Migration d'amibe de dictyostelium : rôle de l'adhésion et de la détection de Quorum

Laurent Golé

Migration of *Dictyostelium* Amoeba:
Role of Adhesion and Quorum Sensing

Laurent Golé

LPMCN

Université de Lyon

Presentée pour l'obtention du titre de Docteur de l'Université Claude Bernard Lyon 1

Soutenu publiquement le 9 décembre 2011

Rapporteurs :

Francois Amblard
Claire Wilhelm

Examinateur :

Franz Bruckert
Pierre Cosson

Directeurs de thèse :

Jean-Paul Rieu
Charlotte Riviere

Abstract

This thesis focuses on the analysis of the role of adhesion between substrate and cell and factors of Quorum sensing on the migration of Dictyostelium amoeba. Tools to automate the recordings of video microscopy and image analysis have been developed to work with very large samples of cells and to quantify cell migration. A microfluidic device for cell detachment in hydrodynamic flow combined with a motorized stage has allowed a statistical study of adhesion but also the dynamics of detachment. The analysis of the migration of Dictyostelium in non nutritive medium highlights the role of density on cell differentiation and migration capacity. We observe the presence of a maximum speed of migration after 6 hours of starvation. We show that the adhesion to glass is twice as low in deprivation buffer as in the nutrient medium. The experiences of migration in growth medium revealed the presence of a factor of detection of density secreted by the cells and regulating their random migration. The diffusion coefficient, the persistence of the movement and morphology of cells vary depending on the concentration of this factor. This factor does not affect cell adhesion but only the dynamics of detachment. Finally, the testing protocol developed allowed us to make a comparative study of migration by varying other parameters such as surface or the chemical composition of experimental medium. This work concludes by outlining the possible role of adhesion to the migration of Dictyostelium in nutrient medium.

Résumé

Cette thèse est centrée sur l'analyse du rôle de l'adhésion cellule-substrat et des facteurs de détection de Quorum sur la migration amibienne de Dictyostelium . Des outils pour automatiser les enregistrements de vidéomicroscopie et l'analyse d'image ont été développés afin de travailler avec de très grands échantillons de cellules et de quantifier la migration cellulaire. Un dispositif microfluidique de détachement cellulaire sous flux hydrodynamique combiné une platine motorisée a permis une étude statistique de l'adhésion mais aussi de la dynamique de détachement. L'analyse de la migration de Dictyostelium en milieu non nutritif met en évidence le rôle de la densité sur la différentiation des cellules et leur capacité de migration. Nous observons la présence d'une vitesse maximale de migration après 6h de carence. Nous montrons que l'adhésion sur verre est deux fois plus faible en milieu carencé qu'en milieu nutritif. Les expériences de migration en milieu nutritif ont révélé la présence d'un facteur de détection de densité sécrété par les cellules et régulant leur migration aléatoire. Le coefficient de diffusion, la persistance du mouvement et la morphologie des cellules varient en fonction de la concentration de ce facteur. Ce facteur ne modifie pas l'adhésion cellulaire mais uniquement la dynamique de détachement. Enfin, le protocole d'analyse développé nous a permis de faire une étude comparative de la migration en faisant varier d'autres paramètres tel que la surface ou la composition chimique du milieu expérimental. Ce travail se conclue en exposant le possible rôle de l'adhésion sur la migration chez Dictyostelium en milieu nutritif.

Contents

Preface

Cell adhesion and migration processes have focused more and more studies during the last decades. Even if the knowledge of such systems has increased considerably, many questions remain open. In particular, the precise role of cell-substrate adhesion on migration is still under debate in the case of amoeba cells. The initial goal of this work was to bring some answers on the interplay between migration and adhesion by a quantitative analysis of cell motility. At the beginning of my thesis, it was very difficult to get reproducible results. A large part of my work has then been dedicated to develop rigorous methodologies to quantify cell migration and adhesion. Careful and precise cell culture is the necessary first step of good research in cellular biophysics. This is particularly important for *Dictyostelium* , as modifications of cell phenotype occur rapidly if cell density in cell culture is too high. Also, understanding that cell density was one of the major parameter regulating migration was a major improvement in reproducibility of our results. Developing automated statistical analysis was necessary to perform multiple experiments and gather large amount of data within the same experimental day. We used microfluidic device to quantify adhesion. A good control of the exact shear flow and a sufficiently large stress range was not easy to obtain. Different microfluidic designs were tested in the course of my thesis. Only the final version is developed in this manuscript. Due to lack of time, I could not take the full advantages of this device to test all desired experimental parameters. In particular, a systematic study of adhesion during development was not performed.

At first, we aimed at measuring both adhesion and migration within the same experimental set-up. However, quantifying cell migration in microfluidic channels is not straightforward as cell migration can be greatly affected (*i*) by the small dimensions found in microfluidic devices leading to a fast concentration increase of molecules secreted by cells if the medium is not renewed, or (*ii*) by the mechanical stimulation induced if a high enough shear flow is applied, leading to bias in cell migration trajectories. Therefore, we have decided to analyze

cell migration and adhesion separately (migration is measured in a separate open dish). Results obtained are developed in Chapter 3, 4 and 5.

Chapter 1 is a description of the biological architecture of cells. It summarizes the main proteins involved in the motility process of eukaryotic cells and explains the coordinated steps required for cells to move. Moreover, state-of-the-art of *Dictyostelium* cells migration and adhesion is given.

In chapter 2, we start by the description of the tools developed to quantify cell motility. The study of *Dictyostelium* cells motion requires large amount of data and precise statistical analysis. We define a diffusion coefficient that characterized cell motion. We then, study the relationship between this parameter and cell shape as well as cell persistence. *Dictyostelium* cells motion in nutrient medium and in the course of development is presented in chapter 3 and chapter 4, respectively. We present how the cell density is a key component tuning cell motion as well as cell morphology in both nutritive and starved condition, with antagonist effects though.

In parallel, we have developed a microfluidic device to quantify cell detachment and to have insight into cell adhesion. Thanks to the parallelization provided by the microfluidic set-up developed, it is also possible to get statistically relevant results within a single experiment. Recording time lapse video of cells submitted to shear flow, we are able to quantify cell adhesion as well as the detachment kinetics by counting cells remaining in the channel at each successive frame. Results are presented in chapter 5. Finally, by comparing cell motion in various environmental conditions (either studying cell motion on different substrates or studying cell adhesion mutants), preliminary conclusions of our understanding of cell migration and adhesion interplay for amoeboid cells are discussed in chapter 6.

Chapter 1

Introduction

Cell motility ability requires the coordination of complex mechanisms. After describing of how migration and adhesion are connected, we will introduce the basic biological features needed for cell motility. Particularities will be given for different type of eukaryotic cells. Then, we will present in detail, *Dictyostelium* cells, the model system we choose in this thesis. We will especially discuss the cell machinery, cell adhesion and quorum sensing in *Dictyostelium* .

1.1 Cell motility

Whereas mobility is defined by the motion of an object, motility refers to the ability of cells to move actively. Therefore, the coordination of complex molecular mechanisms and energy consumption are involved in the process.

Setting apart cell species having specific organelle for motion (cilia or flagellum of sperm cells or certain bacteria), it exists a lot of species that require adhesion on solid substrate to move. Fibroblasts, leukocytes, keratocytes and amoebae belong to the crawling cells group. Crawling of eukaryotic[1] cells on flat surfaces is underlained by the protrusion of the actin network, the contractile activity of myosin II motors, and adhesion to the substrate regulated by complex biochemical networks.

1.1.1 Migration and adhesion interplay
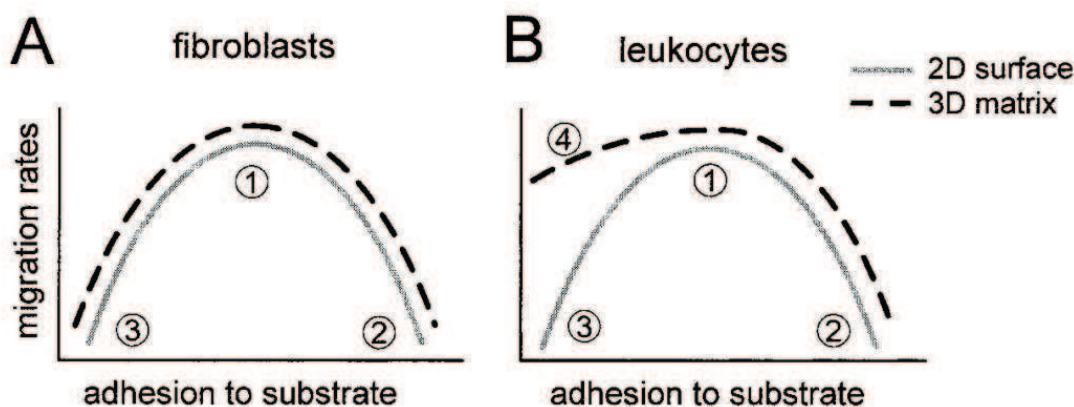
Figure 1.1: Migration Vs. Adhesion. Migration of fibroblasts (**A**) and leukocytes (**B**) on 2-D and within 3-D environments as a function of adhesive strength to the substrate. (**A**) Haptokinetic migration model as established from fibroblasts. In migrating fibroblasts, migration efficiency in both 2-D and 3-D environments is similarly dependent on adhesive interaction to the substrate. Three prototypic migratory states are indicated by numbers. (**B**) Four different migratory states observed for leukocyte migration on 2-D and within 3-D substrates. As a major difference, leukocyte crawling might persist in 3-D environments after adhesion blocking, whereas fibroblast-like migration is dependent on adhesion in both 2-D and 3-D migration models. From (1)

In the haptokinetic model (*i.e.*, adhesion-dependent) of the migration of fibroblasts across

---

[1] Eukaryotic cells are characterized by the presence of one or several nuclei, contrary to prokaryotic cells, which have no nucleus.

ligand-coated surfaces, migration efficiency follows an inverse-U function relative to the adhesive force between the cell and the underlying substrate (Fig. 1.1). Maximum migration rates are achieved at intermediate strength of adhesion to the substrate, allowing the formation of new interactions at the leading edge, while preexisting bonds are sufficiently released at the trailing edge (1, 2). Increasing adhesion, leads to speed reduction, as the rear detachment is impeded. On the other hand, reducing substrate adhesion to a minimum, causes a loss of contact to the substrate. As net interaction and traction forces are further lowered, partial detachment and rounding up of the cells are accompanied by nonproductive oscillatory membrane dynamics and impaired migration. In mammalian cells, adhesion and de-adhesion events are represented by the assembly and disassembly of transmembranous junctions containing adhesion receptors, extracellular ligands, and cytoskeletal elements, called focal adhesions (1). These junctions control cytoskeletal assembly and turnover, adhesion and migration, and related signaling.

1.1.2   How do cells move

The cell migration process can be decomposed in three successive steps (Fig. 1.2). In a first step, from an initial state at which it adheres to the substrate the cell spreads in one direction by forming a protrusion. In a second step, this spreading region is fixed on the substrate via the creation of new adhesion structures. In a third step, the cell retracts from the rear, thus migrating towards the spreading region. The protrusion generated at the cell front region requires two processes: the membrane deformation, and the reorganization of the cytoskeleton. This latter is produced by actin filaments polymerization, which pushes the membrane forward. Myosin-II are recruited at the rear of cells and cross linked with actin filaments, thus contracting the rear of cells. Contractions combined with the rear detachment allow the cell to move forward.

1.2   Mammalian motility machinery

Cell migration are integrated processes requiring in most cell types the coordinated assembly and disassembly of integrin-mediated adhesions (through focal adhesion-related structure) and their coupling to the actin cytoskeleton dynamics (3, 4). In this section, the organization of the cell cytoskeleton, the focal-adhesion-related structure and in particular the structure of integrin proteins and their role in migration and adhesion will be described. Finally, due to its importance for cell migration, we will describe the myosin II motor protein.
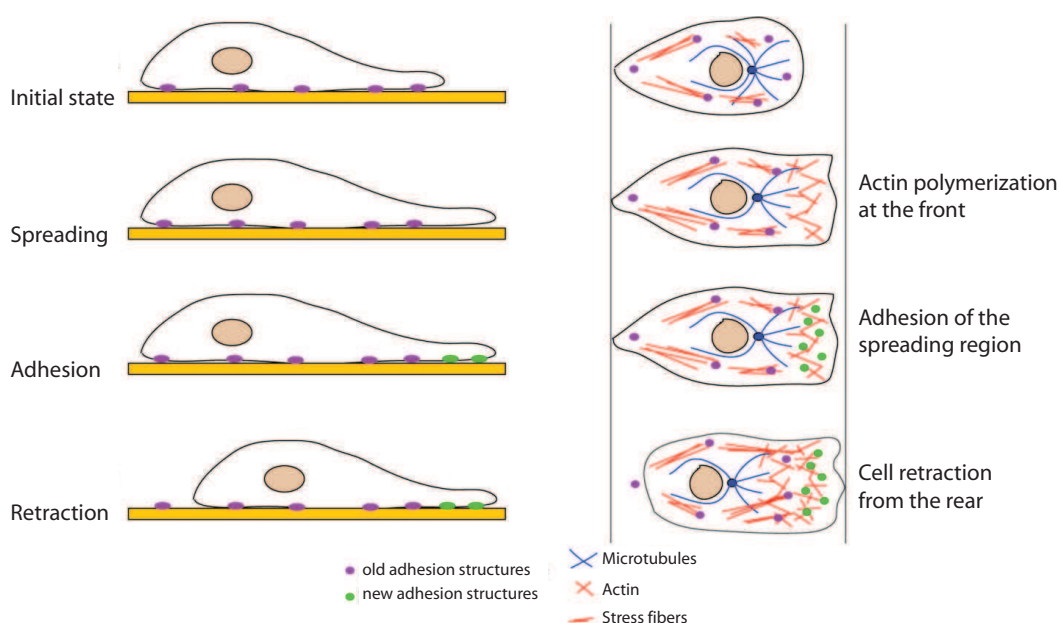
Figure 1.2: Scheme of cell motion. A single cell moving across a two-dimensional substrate is shown in cartoon form (time increases down the page). Detailed morphology varies between cell types, but the same basic types of motility can be distinguished. In cells where the processes occur simultaneously, the morphology is constant during locomotion.

1.2.1 The cytoskeleton

The cytoskeleton, a system of microscopic filaments or fibers, present in the cytoplasm of eukaryotic cells, can be defined as the cell scaffold, which enables to maintain the cell shape and organizes other cell components (Fig. 1.2). It plays an essential role in various biological processes, such as intracellular transport, cellular division, and cell motility. Cytoskeletal elements interact extensively and intimately with cellular membranes (5). Three major types of filaments make up the cytoskeleton: actin filaments, microtubules, and intermediate filaments.

1.2.1.1 Actin

Actin filaments, the thinnest filaments of the cytoskeleton, are the major components of the cytoskeleton (6), and account for the cell mechanical stability and motility (7). Actin filaments occur as constantly changing bundles of parallel fibers. They help cells to maintain their shape, to adhere to surfaces, to move, and assist in cell division during mitosis.

Actin filaments are composed of linear polymers of actin[1] subunits, and generate forces by elongation at one end of the filament coupled with shrinkage at the other, causing net movement of the intervening strand. They also act as tracks for the movement of myosin molecules that attach to the microfilament and walk along them. Actin filaments assume a variety of configurations depending on the type of cell and the state it is in. They extend a considerable distance through the cytoplasm in the form of bundles, also known as stress fibers since they are important in determining the elongated shape of the cell and in enabling the cell to adhere to the substrate and spread out on it. Actin filaments can exist in forms other than straight bundles. In rounded cells that do not adhere strongly to the substrate (such as dividing cells and cancer cells), the filaments form an amorphous meshwork that is quite distinct from the highly organized bundles. The two filamentous states, actin filament bundles and actin filament meshworks, are interconvertible polymeric states of the same molecule. Bundles give the cell its tensile strength, adhesive capability, and structural support, while meshworks provide elastic support and force for cell locomotion.
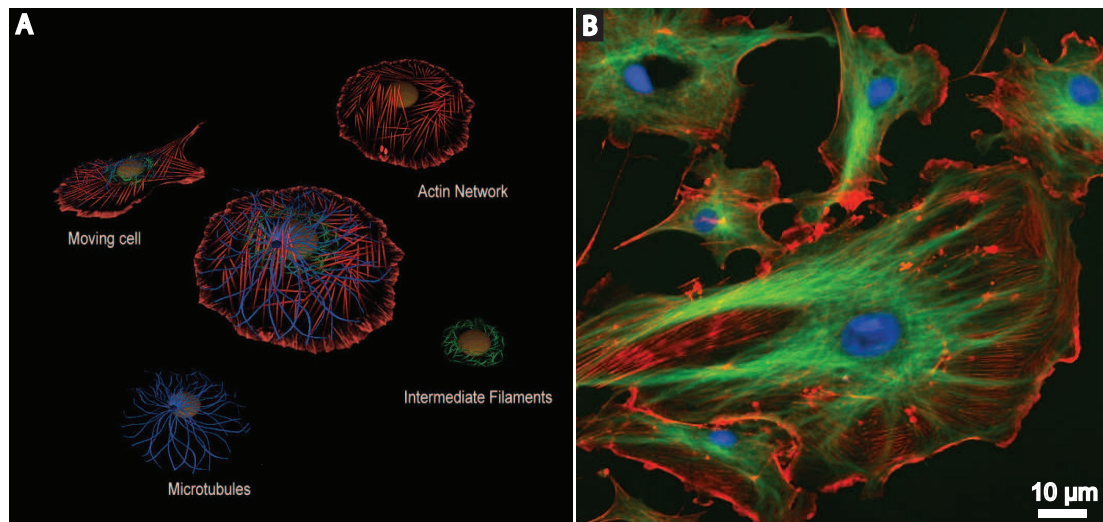
Figure 1.3: The eukaryotic cytoskeleton. (**A**) Schematic representation of the cytoskeleton of a cell in tissue culture. The three main polymer systems are shown: the actin filament arrays (red); the microtubules (blue) and the intermediate filaments (green). (**B**) Endothelial cells under the microscope. Nuclei are stained blue with DAPI, microtubules are marked green by an antibody bound to FITC and actin filaments are labeled red with phalloidin bound to TRITC. Bovine pulmonary artery endothelial cells (Free Pictures from ImageJ).

---

[1]The actin protein is the main structural component of actin filaments in all eukaryotic cells.

1. INTRODUCTION

It is now well known that actin polymerization often entails a retrograde flux of actin along the substratum, leading to a relative speed of the interior of the cell with respect to the substrate. Several studies on distinct systems have shown that the retrograde flow speed is anti-correlated with cell speed (8). Moreover, it was proposed a while ago (9) that force transmission of actin polymerization to the substratum is due to a molecular clutch of proteins. The more the clutch is engaged the smaller the retrograde flow and the higher the speed and the force on the substratum. Alternately, the frictional coupling with the substrate could be essentially non-specific.

1.2.1.2 Microtubules

Microtubules are cylindrical structures that exhibit a cytoplasmic distribution distinct from actin filaments. Microtubules originate in structures that are closely associated with the outside surface of the nucleus known as centrioles. The major structural protein of these filaments is known as tubulin. Unlike the other two classes of filaments, microtubules are highly unstable structures and appear to be in a constant state of polymerization-depolymerization. They play key roles in intracellular transport (they help to transport organelles like mitochondria or vesicles) as well as in the mitotic spindle (10).

1.2.1.3 Intermediate filaments

Intermediate filaments provide structural support for the cell. They anchor the nucleus within the cell and give the cell its elastic properties. These filaments, around 10 nanometers in diameter, are more stable (strongly bound) than actin filaments, and heterogeneous constituents of the cytoskeleton (10). Like actin filaments, they function in the maintenance of cell-shape by bearing tension. Intermediate filaments organize the internal tridimensional structure of the cell, anchoring organelles and serving as structural components of the nuclear envelop. They also participate in some cell-cell and cell-matrix junctions.

1.2.2 Focal Adhesion-Related Structures

Cell adhesion is essential for many important cellular processes, such as tissue organization and differentiation, embryonic development and, as we have seen in the previous section, cell migration. Distinct types of adhesions structures between cells and the extracellular matrix (ECM) have been identified (12, 13).
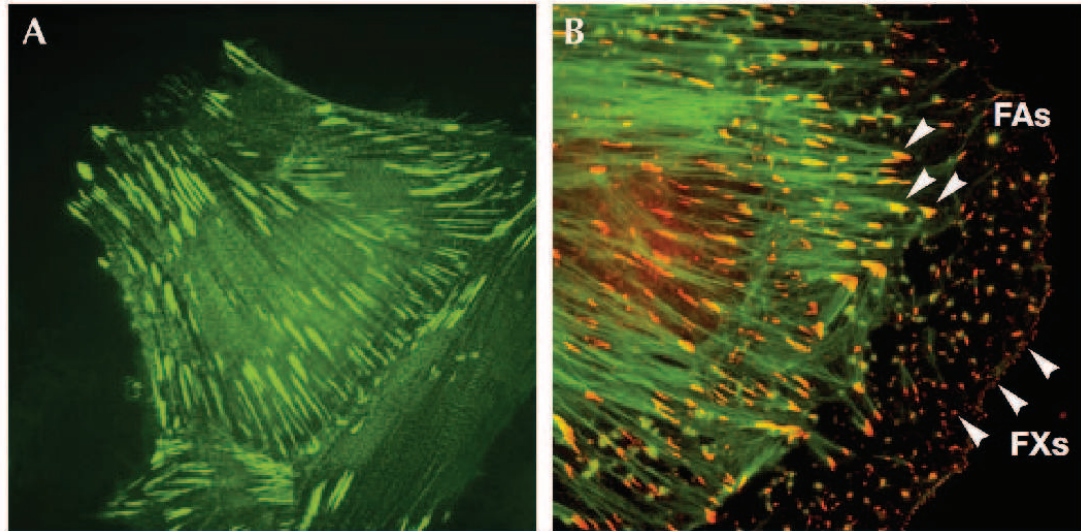
Figure 1.4: Different types of cell extracellular matrix contact structures. (**A**) Elongated focal adhesions (FAs) in a stationary adhesive cell. (**B**) Peripheral focal complexes (FXs) and anchoring FAs in a protruding cell. From (11)

Focal adhesion-related structures include two main types of structures: focal complexes and focal adhesions (Fig. 1.4). Initially, during cell migration, focal complexes (0.5 to 1 μm dot-like contacts) are formed along the lamellipod. These complexes are not directly linked to stress fibers. They can mature into large and stable focal adhesions (3 to 10 μm). Focal adhesions are protein complexes, mainly composed of actin filaments, integrins[1], and some other proteins like vinculin, paxillin and talin (4, 14). It connects the actin cytoskeleton to the extracellular matrix through integrins. Focal adhesions are linked to stress fibers. They are used as anchor by the cell, which can push or pull itself over the extracellular matrix. During the cell migration, a given focal adhesion gets closer and closer to the cell trailing edge. Once at the trailing edge, it will be dissolved in order for the cell to continue its motion (see Fig. 1.2).

1.2.3 Integrins

Integrins are the principal receptors used by animal cells to bind to the extracellular matrix. They are heterodimers and function as transmembrane linkers between the extracellular matrix and the actin cytoskeleton (15). Integrins also function as signal transducers, activating various intracellular signaling pathways when activated by matrix binding. Integrins and conventional

---

[1]integrins are transmembrane proteins. It will be described in more detail in the following section 1.2.3

signaling receptors often cooperate to promote cell growth, cell survival, and cell proliferation.

Integrins are crucially important because they are the main receptor proteins that cells use to both bind to and respond to the extracellular matrix (16). An integrin molecule is composed of two noncovalently associated transmembrane glycoprotein subunits called α and β (Fig. 1.5). At least 18 α and 8 β subunits are known in humans, generating 24 different heterodimers. Moreover, because the same integrin molecule in different cell types can have different ligand-binding specificities, it is likely that additional cell-type-specific factors can interact with integrins to modulate their binding activity.
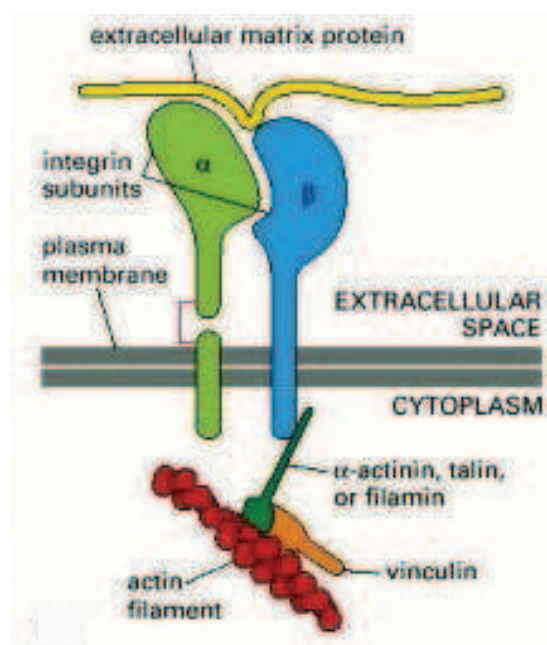
Figure 1.5: Some of the proteins that form focal adhesions. The transmembrane adhesion protein is an integrin heterodimer, composed of an α and a β subunit. Its extracellular domains bind to components of the extracellular matrix, while the cytoplasmic tail of the β subunit binds indirectly to actin filaments via several intracellular anchor proteins. (10)

Integrins function as transmembrane linkers, mediating the interactions between the cytoskeleton and the extracellular matrix that are required for cells to grip the matrix. Most integrins are connected to bundles of actin filaments. After the binding of a typical integrin to its ligand in the matrix, the cytoplasmic tail of the β subunit binds to several intracellular anchor proteins, including talin, α-actinin, and filamin (Fig. 1.5). These anchor proteins can bind directly to actin or to other anchor proteins such as vinculin, thereby linking the integrin to

actin filaments in the cell cortex. Given the right conditions, this linkage leads to a clustering of the integrins and the formation of focal adhesions between the cell and the extracellular matrix.

It seems that integrins must interact with the cytoskeleton to bind cells strongly to the matrix. The cytoskeletal attachment may help cluster the integrins, providing a stronger aggregate bond. Integrins can mediate cell-matrix adhesion without forming mature focal adhesions. In both cases, however, the transmembrane adhesion proteins may still bind to the cytoskeleton. For integrins, this kind of adhesion occurs when cells are spreading or migrating, and it results in the formation of focal complexes. For such focal complexes to mature into the focal adhesions that are typical of many well-spread cells, the activation of the small GTPase Rho[1] is required (17). The activation of Rho leads to the recruitment of more actin filaments and integrins to the contact site.

1.2.4 Myosin II

Motor proteins use the energy of ATP hydrolysis to move along microtubules or actin filaments. They mediate the sliding of filaments relative to one another and the transport of membrane-enclosed organelles along filament tracks. All known motor proteins that move on actin filaments are members of the myosin superfamily (10). Motor proteins bind to a polarized cytoskeletal filament and use the energy derived from repeated cycles of ATP hydrolysis to move steadily along it. Dozens of different motor proteins coexist in every eucaryotic cell. They differ in the type of filament they bind to (either actin or microtubules), the direction in which they move along the filament, and the cargo they carry. Many motor proteins carry membrane enclosed organelles such as mitochondria, Golgi stacks, or secretory vesicles to their appropriate locations in the cell. Other motor proteins cause cytoskeletal filaments to slide against each other, generating the force that drives such phenomena as muscle contraction, ciliary beating, and cell division.

The cytoskeletal motor proteins associate with their filament tracks through a head region, or motor domain, that binds and hydrolyzes ATP. Coordinated with their cycle of nucleotide hydrolysis and conformational change, the proteins cycle between states in which they are bound strongly to their filament tracks and states in which they are unbound. Through a

---

[1]The Rho family of GTPases is a family of small ($\sim 21kDa$) signaling G protein. The members of the Rho GTPase family have been shown to regulate many aspects of intracellular actin dynamics, and are found in all eukaryotic organisms

mechanochemical cycle of filament binding, conformational change, filament release, conformational relaxation, and filament rebinding, the motor protein and its associated cargo move one step at a time along the filament (typically a distance of a few nanometers). The identity of the track and the direction of movement along it are determined by the motor domain (head), while the identity of the cargo (and therefore the biological function of the individual motor protein) is determined by the tail of the motor protein.

Myosin II[1] is responsible for generating the force for muscle contraction. This protein forms bipolar filaments that cross-link actin filaments and stiffen cell protrusions. It is an elongated protein that is composed of two heavy chains and two copies of each of two light chains. Each of the heavy chains has a globular head domain at its N-terminus that contains the force-generating machinery, followed by a very long amino acid sequence that forms an extended coiled-coil that mediates heavy chain dimerization (Fig. 1.6). The two light chains bind close to the N-terminal head domain, while the long coiled-coil tail bundles itself with the tails of other myosin molecules. These tail-tail interactions result in the formation of large bipolar thick filaments that have several hundred myosin heads, oriented in opposite directions at the two ends of the thick filament.
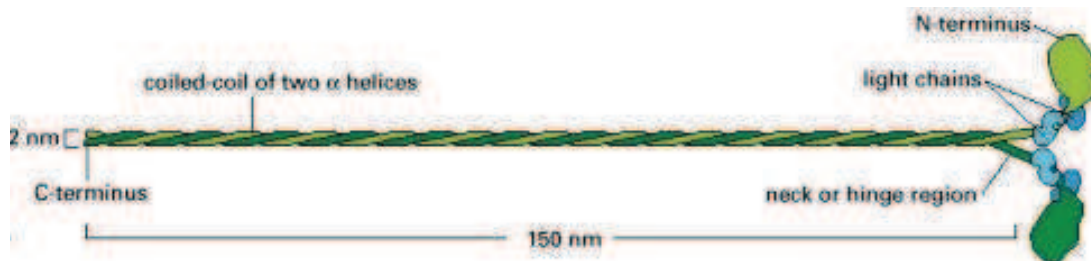
Figure 1.6: myosin-II. A myosin II molecule is composed of two heavy chains (each about 2000 amino acids long (green) and four light chains (blue)). The light chains are of two distinct types, and one copy of each type is present on each myosin head. Dimerization occurs when the two α helices of the heavy chains wrap around each other to form a coiled-coil, driven by the association of regularly spaced hydrophobic amino acids. The coiled-coil arrangement makes an extended rod in solution, and this part of the molecule is called the tail. From (10)

Only actin polymerization is required for cell spreading whereas myosin-II activation, allowing contraction and retraction of cells rear through the actin-myosin complex, is necessary for efficient cell migration. Myosin II was further shown to mediate posterior contraction enabling the rear of the cell to detach from the substrate and move in concert with the leading

---

[1] also called conventional myosin

edge. Although myosin II-deficient cells are principally able to generate pseudopods and undergo locomotion on surfaces, the migration velocity as well as mechanical force generated at the leading edge of myosin II-deficient cells is reduced as a consequence of reduced cortical stiffness, delayed posterior release of adhesive bonds, and rear retraction (18).

1.3   Different type of 2D-cell migration

Three main classes of migration mechanism have been extensively analyzed: *(i)* slow moving cells such as fibroblasts; *(ii)* highly motile cells with quasi-steady cell shape and movement mainly perpendicular to cell major axis such as keratocytes; *(iii)* highly motile and deformable cells with movement mainly parallel to cell major axis, such as amoeba cells, crawling neutrophils, lymphocytes or metastatic cells. The table 1.1 summarizes the order of magnitude of migration and adhesion for 3 different type of cells.

	V(μm/min)	Adhesion (Pa)	Traction forces (nN)	References
Fibroblasts	1	10	900	(19, 20, 21)
Keratocytes	30	1	10	(22, 23, 24)
Amoeba	[3-12]	1	[30-70]	(25, 26)
Dictyostelium	[4-10]	1	[3-5]	(27, 28)

Table 1.1: Order of magnitude of migration (typical cell speed), adhesion (typical shear stress necessary for cell to substrate detachment) and force exerted by cells on soft substrate for various type of cells.

1.3.1   Fibroblasts-like cell motility

When polarized, fibroblasts are slow moving cells. Their speed is around 1 μm/min on a collagen substrate. As all eukaryotic cells, they have microtubules, intermediate filaments and actin filaments. This type of cell forms strong focal adhesions, where actin filaments converge to form tensile fibers. These actin filaments are necessary to exert forces required for motility on a surface (30). In fibroblasts, microtubules are involved in cell polarization (31). Indeed, the depolymerisation of their microtubules leads to the depolarization of cell shape and an increase in the contractility of the cytoskeleton and actin organization (32).

11
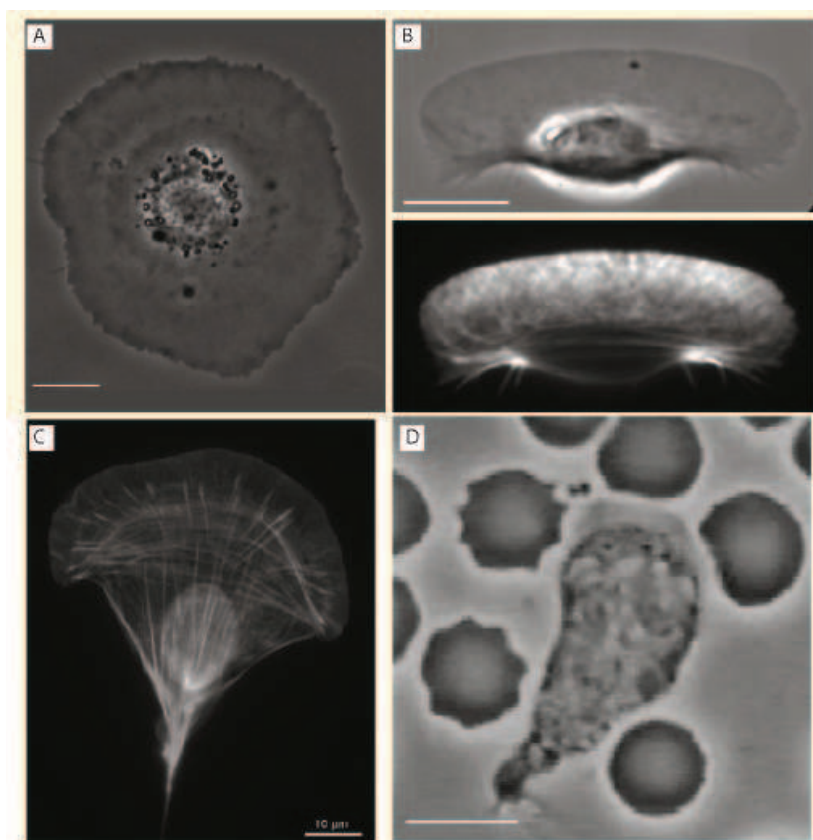
Figure 1.7: Diverse shapes of motile cells. (**A**) Phase contrast image of a live stationary kerato-cyte. The cell body is at the center, surrounded by a flat lamellipodium. (**B**) Phase contrast (top) and fluorescence (bottom) images of a motile keratocyte fixed and stained with phalloidin to visu-alize actin filaments. The broad lamellipodium at the front has a characteristic criss-cross pattern of actin staining, while bundles of actin appear near the cell body at the rear. (**C**) Fluorescence image of a cultured mouse embryo fibroblast fixed and stained with phalloidin. Fluorescence signal from the lamellipodial actin meshwork and from linear actin structures, including arcs at the base of the lamellipodium, linear stress fibers and peripheral bundles is visible, together with autofluorescence from the cell nucleus. (**D**) A human neutrophil surrounded by red blood cells chasing a bacterium. Bars, 10 μm. From (29)

1.3.2   Keratocyte-like cell motility

Keratocytes are the predominant cell type in the epidermis. These cells use a single large lamel-lipodium along their front side arc to rapidly crawl in relatively straight lines while maintaining their characteristic half-moon shape with the cell body containing nucleus at the rear. Their mi-gration speed is up to 30 μm/min. Lee at al.(33) have shown that while intermediate filament

and microtubules are located around the nucleus only, the large lamellipodium is rich of actin filament. Branched actin filaments are distributed within lamellipodium of these cells (34) along with Arp2/3[1] complexes situated at the branched points of the actin filaments, enabling the Arp2/3-dependent actin polymerization to drive the advance of the lamellipodium. Filaments of myosin II align along the concave rear cortex, and mechanical analysis demonstrated that the largest traction forces are detected perpendicular to the left and right cell margins (35). Notably, lamellar fragments of keratocytes, which are devoid of nucleus and of a microtubule cytoskeleton, can still move unidirectionally, indicating that these structures are dispensable for the movement (36). Application of a small external force converts a lamellar fragment in the stationary state to the locomotive state (37). Still, it is unclear how the pseudopodium-forming site is determined and how polarization is maintained.

1.3.3 Amoeboid-like cell motility

Mammalian cells moving using amoeboid-type motility are fast cells including mainly neutrophils and metastatic cells. The unicellular organism *Dictyostelium* that was used as cell model during this thesis shares many features in common with such cells. *Dictyostelium* specificity will be described in more details in the next section. We will focus in this section on mammalian amoeboid motility. Amoeboid migrating cells share one morphological feature that defines them as amoeboid: during locomotion they constantly change shape by rapidly protruding and retracting extensions that have been originally described as pseudopods or false feet (38). In amoeboid cells, the movement is hypothesized to be driven by weak-interaction with the substrate, and cell generated forces have been assumed to involve mainly adhesion-independent forces (1). Movement is generated by cortical filamentous actin, whereas mature FA and stress fibers are lacking (1, 39). However, physical contact with the environment (friction) is still necessary for the cell to translate internal traction forces generated by polymerization or contraction into directed forward motion. It has recently been suggested that, in confined 3D geometries, the intracellular actin network expanding by polymerization can not only propel the cell forward but also generate enough friction laterally by pushing the cell membrane against the walls of the confinement, making specific surface anchoring dispensable (38, 40). Few studies have also described the migration via leading edge bleb formation (41, 42). As a newly formed and protruding bleb is free of actin filaments that generate retrograde forces, it is

---

[1]Arp2/3 is a protein found in most eukaryotic organisms and plays a key role in actin polymerization

entirely unclear whether and how blebs might transduce traction forces onto the substrate: once the bleb adhered to the substrate, the anterograde forces of the expanding bleb would rather push the cell body backward than pull it forward. It has been shown that amoeboid cells can mechanically adapt to the adhesive properties of their substrate by switching between integrin-mediated and integrin-independent migration (43). As far ar neutrophils are concerned, they have been shown to display amoeboid-type of migration when moving towards the source of bacterial infection. Neutrophils have receptors to detect small amount of peptides N-formyles derived from bacterial proteins. As little as 1% of variation in concentration of peptides can be detected by neutrophils and guides them toward bacteria for phagocytosis (44). Neutrophils are usually round but polarized easily with a chemotactic stimulation, expending lamellipod at the front and an uropod at the back, thus migrating on a substrate at high speed (around 10 μm/min). As eukaryotic cells, their cytoskeleton contains actin filaments, microtubules and an intermediate filament network. Actin filaments are largely recruited in the forwarding front and are necessary for cell migration. When cells are polarized, actin filament and myosin-II are required to develop and maintain cell asymmetry of microtubules networks in the cell body.

1.4 *Dictyostelium* Discoideum

1.4.1 *Dictyostelium* Life Cycle

Dictyostelium is a soil-living amoeba first isolated by Raper *et al.* in 1935 (45). *Dictyostelium* is a primitive eukaryote that is able to differentiate from unicellular amoebae into a multicellular organism and then into a fruiting body within its lifetime (Fig. 1.8). In the wild, *Dictyostelium* can be found in soil and moist leaf litter. The primary diet of *Dictyostelium* consists of bacteria, which are found in the soil and decaying organic matter. The amoebae feed on bacteria by phagocytosis.

It is a great convenience to be able to grow *Dictyostelium* in a broth medium rather than on live or dead bacteria. AX2 is an axenic strain which can grow in a simplified medium (HL5 medium) without bacteria (47). Independently another *Dictyostelium* axenic strain, AX3, has been isolated by WF Loomis. AX3 gave rise to a number of derivatives and contains a large duplication that is not present in AX2. Both strains grow well in the defined minimal medium (HL5). In this thesis, DH1[1] strain is used. When nutrients are available, *Dictyostelium* lives,

---

[1]DH1 was made by Dale Hereld in the Devreotes lab. It's an AX3 derivative with the entire coding sequence of pyr56 removed using a PCR-constructed splint and FOA selection.
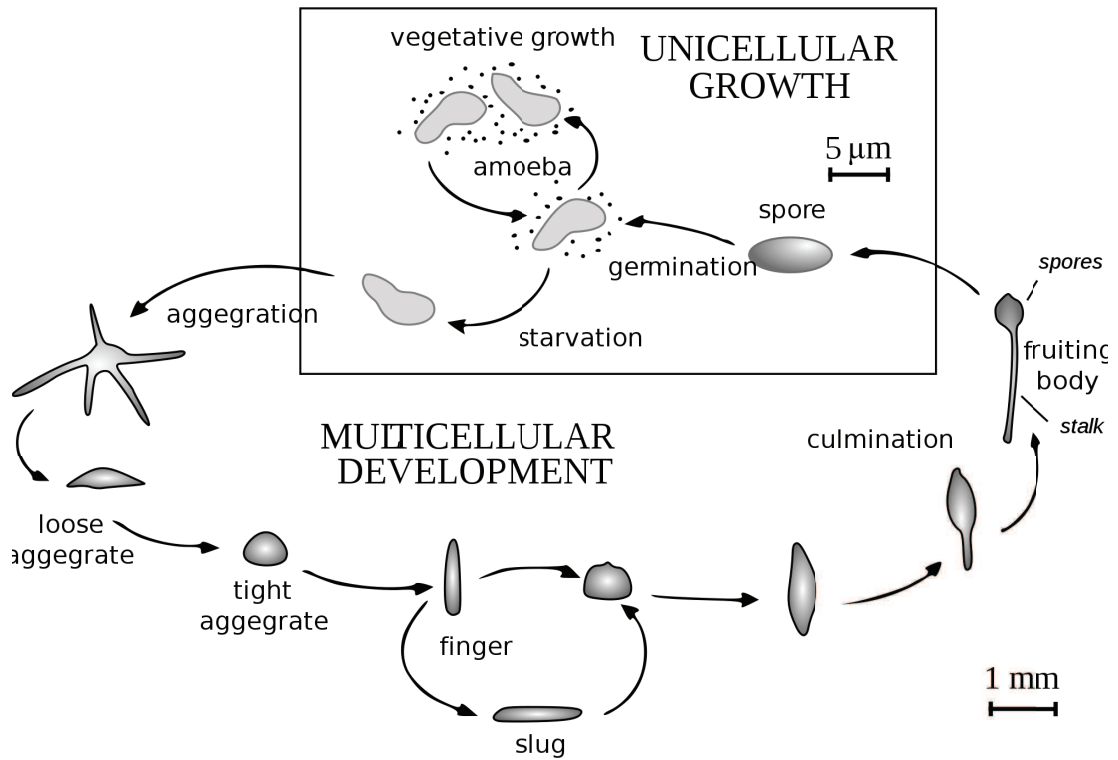
Figure 1.8: ***Dictyostelium* life cycle.** Schematic view of unicellular growth and multicellular development of *Dictyostelium* cells.

Figure 1.9: ***Dictyostelium* development.** Structures formed during development, arranged chronologically from left to right: mound, tipped mound, first finger, slug, mexican hat, mid-culminant and fruiting body. From (46)

divides and grows as single-cell amoeba (with an averaged diameter of 10μm, if it is considered spherical). This growth phase is called vegetative stage.

Exhaustion of the bacterial food source triggers a developmental program (Fig. 1.8 and 1.9), in which up to 100,000 cells aggregate by chemotaxis towards cAMP (Fig. 1.10). Morphogen-
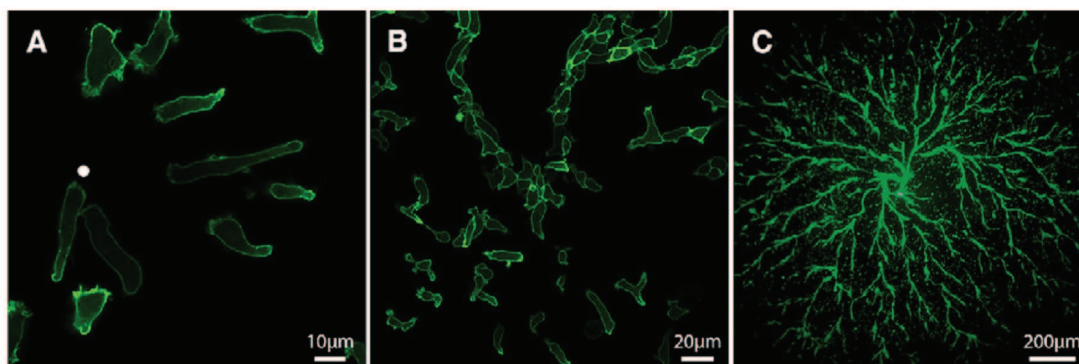
Figure 1.10: *Dictyostelium* **chemotaxis.** All cells are labeled with a marker for the F-actin cytoskeleton, tagged with GFP. (**A**) Migration of amoebae towards a micropipette filled with cAMP (position indicated by white dot). (**B**) Formation of an early aggregation centre. (**C**) Cells streaming during aggregation. From (46)

esis and cell differentiation then culminate in the production of spores enabling the organism to survive unfavorable conditions (Fig. 1.8). *Dictyostelium* offers unique advantages for studying fundamental cellular processes with the aid of powerful molecular genetic, biochemical, and cell biological tools. These processes include signal transduction, chemotaxis, cell motility, cytokinesis, phagocytosis, and aspects of development such as cell sorting, pattern formation and cell type differentiation. *Dictyostelium* was also described as a suitable host for pathogenic bacteria in which one can conveniently study the process of infection (48). The recent completion of the *Dictyostelium* genome sequencing project strengthens the position of *Dictyostelium* as a model organism. The completed genome sequence and other valuable community resources constitute the source for basic biological and biomedical research and for genome-wide analyses (49). Together with a powerful armory of molecular genetic techniques that have been continuously expanded over the years, it further enhances the experimental attractiveness of *Dictyostelium* and positions the organism on the same level as other fully sequenced model organisms like S. cerevisiae, Caenorhabditis elegans, or Drosophila melanogaster.

1.4.2 *Dictyostelium* Motility Machinery

Even if *Dictyostelium* is a primitive eukaryote, it shares many similarities with mammalian cells (hence its importance as model system of amoeboid migration). *Dictyostelium* cells are fast-moving cells ($\sim 10\mu$m/min) with an irregular shape changing very dynamically. In many aspects, they follow the classical extension- retraction cycle (Fig. 1.2) with steps 1 and

16

2 (spreading and adhesion) probably occurring simultaneously due to the absence of mature adhesion complexes in *Dictyostelium* and the probable importance of non-specific adhesion. In this section, we will first describe in more details this extension-retraction cycle for the various developmental stages of *Dictyostelium* adhesion. In particular, we will present results on cell speed, shape and traction forces oscillations, on more detailed pseudopod dynamics and we will discuss the role of actin polymerization and myosin II in this basic motility. We will then focus on the main adhesion proteins found in *Dictyostelium* and summarize the scarce knowledge of the adhesion-migration interplay in this cell type.

1.4.2.1 Coordinated shape changes and traction forces during *Dictyostelium* motility

In *Dictyostelium*, it is known that pseudopodia are periodically induced at points on cell periphery, as if they were driven by an internal oscillator (50). Due to the main extension-retraction cycle, cell speed oscillates with a 1-2 min period both in the vegetative (51) and aggregating phase (52).

In the vegetative state, cells present correlated cyclic changes in term of speed, shape (between an elongated form and a more rounded one) and forces (Fig. 1.11). Forces are always oriented centripetally. They are minimal when the cell is rounded. When the cell elongates, the force gradually increases until the rear starts to retract and the force decreases. Forces are especially large when the front and rear are symmetric. However, one observes more often a front-rear asymmetry in shape and force with a higher forces in the uropod balanced with smaller forces distributed over a larger area in the front (Fig. 1.14). For the whole vegetative cells examined in (28), the average durations of one cycle was 95 ± 25 seconds from force or shapes time series. With a rapid extension (E) plus a rapid retraction (R), one can find generally twice more peaks of speed than peaks of force as indexed in Fig. 1.11.

In the aggregating phase, cells are faster, more elongated and more persistent. They also exhibit periodic speed, shape and force changes with a period time T comprised between 1 and 2 min (53). Interestingly, cell speed V is inversely proportional to T and could be approximated by the hyperbola $VT = \lambda$ where λ is of the order of the cell size (20 μm) (53). Barnhart *et al.* observed the same relation for fish epithelial keratocytes and presented a simple mechanistic model providing theoretical grounds for a linear relation between cell speed and frequency in which periodic retraction of the trailing edge is the result of elastic coupling with the leading edge (54).
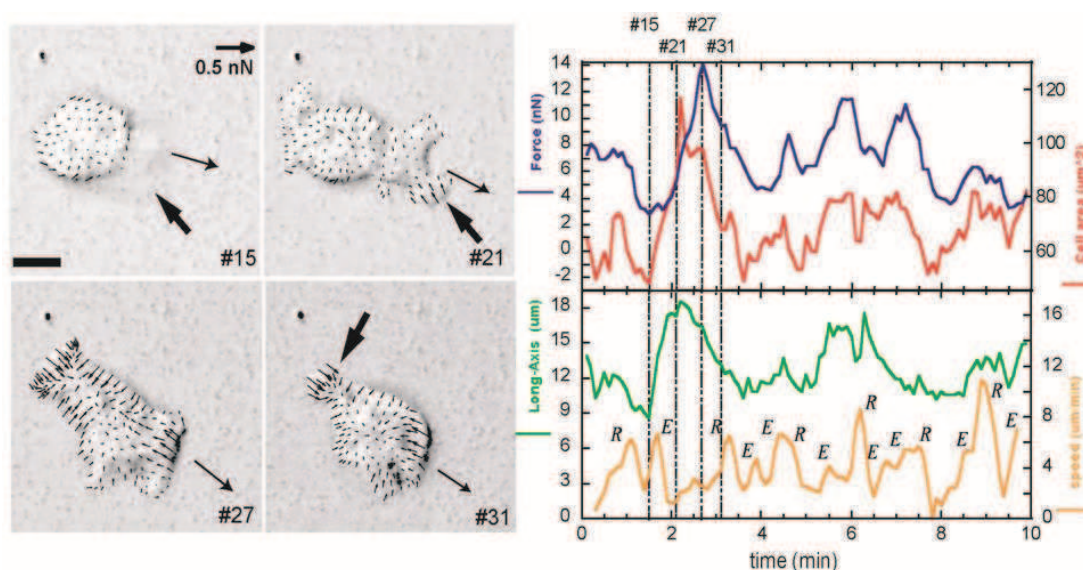
Figure 1.11: Time Series of forces, speed and shape (area and major axis) of an AX2 *Dictyostelium* cell in the vegetative phase. (Left) Force maps on a very soft polyacrylamide elastomer substrate ($E = 400$ Pa). Frame number is indicated on bottom right of each panel. Time interval is 6 sec between two recorded frames; small arrows indicate the direction of cell motion; large arrows refer to cell protrusions. The sequence that lasts for 2.4 min shows a cell initially rounded that extends a large pseudopod towards the bottom right (arrow), exerts large symmetrical forces ($F_0 \simeq 10$ nN) at maximal elongation and afterwards slowly retracts from its initial position (see arrow) and becomes rounded again (not shown). (Right) Plots as a function of time of the overall absolute value of the force (blue), cell area (red), cell major axis (green) and cell speed (orange). Peaks of speed are indexed with the subscript R or E to indicate whether they correspond to retraction or extension events. Bars, 5 μm. From (28).

The extension-retraction cycle of *Dictyostelium* aggregating cells has a 3D cyclic z-axis extension (Fig. 1.13). First, a dynamic pseudopod, which lasts for about 30 seconds is extended, then, the pseudopod either retracts, or attaches to the underlying substrate and pulls the remainder of the cell body towards it (52). Pseudopods can form on and off the substrate. Ones which initially form on the substrate, or those which form off the substrate and subsequently contact it, are more likely to become the new expanding anterior end of a cell, while pseudopods that form off the substrate and do not subsequently contact it are retracted (55). Large retraction or extension peaks are neither observed in the evolution of traction forces nor in the evolution of cell major axis (Fig. 1.12). The front-rear asymmetry in shape and force observed generally for vegetative cells is not so obvious for aggregating cells. The largest forces measured here are not always located at the outermost boundary of the rear, with even transient absence of forces
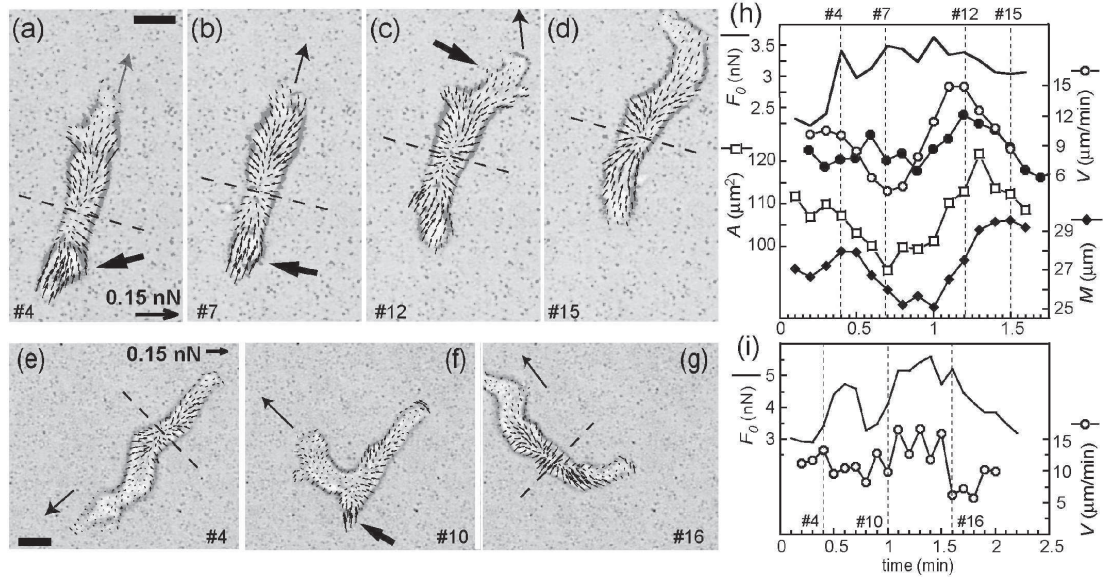
Figure 1.12: Time Series of forces, speed and shape (area and major axis) of two AX2 *Dictyostelium* cells in the aggregating phase. (**a**)-(**g**) Force maps on soft polyacrylamide elastomer substrates ($E = 1150$Pa). Frame # is indicated on bottom right of each panel. Time interval is 6 sec between two recorded frames; small arrows indicate the direction of cell motion; large arrows are discussed in the text. The first cell (**a-d**) is moving straight and slightly turning left at the end of the sequence while in (**d**)-(**f**) the second cell is suddenly turning. (**h**)-(**i**) Plots as a function of time of the overall absolute value of the force (solid line), cell centroid speed (circles), rear edge speed (bullets), cell area (open squares) and cell major axis (black diamonds) for cell 1 (**h**) and cell 2 (**i**). The overall force is about $F_0 = 3$ nN during straight trajectories or slow turns and increase during a sudden turn. Bars, 5 μm. From (28).

at the rear (Fig. 1.12d,e,g). This indicates that the uropod of these cells is more loosely bound to the substrate and even partially floating. Forces are generally not detectable in the newly extended long pseudopods but very large in turning cells (Fig. 1.12f) or retracting pseudopods (Fig. 1.14).

1.4.2.2 Actin-based and myosin II-based propulsive forces in migrating *Dictyostelium* cells

Like other eukaryotic cells, actin filaments and microtubules are part of the cytoskeleton of *Dictyostelium* cells. However, these cells do not posses intermediate filament. Although microtubules are involved in the stability of pseudopod formation and play a role in the directionality of movement (56), *Dictyostelium* cells can move and stay polarized without them (57). Actin

A.

B.
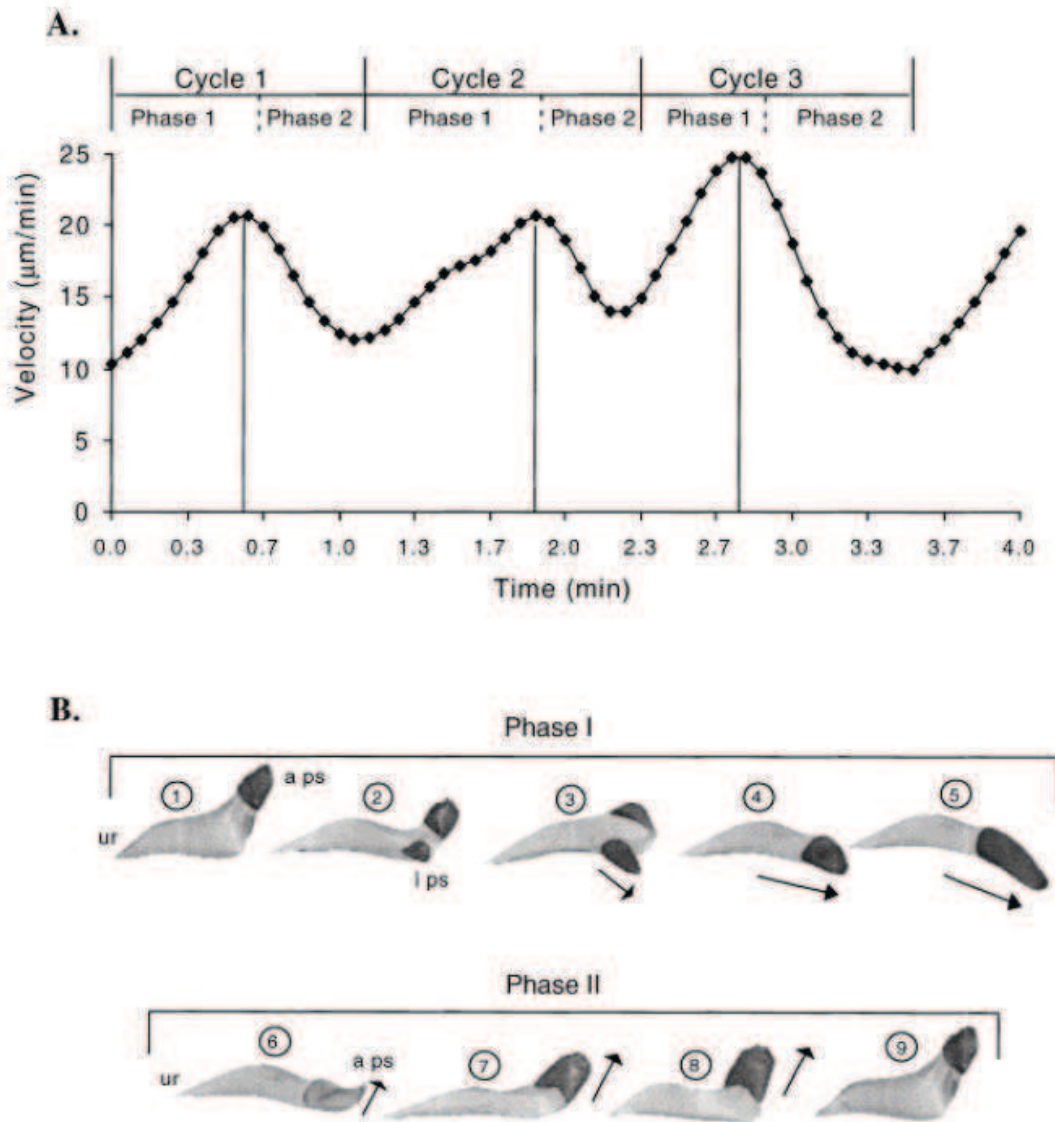
Figure 1.13: Description of the behavior cycle of AX3 *Dictyostelium* aggregating cells crawling in buffer. (**A**) Time plot of instantaneous velocity of a representative amoeba smoothed to delineate velocity peaks and troughs. The behavior cycles and the two phases of each cycle (phases I and II) are demarcated at the top of the plot. Peaks are noted by vertical lines. (**B**) Cartoon of consensus cell behavior in phases I and II of the behavior cycle. The nonparticulate cytoplasmic zones of pseudopods are shaded. Arrow, direction of centroid translocation. Abbreviations: aps, anterior pseudopod; lps, lateral pseudopod; ur, uropod. From (52).

filaments are recruited in the front of the cells emitting protrusions and are necessary for cells motility. Indeed, *Dictyostelium* cells become round and cannot migrate if they are exposed

to drugs such as Latrunculin-A that depolymerize actin networks. It is well known that cell migration is a complex process mediated by dynamic changes in the acto-myosin cytoskeleton. It is now generally thought that actin polymerization at the leading edge provides a critical driving force for extension of most eukaryotic cells including *Dictyostelium* cells (39, 58, 59) whereas the detachment and retraction of the rear of the cell from the substratum is thought to be induced by contraction via myosin II-dependent processes (18, 28, 53, 58, 59). Past immunofluorescence and more recent fluorescence studies have revealed the presence of distinctive organizations of filamentous F-actin: (i) highly branched in three-dimensional meshworks in pseudopodia, (ii) cortical bundles or meshworks with increased thickness towards the rear (cortical actin), and (ii) radial arrays or actin foci emerging from postulated adhesion sites (58, 60, 61, 62). Myosin-II on the other hand is mainly present at the cortex with an increasing concentration at the rear part (uropod) and transiently in retracting pseudopods in randomly moving *Dictyostelium* cells (28, 58). Myosin II is thus traditionally assumed to cause the contraction of the posterior, and to inhibit the formation of lateral pseudopods which could impair directed migration (50). However, it has been shown, that myosin II-knockout mutants, even if slower than wild type, were still able to move (53, 63) indicating that cells use also myosin-II independent propulsive force (*i.e.*, actin polymerization). This general picture of the role of actin and myosin-II is now well documented by traction force microscopy experiments.

Fig. 1.14 presents the co-localization of myosin II and large retracting forces in the rear and retracting pseudopods using a myosin II-GFP expressing *Dictyostelium* strain (28). Lombardi *et al.* found in vegetative cells a period of increasing force in the uropod followed by a sudden drop after abrupt uropod retraction (within 5 seconds) allowing for protrusion in the front to begin rapid recoil retraction mode, (63). On the other hand, myosin II is clearly absent from the traction area of the long starved cell indicated with an arrow in Fig. 1.14g. Here, the propulsive force likely results from the reaction force to actin polymerization in the neighborhood of the leading edge. The exact mechanisms of such a reaction force are not yet fully understood and the exact coupling between actin and the substrate is not clearly identified in *Dictyostelium* (see next section).

1.4.2.3 A relation between migration efficiency and adhesion in *Dictyostelium* ?

As already stated, the initial question of this thesis was to investigate whether the well established adhesion/speed relationship for fibroblastic cells (Fig. 1.1) occurred for highly dynamic amoeboid cells. While fibroblasts adhere and exert forces through focal adhesions, no structure
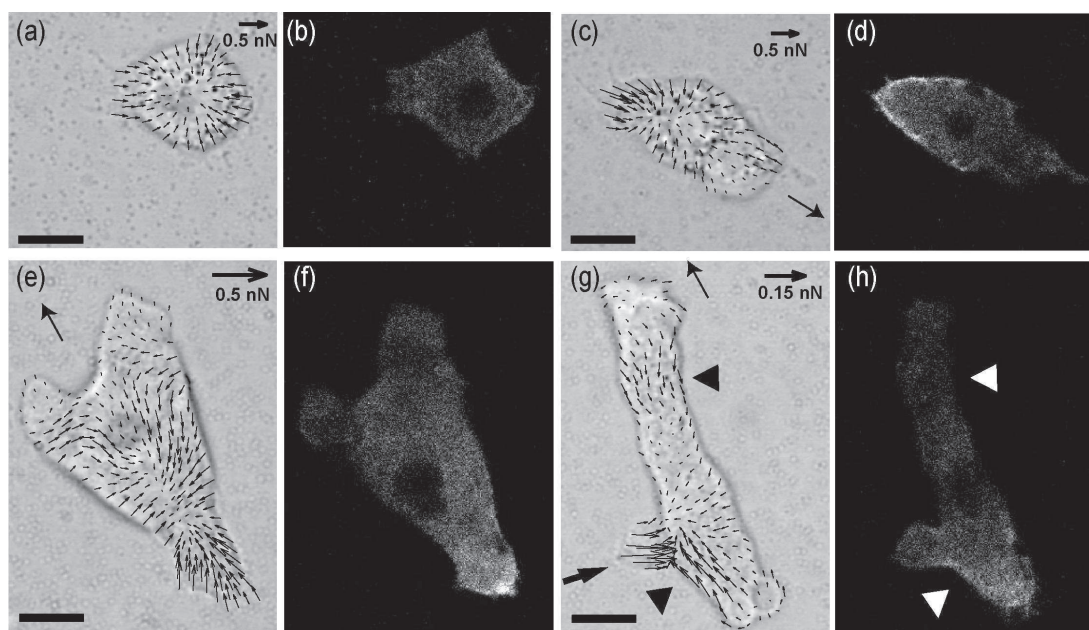
Figure 1.14: Co-localization of myosin II and forces using AX-2 cells expressing GFP- myosin II. (**a**)-(**d**) Vegetative cell presenting both a rounded shape with peripheral force distribution (**a**)-(**b**) and an asymmetric shape and force distribution (**c**)-(**d**). (**e**)-(**f**) Starved cell with an asymmetric force distribution. (**g**)-(**h**) Long starved cell with a retracting pseudopod (large arrows in (**g**)). In each case, note the good co-localization of forward directed retraction forces with myosin II but not of propulsive forces (compare arrowheads in (**e**) and (**f**)). Bars, 5 μm. From (28).

similar has been found in *Dictyostelium* . According to Uchida *et al.*, *Dictyostelium* adhesion to substrate is done through actin foci (61). They are very dynamic structures that appear and disappear at the surface on the substratum during cell migration. Reflection interference microscopy revealed that the ventral cell membrane was closer to the substratum at sites of actin foci (Fig. 1.15A). Bretschneider *et al.* found similar actin structures and showed that they contain the Arp2/3 complex which favors actin branching (60). Such actin foci may also contain the putative membrane proteins of *Dictyostelium* . Interestingly, Uchida *et al.* found that the instantaneous velocity of cells was inversely proportional to the number of actin foci (Fig. 1.15B). It was also shown that the starved cells speed slightly decreases on surfaces of increasing adhesiveness (18), and other studies suggest a negative correlation between average speed and average traction force (28).

Dictyostelium cells adhere to extracellular matrix molecules and can also adhere to plain or coated solid materials. Cell adhesion has been thoroughly quantified by Bruckert *et al.* (64). By

submitting cells to radial hydrodynamic flows, they have shown that adhesion of *Dictyostelium* cells to glass is influenced by the composition of the medium bathing the cells. Coating the glass surface with components of the HL5 nutritive medium reduces the value of adhesion to one fifth of its value in Sörensen buffer (SB). Addition of 50 mM maltose (one component of HL5 medium) to SB decreases cell detachment threshold stress threefold (64). The simplest explanation is that a lectin[1]-like adhesion protein(s) could contribute significantly to non-specific adhesion to glass. Charges and hydrophobicity of the surface have also been shown to play an important role in *Dictyostelium* adhesion. In SB, a 4-fold increases in cell detachment was observed between glass substrate and positively charged surfaces (glass coated with a silane bearing NH_2-groups that are protonated at neutral pH, APTES, see section 2.2.2). Similarly, a glass coated with a hydrophobic silane (DDS) induce a 3-fold increases in cell detachment (64). Importantly, according to studies from this group, cell detachment depends on cell size and physico-chemical properties of the substrate, but is not affected by depolymerization of the actin cytoskeleton (using an analog of Latrunculin A). They emphasize the importance of detachment kinetic. We will come back on this point more specifically in the chapter 5.
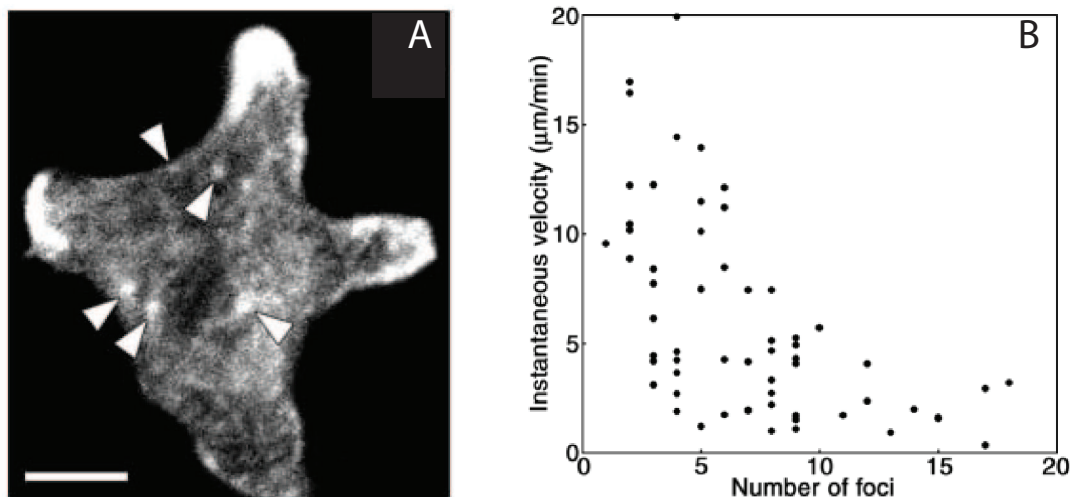
Figure 1.15: Actin Foci. (**A**) Distribution of actin. Several actin foci were observed on the ventral membrane of the cell. Scale bar: 5 μm. (**B**) The instantaneous velocity of cells was inversely proportional to the number of actin foci. The number of actin foci and instantaneous velocity were examined in sequential images of eight cells. From (61).

---

[1]Lectins are sugar-binding proteins involved in the regulation of cell adhesion in animals cells

1.4.2.4 Adhesion proteins in *Dictyostelium*

Several membrane proteins have been identified to mediate adhesion in *Dictyostelium* . Some of these proteins are similar to β-integrins (Sib proteins), which mediate interaction of eukaryotic cells with extracellular matrix proteins (65, 66). *Dictyostelium* also possesses many proteins known to be part of adhesion structures in higher eukaryotes, such as talin (67, 68), paxillin (69), coronin (70), ERMs, FAK, myosins (71), Phg1, Phg2 (72) and Src-like tyrosine kinase (73).

Phg2 seems to play a specific role in signaling actin polymerization and depolymerization at places where the amoeba comes into direct contact with a substrate (72). Paxillin[1] homologue is localized at actin foci and implicated in controlling cell-substrate interactions and cell movement (74). Talin null cells adhere weakly to substrate (72).

The receptor Phg1 is a hydrophilic receptor (75). As for now, the molecular nature of its ligand is unknown, but it is present in nutritive media, because Phg1 null mutants are adhesion defective in this medium. Cells lacking Phg1 protein are unable to bind to glass in the presence of HL5 medium, while in the presence of SB, the threshold stress is comparable to that of wild-type cells. The simplest explanation is that Phg1 is the only adhesion protein mediating *Dictyostelium* adhesion to glass when the plasma membrane lectins are saturated. The secondary structure of this protein is indeed suggestive of a receptor, having both extracellular and intracellular domains. Interestingly, several Phg1 isoforms are present in *Dictyostelium* genome and homologues are found in the Drosophila and human databases. The role of these proteins in the other species has not yet being determined.

Sib[2] proteins (65, 66) are transmembrane proteins involved in the adhesion of *Dictyostelium* cells and link to talin. Experiments of Cornillon *et al.* (66) suggest that SibA and SibC act as redundant adhesion molecules at the cell surface and that the variable levels of expression of SibC participate in the regulation of cell adhesion. When cells are cultured in suspension in Fresh medium, SibC is highly expressed, while it is down modulated when cells are adherent to petri dish in conditioned medium. Accordingly, SibA mutant cells are more sensitive than wild-type (WT) cells to these environmental cues (because their adhesion relies on SibC), while SibC mutant cells respond minimally to environmental cues because SibC expression is abrogated.

---

[1]Paxillin is a key regulator component of focal adhesion sites in mammalian cells
[2]Similar to Integrin β

Along with Sib protein, SadA[1] has been identified as a molecule of cell to substrate adhesion of *Dictyostelium* vegetative cells (76, 77). The cell-substrate adhesion protein SadA is active only during vegetative growth whereas SibA is constitutively expressed. The table 1.2 resume the localization and expression of main adhesion protein of *Dictyostelium* .

Dictyostelium protein	localization	cycle	References
Phg1	Transmembrane	not expressed in SibA mutant	(75)
Phg2	Transmembrane	not expressed in SibA mutant	(72)
SibA	Transmembrane	Vegetative only	(65, 66)
SibC	Transmembrane	Vegetative and starved cells	(65, 66)
SaDA	Transmembrane	Vegetative	(76, 77)
Paxillin	Internal	all stage; peaks during slug formation	(74)
Talin	Internal	all stage	(67, 68)

Table 1.2: Some proteins involved in *Dictyostelium* adhesion to substrate.

1.4.3 *Dictyostelium* and Quorum Sensing (QS)

There appear to exist factors secreted by cells in higher eukaryotes that function as quorum sensors[2], so that as the number or density of cells of a specific type increases in a tissue or the body, the concentration of the factor increases, allowing the cells to sense their number or density. QS[3] has been described in detail for many bacterial systems (78), fungi (79), *Dictyostelium* (80) and was recently suggested to regulate ovarian cancer metastasis (81). For instance, a major problem in treating cancer is the phenomenon of tumor dormancy: often, when a patient has a primary tumor and metastases, surgical removal of the primary tumor appears to stimulate cell proliferation in the metastatic foci. This postsurgery proliferation appears to be due to the tumor cells secreting an unknown quorum factor that inhibits their proliferation, so that when

---

[1]Substrate Adhesion Deficient A

[2]Quorum sensors are also known as cell density sensors

[3]Quorum Sensing. QS is accomplished by simultaneously secreting and sensing autocrine factors that accumulate in the extracellular space in a cell-density dependent manner.

1. INTRODUCTION

a major source of the quorum factor (the primary tumor) is removed, the resulting reduction in the levels of the factor allows the metastases to proliferate faster (80). QS mechanism has also been shown to play a role in wound healing and fibrosing diseases such as cardiac fibrosis, pulmonary fibrosis, and end-stage kidney disease (82). QS have been identified in human blood serum protein, and clinical trials using this secreted factor are currently underway (83). The simple *Dictyostelium* developmental cycle provides an excellent system in which to study eukaryotic QS. Understanding the mechanism of QS in cell model such as *Dictyostelium* is therefore of great interest and will hopefully help us to elucidate the physics and biochemistry of development in higher eukaryotes.

During growth, unicellular *Dictyostelium* amoebas monitor their cell density relative to that of their bacterial food source by secreting a glycoprotein called prestarvation factor (PSF) at a constant rate (80, 84). When the ratio of PSF relative to that of bacteria exceeds a certain threshold, cells stop proliferating and initiate the expression of early developmental genes like discoidin (in a dose-dependent manner) that are required for its aggregation and coordinate the initiation of multicellular development (85). It is important to note that PSF are not observed in the case of axenically growing *Dictyostelium* .

Early on during aggregation, gene expression requires the activity of cAMP-dependent protein kinase (PKA) (86), and a high PSF to food ratio is thought to upregulate the translation of the PKA catalytic subunit PKA-C (87, 88). Upon starvation, cells signal each other that they are starving by secreting an array of cell density-sensing factors such as the glycoprotein conditioned medium factor (CMF) (84, 89, 90). As more and more cells secrete this factor, the concentration of the factor rises, and when the concentration goes above a threshold, cells start aggregation with relayed pulses of cyclic adenosine monophosphate (cAMP) as a chemoattractant (91).

CMF stimulates gene expression in parallel with PSF, and both signals potentiate cAMP signaling by inducing genes involved in cAMP synthesis and detection (85, 92). The cAMP pulses also regulate the expression of many genes that are specific to early development.

For example, among the newly activated genes are those encoding adenylate cyclase A[1], cAMP receptors[2] and the extracellular cAMP phosphodiesterase PdsA which hydrolyzes cAMP. These proteins, together with PKA and RegA, an intracellular cAMP phosphodiesterase with response regulator, form a biochemical network that generates pulses of cAMP (93). Once

---

[1]ACA, an enzymes which synthesizes cAMP

[2]cARs, Gprotein coupled receptors that detect cAMP

these proteins are functioning, a few starving cells start to emit cAMP pulses. Surrounding cells respond by moving towards the cAMP source and by relaying the pulse to more distant cells. Chemotaxis and signal relay together then cause the rapid aggregation of cells into multicellular mounds. This process forms a number of groups of up to 10^5 cells. The top of the mound continues to emit cAMP pulses and is pushed upwards by the movement of cells underneath (94). The group size is controlled by counting factors (CF) that mediate cell density sensing during the late aggregation and regulate myosin II distribution, motility and cell adhesion (95).

More recently, Gomer *et al.* show that AprA and CfaD are secreted proteins that function as autocrine signals to inhibit cell proliferation of *Dictyostelium* in nutritive condition (82). In the AprA/CfaD system, a chalone[1] pathway was found where the chalone signal has two components that need each other for activity and thus act as message authenticators for each other. A quorum-sensing molecule (unfortunately not purified) was reported by Cornillon *et al.* to regulate cell adhesion in vegetative *Dictyostelium* cells (66). At high cellular densities, a strong decrease in cell adhesion and in the expression of the adhesion protein sibC was observed.

None of these studies have analyzed to our knowledge the role of Quorum Sensing on cell motion and cell shape in nutritive condition. In this manuscript, the role of Quorum-sensing factors in the regulation of cell motility has been unambiguously demonstrated, and will be described in detail in Chapter 3.

---

[1] any internal secretion that inhibits a physiological process or function

1. INTRODUCTION

Chapter 2

Protocols

In this chapter we present the tools we developed to study cell motility and cell detachment. We used large glass slides with 4 independent well allowing us to study simultaneously different parameter influencing cell migration. We developed a new microfluidic device to quantify cell adhesion and cell detachment kinetic. Statistical analysis was performed using Matlab software.

2.1 Motility

2.1.1 Strain & culture.

Dictyostelium DH1 were grown in HL5 medium (formedium, UK; composition in Tab. 2.1) in plastic culture dishes (Falcon, 10 cm diameter) at 21°C. Cells adhere to the plastic bottom of dish and feed by pinocytosis[1]. In this condition cell division is about 8 hours. We culture *Dictyostelium* DH1 cells as follow: we subculture when the cells are subconfluent or reach a maximal density of 1×10^6 cells/mL, which takes ~ 2 days, for DH1 strain. We then make a 1:100 to 1:200 dilution into 10 mL fresh HL5 medium and add to a new dish. Cell subculture has to be limited in time (~ 1 month) to avoid any spontaneous mutation and experimental reproductibility issues. A new *Dictyostelium* culture is start from a frozen stock of cells prepared before in the laboratory. After harvesting around 1×10^7 cells by centrifugation (600g for 5 min) of suspended cells confluent culture, we resuspend it in 1 mL of HL5 medium with 10% of Dimethyl sulfoxide[2] (DMSO) in a liquid nitrogen storage vials. Finally we store the vials in a $-80°C$ freezer.

	Peptone	Yeast Extract	Glucose	KH_2PO_4	Na_2HPO_4
g/L	14	7	13.5	0.5	0.5

Table 2.1: Nutrient medium HL5 composition (formedium)

2.1.2 Cell starvation.

Once cells are at confluence during standard culture procedure we wash the cells with 10 mL Development buffer (DB, see composition in Tab. 2.2) three times and concentrate them in 3 mL of DB (*i.e.* 2,4×10^6 cells/mL in a 3,5 cm petri dish, corresponding to a cell density of 2,4×10^5 cells/cm² and a cell-cell distance of 20 μm: cells are in contact with each other). Starvation time corresponds to the time the cell spent in concentrated DB.

---

[1]Pinocytosis is used primarily for the absorption of extracellular fluids. The cell takes in surrounding fluids, including all solutes present

[2]DMSO may also be used as a cryoprotectant, added to cell media to prevent cell death during the freezing process.

	Mw	g	mM	mL
$NA_2HPO_4, 2H_2O$	141.96	0.71	5	
KH_2PO_4	174.18	0.68	5	
H_2O				989
$MgSO_4$			0.002	10
$CaCl_2$			0.02	1

Table 2.2: Developmental buffer composition

2.1.3 Microscopy

Vegetative cells were harvested at a density of 1×10^6 cells/mL, suspended in fresh medium and plated on glass coverslip at various densities (between 50 cells/cm^2 and 3×10^4 cells/cm^2) at 21°C.
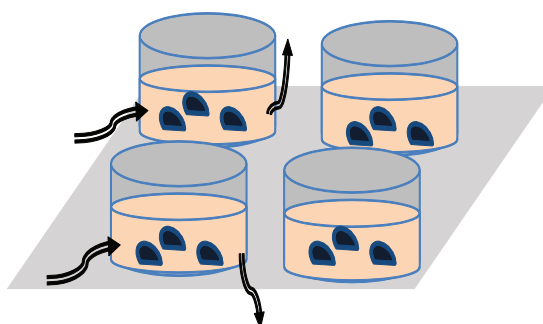
Figure 2.1: Cell migration device. Four wells with about 2 cm^2 surface are sealed on a glass slide and filled with 2 mL of medium or buffer. Medium can be eventually exchanged with our syringe pump (left). This setup allows the simultaneous recording of four different experimental conditions. Various parameters are the cell density, the substrate, the surrounding medium and cell strain.

Glass coverslips (Scientific Glass LABS LTD, 76x52 mm) were rinsed with 70% ethanol and HL5 medium. Custom-made wells (Fig. 2.1) were sealed on a glass coverslip allowing four different assays in parallel (each of area $S \simeq 6$cm^2, volume $V_0 \simeq 2$mL). Renewing the cell medium was possible using a syringe pump (PHD ULTRA infuse/withdraw, Harvard Apparatus) connected to one or two wells. Cells were observed with an inverted light microscope (Nikon TE2000) using a 4x objective (field of view 2.2×1.7 mm, at a resolution of 1.61 μm/px) in a home-made temperature-controlled chamber (21°C). A motorized x-y stage (Märzhäuser) enabled to record in parallel up to 20 regions (*e.g.*, 5 different regions in each well). Images

31

were captured at 30 seconds intervals for 8 to 12 hours with a cooled CCD camera (CoolSNAP HQ2 Monochrome Roper Scientific) and the dedicated TE2000 software NIS Elements AR.

2.1.4 Image Processing

Recorded movies were binarized (Fig. 2.2) using ImageJ software with a custom made macro. Binarized movies were analyzed using Matlab to obtain individual cells positions (mass centroïd position), size and orientation. In appendix A., noise on tracked positions due to camera and stage repositioning errors are carefully evaluated. From the mean-squared displacement of fixed dusts, we measured a total error of $\sigma_T \leq 1.5\mu$m.

Figure 2.2: Cell contour detection. Detail ($\approx 10\%$) of one field of view obtained by bright field microscopy using a 4x objective lens (**A**) which is superimposed with cell contours identified by our ImageJ script (**B**). In (**C**) the corresponding binary image is displayed.

2.1.5 Motility Assay

In typical motility assays, cells were placed on glass coverslips in a well filled with 2 mL of nutrient medium (nutritive conditions for vegetative cells) or DB buffer (starved conditions). After 1 hour letting cells settle on glass, they were tracked during 10 hours at $\Delta t = 30$ seconds intervals. In aging experiments, cells were tracked during 10 hours, resulting in 1200 images. Images are organized in stacks of 100 images as 50 minutes is the lowest time interval to get a reasonable diffusion coefficient (see chapter 3) An example of typical cell tracks is shown in Fig. 2.3.

Other 'Aging' experiments were performed using highly conditioned medium (HCM, from cell cultured during 24 hours) or moderately conditioned medium (MCM, from cell cultured at experimental density for 4 hours). For flow experiments, cell medium was renewed with fresh HL5 (experiments with vegetative cells of chapter 3) or fresh DB (experiments with starved cells of chapter 4) using either an exponential flow ramp renewing medium from 0 up to 0.5
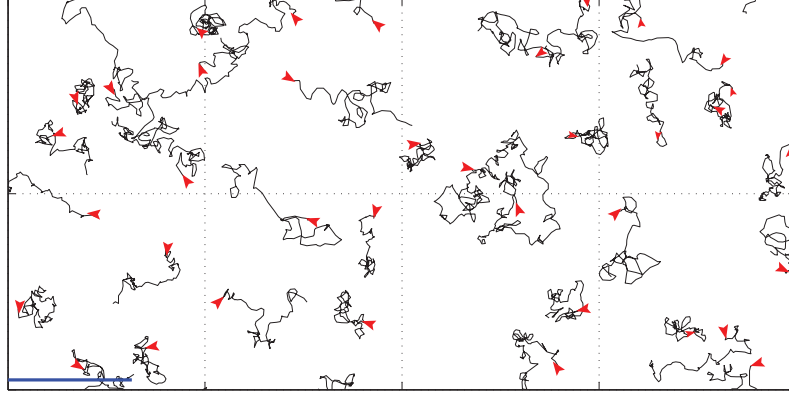
Figure 2.3: **Cell tracks.** Examples of cell trajectories lasting 50 min obtained at a cell density of 12000 cells/cm^2 in nutritive condition. Starting points are represented by red arrows. Scale Bar $= 100\mu$m.

mL/min either a constant flow rate renewing up to 2 mL/min.

2.1.6   Measurement of motion parameters

For a set of N cells tracked during $t_{tot} = N_{times}\Delta t$, the mean-squared displacement (*MSD*, see Appendix E.) is calculated as a function of the time lag t (see dark thick line in Fig. 2.4):

$$\langle \rho^2(t) \rangle = \langle (x_i(t_0+t) - x_i(t_0))^2 + (y_i(t_0+t) - y_i(t_0))^2 \rangle, \tag{2.1}$$

where we take the average over N and over all possible t_0 using overlapping intervals (96).

Standard deviation (SD) and standard error of the mean ($SEM = SD/\sqrt{N}$) are computed to evaluate error bars and dependence on timelapse microscopy parameters (time interval, number of cells..., see Chapter 3). We also calculated the *MSD* of individuals cells (see green lines in Fig. 2.4).

MSD were fitted with Eq.(3.1) for time larger than 5 min. Error on the fitted diffusion constant D was estimated from the SEM of the *MSD* at 15 min. We used the instantaneous velocity of the cell i at time t, $\vec{v}_i(t) = (\vec{r}_i(t+\Delta t) - \vec{r}_i(t))/\Delta t$ to calculate the normalized or non-normalized autocorrelation function of the velocity $C(t) = Z(t)/Z(0)$ and $Z(t) = \langle \vec{v}_i(t_0 + t).\vec{v}_i(t_0) \rangle$ respectively.

MSD can be represented in different forms (Fig. 2.5). We choose to represent cell migration as *MSD*/t throughout the manuscript for observational convenience. It shows clear difference
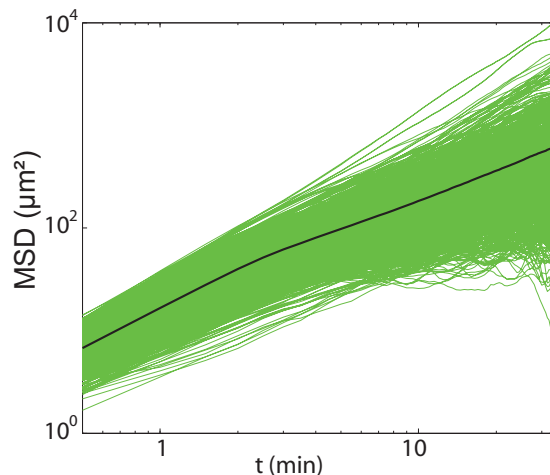
Figure 2.4: Mean Squared Displacement. Mean Square Displacement (*MSD*) as a function of time lag *t* in log-log scale. Green lines: individual *MSD* for each tracked cells, revealing the large dispersion of our population. Black bold line: Average *MSD* of all tracked cells
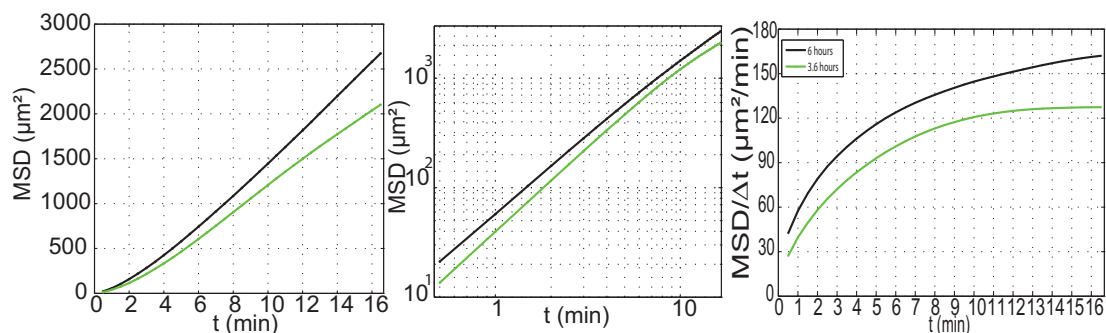
Figure 2.5: Mean Squared Displacement representation. *MSD* representation in a linear scale, a log-log scale and a representation of MSD/t as a function of time t. For two distinct situations: (*i*) normal diffusion at long times with persistence at short times (green line), (*ii*) apparent anomalous superdiffusion (at least during the recorded period, black line).

between 2 experiments and it easily exhibit whether cells have reached random diffusion at some time (a plateau is reached at long times, see Fig. 2.5). Note that the linear representation hides any eventual anomalous diffusion.

Bimodal analysis was performed as described in (97). Briefly, the turn angle ϕ was defined as the angle between 2 successive centroïd vector displacements. If, at least, 3 successive $|\phi|$ are below a threshold set as 45°, this portion of the trajectory is considered as persistent. Otherwise, it is random. An example of sorted trajectory using the bimodal analysis is represented

34
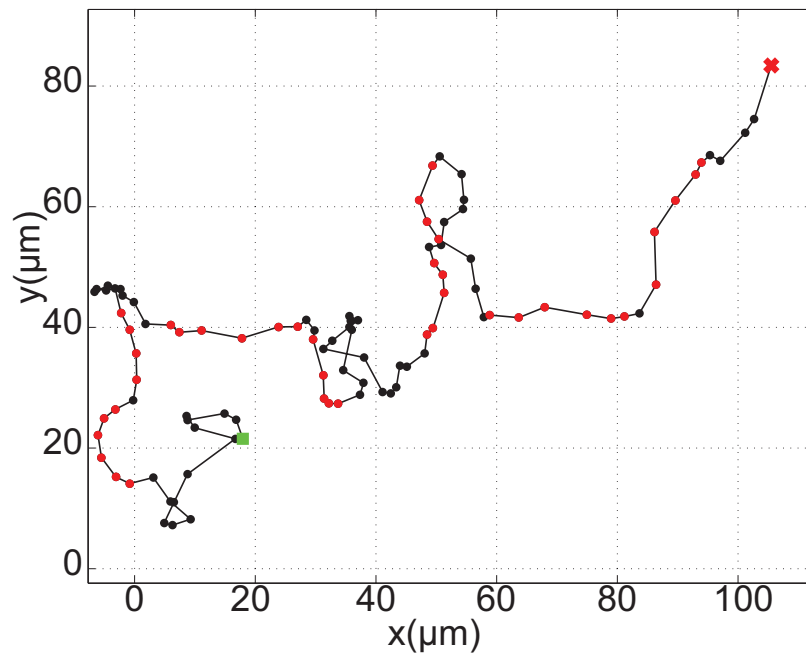
Figure 2.6: Cell tracking and Bimodal analysis. Typical tracks of persistent mode (in red) and random mode (in black) along a cell trajectory lasting 50 min (time step between two points, $\delta t = 30$ sec),starting point (green square).

in Fig. 2.6 with persistent tracks in red and random tracks in black. For each cell, we computed the proportion of time spent in persistent mode t_P/t_{tot}, the mean distance of each persistent track L_P and the total distance traveled in persistent mode $\sum L_P$. Error bars on these quantities represents SEM.

2.1.7 Statistical analysis

Wilcoxon non parametric tests were used to analyse statistical differences between groups. P values < 0.05 were considered significant (* indicating $p < 0.05$, ** indicating $p < 0.01$).

2.2 Adhesion

2.2.1 Device fabrication

We used standard multilayer photolithography procedures (98, 99) (see appendix D.) to create the microfluidic device with four parallel channels shown top-viewed in Fig. 2.7A.

The photo mask pattern as shown in Fig. 2.7B was drawn with CleWin4 (WieWeb software). The mask was transfered onto a glass plate as substrate. Firstly, we applied one negative photoresist layer (LAMINAR Aqueous Resist E9220, thickness 50 μm) and exposed it to UV light. This helps the further layers to stick properly. Then, 1, 2 or 3 layers of the same negative photoresist were put on the substrate and covered with the mask before exposing to UV light. This lead, after development with a carbonate solution (8.5 g CO_3^{2-}/L H_2O, heated to 67°C), to profile heights of 50, 100 or 150 μm respectively. We verified this height with a surface profiler.

The developed master was first silanized (ALDRICH Octadecyltrichlorosilane, 90+%) to ease unpinning PDMS afterwards, then covered with reticulating PDMS (10:1 ratio PDMS: reticulate, using SYLGARD 184 Silicone Elastomer and the associated curing agent), and baked for two hours at 75°C. The reticulated PDMS was ablated from the master, pierced for in-/outlets with a Harris Micro-puncher 0.5 mm diameter, treated with O_2-plasma (53 W, 2.5 min, 200 mTorr, distance from cathode about 5 cm) and irreversibly sealed to an equally treated clean glass plate (Scientific Glass LABS LTD, 76x52 mm, constituting the surface on which the cells adhere later). All operations so far had been done in a clean room (Team Microfluidics, Institut des Nanotechnologies de Lyon) to avoid contamination. Just after sealing, the channels were wetted with 0.22 μm-filtered ethanol to decrease surface tension and avoid bubble formation.
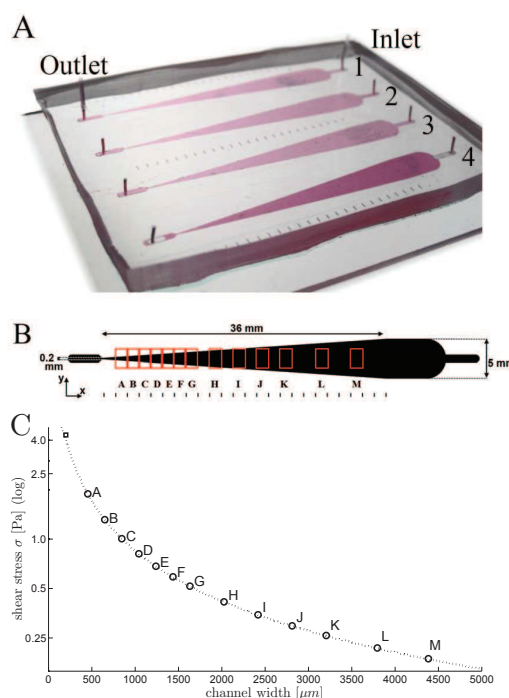
Figure 2.7: Microfluidic device with four independent branches. **A.** Photograph of the device, sealed on a 76x52 mm glass slide. The four channels are labeled with numbers. Inlet-outlet-distance is 50 mm. In- and outlet can be interchanged to avoid a high hydrodynamic pressure for large widths which occurs at the inlet site (see appendix B.). **B.** Photolithography mask (detail). The colored rectangles correspond to the visual field of different shear stress zones we used for our later discussed model experiment. **C.** Shear stress (log-scale) related to the position in the tapered channel for a low flow rate $Q = 5$ mL/h. The corresponding letters are represented in subfigure B. The square on the top left shows the highest possible shear stress that could be attained at this flow rate.

2.2.2 Channel coating

The glass surface was used directly or further coated with (3-Aminopropyl) Triethoxysilane (APTES, Sigma-Aldrich). For APTES-coating, 1% APTES in 5 mM aqueous acetic acid was injected in the chamber. A stop-and-go flow of the solution was maintained for 20 min. The APTES-coated channels were then washed with distilled water before drying at 100°C for 15 min. The channels were then thoroughly rinsed with fresh cell medium and used directly.

2.2.3 Flow creation

Both inlet and outlet of the four channels of our device were connected to flexible tubes (POR-TEX *Fine Bore Polythene Tubing* 0.28 mm inner diameter), the inlet being connected to a switchable T-connectic, allowing easy cleaning and exchanging of hand- and pump-driven syringes. The tightly closed system allowed a precise measurement of fluid flow by collecting and weighing the liquid that had passed by.

For precise flow control, we used a syringe pump (PHD ULTRA infuse/withdraw, Harvard Apparatus) with up to four BRAUN *Omnifix* 20 mL *Luer Lock* syringes. Of major importance were tight syringes with a rubber piston which shows no stick-and-slip behaviour, in order to assure a steady-going flow. With 20 mL syringes, experiments of up to 3 hours with a flow rate of $6 - 7$ mL/h could be easily managed.

2.2.4 Cell injection

Dictyostelium discoideum DH1 were grown in HL5 medium (formedium, UK) in plastic culture dishes (Falcon) at $21°C$ as explained above. Vegetative cells were harvested at a density of $1 \cdot 10^6$ cells/mL, suspended in fresh medium and injected into the microchannel via the channel outlet using a micro-pipette. A careful injection of about 24 μL into the outlet with the inlet being kept open was sufficient to obtain cell densities of $(4 \pm 1) \cdot 10^4$ cells/cm^2. The injected volume exceeds the volume of one channel (14 μL) to assure the coverage of those parts of the channel which are far from the injection point. A settling time at the surface of 30 min was chosen to enable cells to adhere to their substrate.

2.2.5 Microscopy

A low resolution 4x objective was chosen to get high statistics in single experiments. Images were captured automatically along a path scanning the different positions (and therefore the different applied stresses), as visualized schematically in Fig. 2.7B by colored rectangles. The microscopy setting and environment are the same as in the migration part. Images were captured automatically along a path scanning the different positions (and therefore the different applied stresses), as visualized schematically in Fig. 2.7B by colored rectangles. One image contained typically $500 - 1500$ cells. A scanning path with 52 positions (4 channels, 13 positions each) took about 45 s, which determined the temporal resolution of detachment kinetics recording. A lower number of channels and of positions per channel enabled much higher time
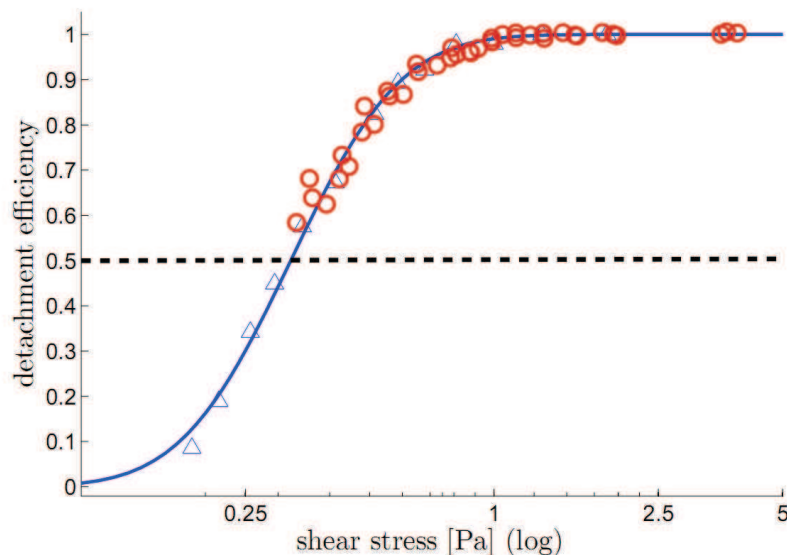
Figure 2.8: Detachment efficiency. The cumulative lognormal threshold-stress distribution function (cdf), fitted with eq. 5.4. Detachment efficiencies for *Dictyostelium* in fresh medium at flow rate Q = 5 mL/h (blue triangles and fit), and Q = 10 mL/h (red circles). Every datapoint for the *Dictyostelium* data in fresh medium corresponds to one position in Fig. 2.7. $\sigma_{1/2}$ can be read off at the point where the dashed line intersects the fits.

resolution. Higher spatial resolution (20x) but with lower statistics could be accomplished without change of the setting as well.

It turned out that setting out of focus the lenses delivered an optimal performance in practice: even if the precise cell shapes were not visible any longer, the cells were easier to distinguish from device impurities, thus facilitating subsequent cell counting. Typical images obtained are shown in Fig. 2.9.

2.2.6 Image Processing

To count the number of cells for each image and each timestep, the recorded movies were analyzed with the free, platform-independent program ImageJ using a custom-written batch algorithm based on the *Find maxima* routine which gave the number of cells (and the cell positions, if tracking was desired) for each image. It is therefore possible to represent the number of detached cells as a function of the shear stress applied to quantify cell adhesion (Fig. 2.8).The exact calculation of applied shear stress in such geometry is given in Appendix C. The superposition of 2 experiments of detachment at different shear flow shows the high reliability of

our device to quantify cell adhesion (Fig. 2.8).

The data obtained were further analyzed with a single MATLAB program which calculated the cell density (in cells/cm^2), the cell detachment in dependence of time and the parameters which characterize a cell population and its detachment kinetics (see Chapter 5). We thereby used the free MATLAB fitting toolbox EzyFit.

2.2.7 Cell counting and wall shear stress reliabilities
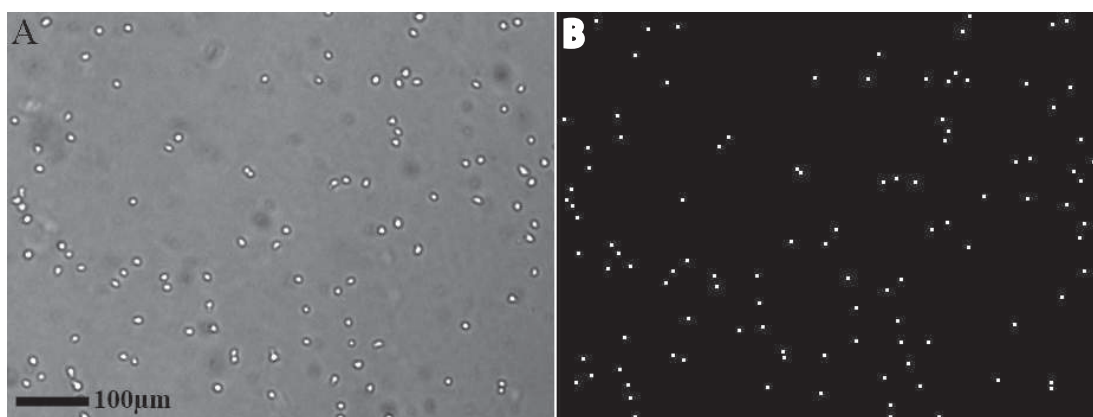
Figure 2.9: Detail ($\approx 10\%$) of one field of view within the microfluidic chamber before detachment by shear stress, using a 4x objective lens. The right hand side shows as single dots the cells identified by our ImageJ script.

Image acquisition with microscopy and treatment with ImageJ were done as described in detail in the previous section 2.2.5. Fig. 2.9 shows $\approx 10\%$ of a field of view. It shows the high reliability of our cell counting method for *Dictyostelium* .

Within the same program, error calculus was done, effecting error propagation for stress incertitudes and analysis of the statistical error due to finite number of cells, both by means of straightforward resampling methods (see Appendix B.). The MATLAB-Code with a working data sample is available upon request. The two main possible error sources affecting the measured number of detached cells and the estimated wall shear stress are discussed:

1. Statistical and counting errors (a limited number of cells creates a statistical error).

2. Physical incertitudes and device approximations of the wall shear stress (flow velocity field and thus shear stress values may be modified by PDMS deformation due to internal

pressure; temperature-dependency of viscosity can affect the shear stress as well; also channel width and thus shear stress are not constant over a given field of view).

Chapter 3

Vegetative cell Migration

In this chapter, *Dictyostelium* was used as a model system to investigate the interplay between spontaneous amoeboid cell motion in nutrient solution and cell density. Cell migration has been quantified thanks to large data set and analysis from statistical physics. This analysis shed light on the heterogeneity within a given cell population, and the necessity to use large number of cells and long recording time to get reliable information on cell motion. In average, motion is persistent for short periods of time ($t \leq 5min$), but normal diffusive behavior is recovered over longer time periods. The persistence times are positively correlated with the migrated distances. The adaptation of cell migration to cell density highlighted the role of a secreted quorum sensing factor (QSF) on cell migration. Using a simple model describing the balance between the rate of QSF creation and the rate of QSF dilution, we were able to gather all experimental results into a single master curve, showing a sharp cell transition between high and low motile behaviors with increasing QSF. This unambiguously demonstrates the central role played by QSF on amoeboid motion in the growth phase. Cell motion analysis in response to this QSF can then be a useful parameter to fully quantify and compare cell response in different conditions.

3.1   Introduction

Cell movement has been classically described as a persistent random walk following the Ornstein-Uhlenbeck process (100) (see Eq. 3.1). This model derives from Langevin equation of motion, with white-noise. Accordingly, cells follow a directed motion over a short time range, while recovering normal Brownian diffusion over longer periods. The cross-over defines a persistence time (101). More recently, many studies have pointed out the existence of anomalous behavior (*i.e.*, even at long time scale, the cell do not show Brownian motion) in mammalian cells (102), and amoebas (103). None of these studies has investigated nor suggested the role of quorum sensing (QS) mechanisms in the regulation of spontaneous cell movement. It is however interesting to note that in the absence of external signals (very diluted conditions), Li *et al.* (104) have found a much faster migration than others using the same cell type but a higher cell density (103, 105).

It is well known that individual *Dictyostelium* cells exhibit variable motile properties and that even their average properties are often changing from one experiment to the other depending on unidentified parameters (66, 95). It is therefore important to be able as much as possible to investigate the dependence of cell motile properties on different experimental parameters in parallel.

In this chapter we investigate in a quantitative manner the role of cell density on the random motion of vegetative cells using a very large data set. The role played by cell-density on spontaneous cell migration was analyzed thanks to statistical analysis of cell centroid displacement over time in different experimental conditions. First, cell density has been varied in a large range (from 50 cells/cm^2 to 3×10^4 cells/cm^2, density experiments) corresponding to mean cell-cell distances ranging from 1300 μm down to 70 μm). Second, the evolution of cell migration was analyzed over time (aging experiments), in conditioned media and under controlled flow conditions (flow experiments). We have characterized the motion with different parameters classically used for the analysis of motion of colloids in complex fluids or biological cells (mean square displacement, velocity autocorrelation, persistence time, bimodal analysis). Our results demonstrate the role of QS factors (QSF) secreted by cells in the spontaneous migration of amoeboid cells.

3.2 Results

3.2.1 A random motion with persistence

Dictyostelium cells were generally tracked during periods of 50 min. The motorized stage of the microscope performed a loop of up to 20 frames with a time interval of 30 sec between two loops. A first qualitative analysis of cell motion can be done by displaying trajectories with a common starting point (Fig. 3.1B and C).

This graph shows the absence of any bias in the trajectories and the amplitude of the fastest cells. For this particular experimental condition (*i.e.*, cells submitted to a perfusion flow at $Q = 30$ mL/h), in 50 min, the fastest cells are exploring a region of 150 μm in diameter. For another condition (*i.e.*, cells at similar density but without flow), cells are slower (the fastest cells are exploring a region of 75 μm in diameter) but still migrate randomly (Fig.3.1C).

To quantify the randomness of these trajectories, it is useful to compute mean squared displacements (*MSD*, see Eq. 2.1, the calculus is given in appendix E.). This can be done for each cell (represented as a green line in Fig. 3.1E) and a mean *MSD* can be computed (thick black line in Fig. 3.1E). These individual *MSD* are log-normally distributed. The first striking characteristic is the large dispersion of individual *MSDs* already noticed a long time ago in the pioneering work of Potel and MacKay (106).

Due to the stochastic nature of both diffusion process and cell migration, large statistical variances are expected, even for very precise measurements (107). According to Qian *et al.*, large variances may also arise from the finite number of cells N, the time interval Δt between two recorded images and the total recording time t_{tot}. We analyzed the effect of these different parameters on the variance of the computed diffusion constant (Fig.3.2).

The standard deviation SD of the effective diffusion constant ($D_{eff} = MSD/4t$ at $t = 15$ min) is calculated as a function of N with a random sampling of N trajectories over the 1280 cells tracked for this particular experiment (other parameters: $t_{tot} = 50$ min, $\Delta t = 30$ sec). It does not depend on the number of cells N used for the statistics (Fig.3.2A, Inset). The standard error of the mean (SEM) and the relative standard error (RSE=SEM/mean) on the *MSD* are therefore decreasing with N as $N^{-1/2}$. The RSE is about 4.5% at $N = 900$, 13.5% at $N = 100$ and increases dramatically if $N \leq 50$ (Fig.3.2A). A large statistics is therefore essential to get accurate *MSD* values.
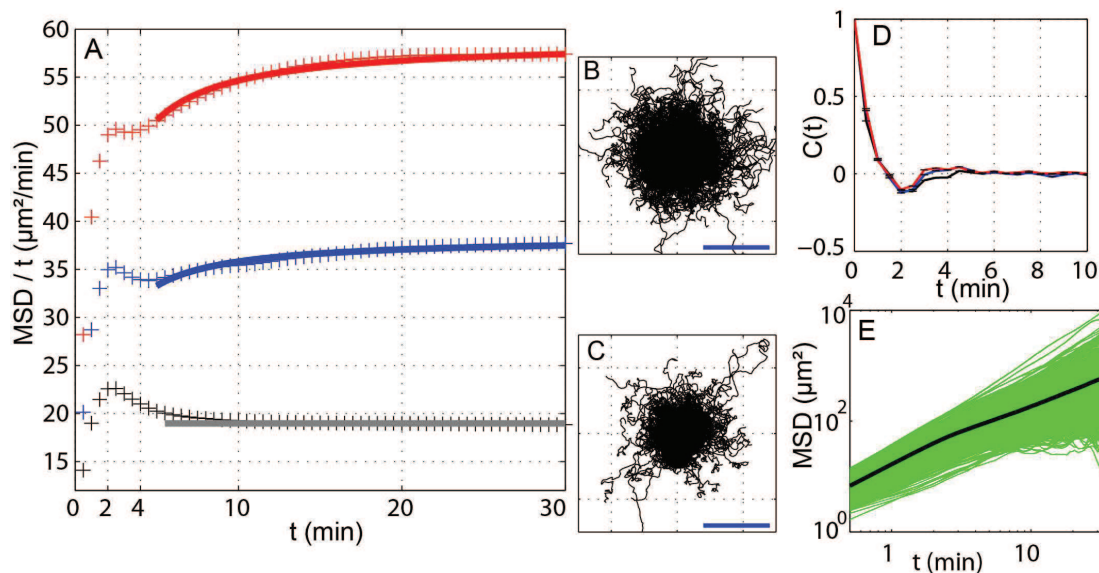
Figure 3.1: Cell track analysis. (**A**) *MSD* divided by time lag as a function of time lag for 3 typical cell conditions: red crosses, fast moving cells $D = 14.7 \mu m^2/min$; blue crosses, intermediate moving cells $D = 9.6 \mu m^2/min$; black crosses: slow moving cells $D = 4.7 \mu m^2/min$. Solid line are fits with the Fürth's formula. This plot reveals an overshoot at 2 min. The slower the cells, the larger the overshoot; (**B-C**) Typical cell tracks, with their origins brought to a common point, are shown for (**B**) a condition of fast cell displacement (under a perfusion flow of 30 mL/h), and (**C**) a condition of slow cell displacement (same cell density without flow). (Scale Bar= $100 \mu m$); (**D**) Velocity autocorrelation C(t) as a function of time lag for the same cell conditions as (**A**), showing a negative peak at 2 min; (**E**) Mean Square Displacement (*MSD*) as a function of time lag t in log-log scale. Green lines: individual *MSD* for each tracked cells, revealing the large dispersion of our population. Black bold line: Average *MSD* of all tracked cells.

The evolution of SD with the recording time t_{tot} was also computed (Fig.3.2B). The *SD* of three different effective diffusion constants ($D_{eff} = MSD/4t$, with time of interest equals 5, 15 and 30 min respectively) remains stable for recording time larger than around 3 times the time of interest. As it is important to compute *MSD* up to times where cell motion recovered normal diffusion, it confirms that a long recording time is compulsory to analyze cell motion exhibiting long persistence time (96). In our case, the maximum persistence time was found to be around 5 min, and the MSD/t curve exhibits clear asymptotic behavior for time larger than 15 min. A minimum recording time of 45 min was thus chosen. As far as the time interval Δt is concerned, SD of the D_{eff} (with time of interest equals 15 min) was computed (Fig.3.2C). Importantly, the SD remains stable even for time interval $\Delta t = 5$ min. In conclusion, to get statistically relevant
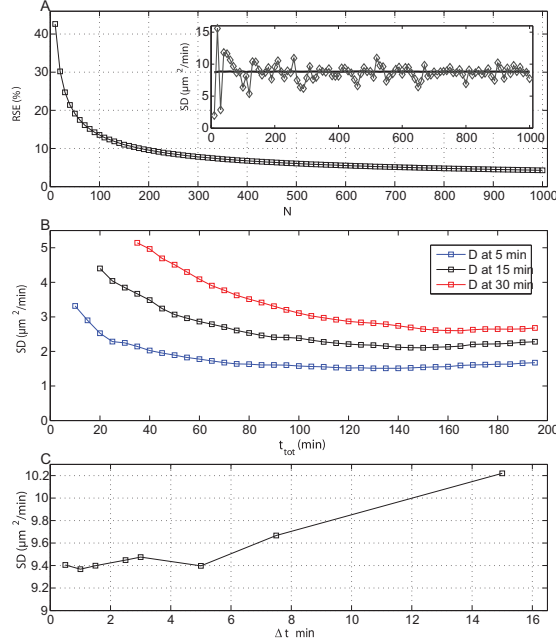
Figure 3.2: Error due to number of cell N, total time t_{tot} and time interval Δt. (**A**) RSE of $D_{eff} = MSD/4t$ at $t = 15$ min *Vs. N* calculated by generating and averaging 1000 ramdom samples of N among the full recorded cells. Inset: Standard deviation of D_{eff} *Vs. N* (same procedure). The black line represent the average of 1000 random samples and diamonds a single random sample. (**B**) Standard deviation *Vs. t_{tot}* for D_{eff} calculated at 5 min (blue), 15 min (black) and 30 min (red). (**C**) Standard Deviation of D_{eff} calculated at 15 min as a function of time interval Δt.

results on the diffusive behavior of cell motion, it is important *(i)* to analyze *MSD* of a large number of cells (typically larger than 500), *(ii)* to record cell motion during a time larger than 8-10 times the expected persistence time, *(iii)* a time interval of the order of the persistence time is sufficient. The use of smaller time interval does not increase the accuracy of the results.

For each condition analyzed, the plot of the mean *MSD Vs.* time lag t shows two apparent slopes in a log-log scale (Fig. 3.1E). It is linear at long times ($t \geq 20min$) indicating normal (random) diffusion. At short times, it scales as t^β with an exponent β larger than one indicating a persistent motion. However data cannot be fitted over all times with the standard expression of random motion with persistence relation (Fürth's formula) (100):

$$\langle \rho^2(t) \rangle = 4D \left(t - P \left(1 - e^{-t/P} \right) \right) \tag{3.1}$$

where D and P are the diffusion constant and persistent time respectively. This is clearly evidenced by a *MSD/t* representation (Fig. 3.1A) which shows the presence of an initial overshoot

near about $t = 2$ min. This overshoot has never been reported to our knowledge in previous studies but the reason could be that the MSD/t representation is not classically used. In log-log or linear MSD plots, we cannot indeed notice this singularity.

The presence of this overshoot is correlated with the presence of a negative peak in the velocity autocorrelation function ($C(t)$) near 2 min (Fig. 3.1D). We have carefully checked that both are not due to noise on centroid positions due to stage repositioning or camera errors (Fig. 5 in appendix A.). The negative peak of $C(t)$ corresponds to an excess of turn angles larger than 90° near 2 min: there is a significant probability that a cell moving in a given direction retracts backward after two minutes. It will be interesting to analyze pseudopod activity for those cells by using a larger spatial and temporal resolution but we could not perform this analysis during this thesis.

For times greater than 2 min, the cell centroïd displacements show some slight persistence as velocity autocorrelation is significantly larger than zero especially for fast moving cells (red curve in Fig .3.1D). For times much larger than the overshoot, it is possible to get a reasonable estimate of the persistence P and of the diffusion constant D by fitting the mean MSD with the Fürth's formula. The reported value of D throughout the manuscript correspond to values obtained by fitting data with a lower cut-off at $t = 5min$. The fit indicate that the larger the diffusion constant D, the larger is the persistence time, P (Fig.3.3A). Assuming a linear correlation between these two fitted parameters, we can estimate an intrinsic instantaneous speed $S = \sqrt{2D/P} = 4.3 \mu$m/min from the slope. The existence of a linear relation would indicate that the long term migrated distance is caused by the ability of cells to maintain movement in a chosen direction, not by the increase in their intrinsic speed.

3.2.2 Bimodal analysis

We also analyzed the statistics of the persistence portions of the trajectories with a bimodal analysis (see chapter 2 which was reported to be very helpful to describe the different kinds of motility from random to directed (97, 108). The bimodal analysis is based on the condition that three successive directional angle are below an arbitrary threshold. The arbitrary cut-off value of 45° used in Bimodal analysis is compatible with the maximum fluctuations in cell direction of persistent portions of *Dictyostelium* cells (104). Fig.3.3B-D show the relation between D and the proportion of time spent in persistent mode t_P/t_{tot}, the mean persistent run length L_P or the cumulated distance in the persistent mode $\sum L_P$ respectively. Each point corresponds to the average value over all cells of a given experiments. Experiments with faster cells have a larger mean t_P/t_{tot} but also a larger L_P. As a result the cumulated distance migrated in the persistence mode which is a combination of both t_P/t_{tot} and L_P is very dependent on the conditions. The bimodal analysis may be also performed for each cells and the distribution of persistent parameters for the whole cells of a given experiment may be calculated. Cell distributions obtained from 3 typical cell conditions (from fast to slow migrated distance) are shown in Fig. 3.4. Histograms can be accurately fitted with a Gaussian distribution. Even if the distribution is very large, clear differences of the average values of each persistence parameters are found. This bimodal analysis confirms the strong correlation between persistence and diffusion constant.
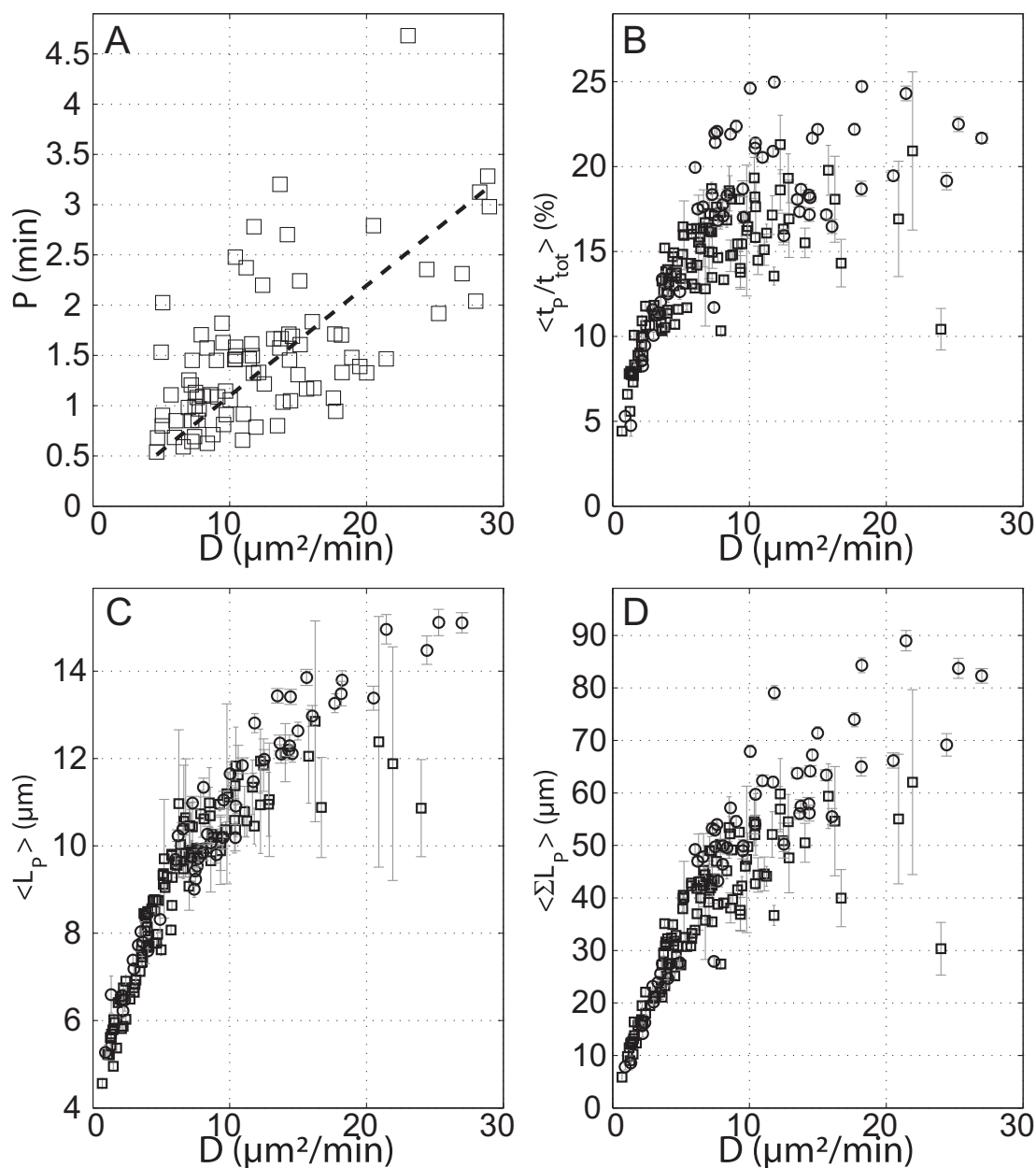
Figure 3.3: Cell persistence is correlated with Diffusion Coefficient D. All variables are plotted as a function of D which is obtained (as well as the persistence time P) by fitting MSD with the Fürth's formula at long times ($t \geq 5min$). (**A**) Persistence time P (values larger than the time interval of 30 sec were considered); (**B-C-D**) Parameters obtained from a bimodal analysis; (**B**) Ratio of time spent in persistent mode over total tracking time; (**C**) Length of persistence L_P (distance end-to-end of each individual persistent portion of cell trajectory); (**D**) cumulative L_P, summed over all cell trajectory. Squares correspond to 'Aging' experiments, circles to Flow experiments. $\langle \rangle$ denotes averaging over all tracked cells in a given condition. Error bars represents SEM. The solid line in (**A**) is a linear fit $P = aD$ ($a = 0.11$, $R^2 = 0.54$).
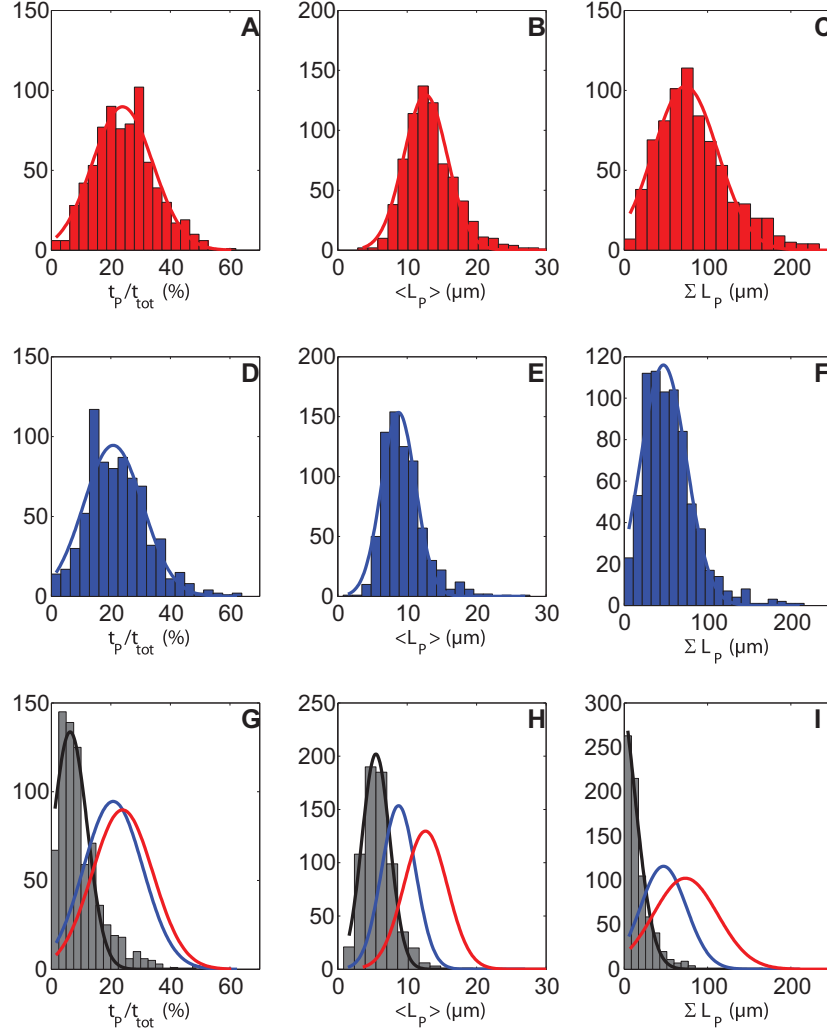
Figure 3.4: Individual cell distributions of the persistence parameters obtained from a bimodal analysis. t_P/t_{tot} is the proportion of time spent in persistent mode, L_P is the mean persistent run length and $\sum L_P$ the cumulated distance in the persistent mode. Three different experiments corresponding to the ones of Fig. 3.1A are represented: in red (**A-C**), histograms of fast moving cells; in blue (**D-F**),histograms of cell moving at intermediate speed; in gray (**G-I**), histograms of slow moving cells. The solid line is a fit of each histogram with a Gaussian function. All fits of a given parameter are superimposed in (**G-I**) to better visualize the differences between the three experiments. Histogram reveals large distribution of cells within an experiment but clear differences between mean values of each parameters, reinforcing the use of large statistics to describe cell motility. The faster the cells, the larger are the persistence parameters.

3.2.3 Cell shape and cell migration are correlated

Although we used a low spatial and temporal resolution (1.59μm/pix and 30 sec respectively), the overall cell shape as well as main modes of deformation can be easily detected by our ImageJ script (Fig.2.2). Two typical fast and slow cells are displayed in Fig. 3.5A. Cell shape were here characterized with the roundness parameter r ($r = 1$ indicates a circular cell, $r << 1$ a very elongated cell). The larger the diffusion constant, the lower the roundness parameter r (Fig.3.5B). The diffusion constant D was found to be positively correlated with the changes in roundness Δr during 30 sec (Fig.3.5C) indicating that fast vegetative cells (see red box) were also changing frequently their overall shape between a long and a more rounded shape while slow cells remained mostly rounded because they were extending very small protrusions (see blue box).
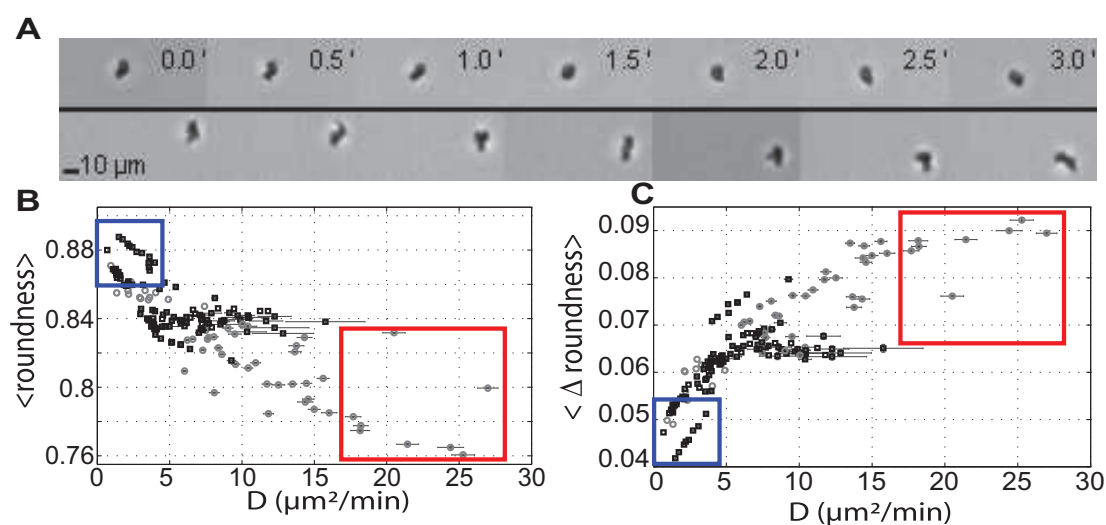
Figure 3.5: Cell shape is correlated with migrated distance. (**A)** time lapse of 2 cells (upper and lower rows: slow and fast, respectively). Despite the low resolution, we can distinguish easily that the fast cell is more elongated and more active than the slow cell. Cell roundness (**B)** and roundness difference (**C)** between two successive images are correlated with the diffusion constant (positively and negatively respectively). Squares correspond to aging experiments, circles to experiments with a flow. The two colored boxes highlight two special groups of cells, very slow and fast respectively. Roundness is defined as $2(\sqrt{A/\pi})/M$ where A is the cell area and M the cell major axis length (both are determined with Matlab). Each point corresponds to the average over all cells tracked during a single experiment. The more elongated the cells are (Roundness< 1) the faster they move. Roundness difference quantify the cell deformation activity. The larger is this activity, the faster move the cells.

3.2.4 Cells move faster at low cell density

It is well known that starved cells acquire aggregation competence by exchanging signals with others at high cell density (109). Aggregation competent cells are highly polarized, very persistent and move fast (28). Surprisingly, vegetative cells behave in the opposite way: they move faster at low cell density. We checked this by measuring the mean *MSD* in a wide range of cell densities between 50 and $3.10^4 cells/cm^2$ (Fig.3.6A). The diffusion constant at the lower investigated density is five times larger than at the highest density. Differences are statistically significant (see inset of Fig.3.6A).
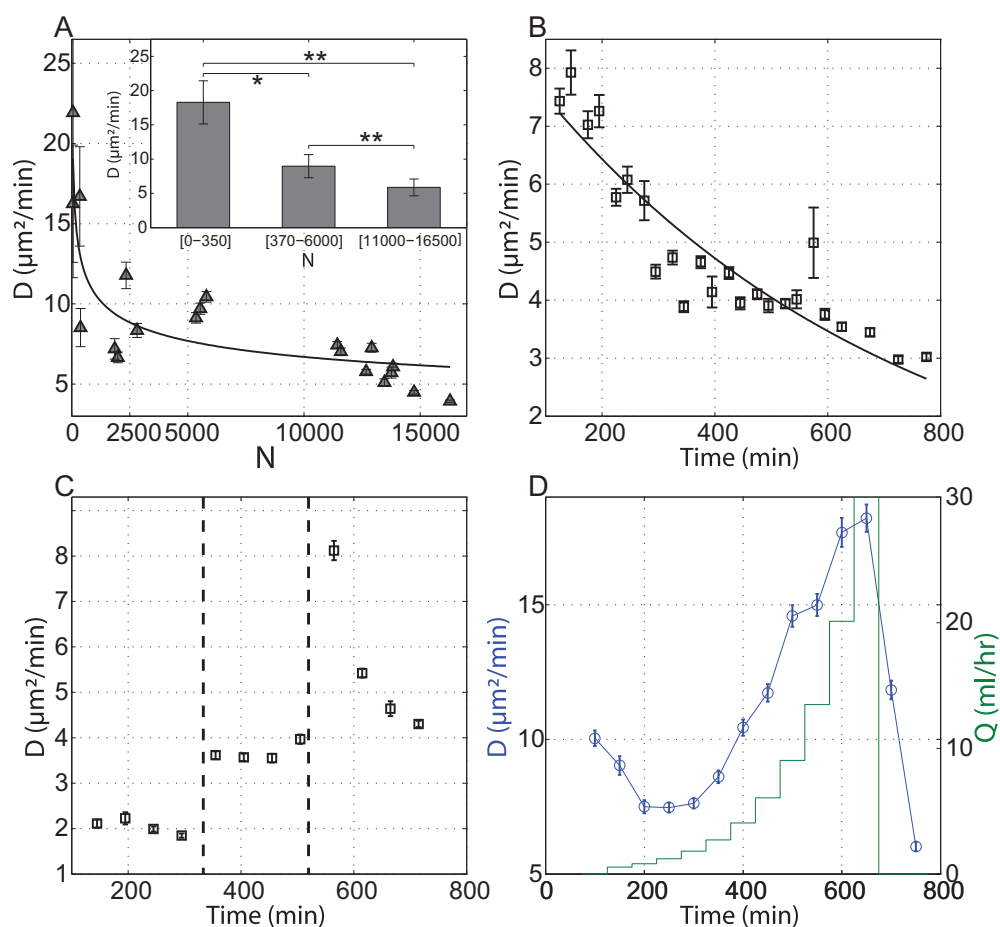
Figure 3.6: Cell motility depends on a QSF secreted by cells. The diffusion coefficient D is decreasing with cell density and experimental time, highlighting the role played by a QSF factors in cell motion. Error bars represent SEM. (**A**) D plotted as a function of the experimental cell density. Cells were recorded during 50 min, 1.5 hours after cells were washed in a fresh HL5 medium. Inset: Average D values and corresponding SD error bars obtained for different cell density ranges; (**B**) 'Aging' assay: as time increases QSF increases and D decreases; (**C**), Evolution of D when medium is changed during experiment starting from Highly conditioned Medium (left part, during time [150-300 min], low D), moderate conditioned medium (middle part, during time [350-500 min], intermediate D) and fresh medium (right part, during time [550-700 min], rapid increase in D, followed by an exponential decrease); (**D**) Evolution of D with flow Q. A home-made macrofluidic chamber enables renewing the flow. Applied flow is changed with exponential step (green line, vertical right axis). D is first decreasing (corresponding to a state where QSF cell emission is overcoming QSF flow dilution), then increasing (corresponding to a state where QSF flow dilution is overcoming QSF cell emission). When flow is stopped after 700 min, D rapidly decreases (corresponding to a rapid increase in QSF concentration)

3.2.5 Cell migration is regulated by a QS factor secreted by cells

Several tests were performed in order to check whether the dependence of cell migration on cell density could be regulated by an unknown factor secreted by cells.

First, we measured the evolution of the *MSD* over time ("aging" experiments). For that, cell trajectories were continuously recorded during 12 hours and the *MSD* calculated during time intervals of 50 min. Time zero corresponds to the time when cells were washed and plated on the sample dish in fresh HL5 medium. The diffusion constant D decreases from 8 to 3 μm^2/min over 12 hours (Fig.3.6B) whereas initial cell density is $9000 cells/cm^2$ at $t = 0$. Clearly this change is not accounted for by the increase of the cell population (due to cell division) which is roughly only doubling during that experimental period, corresponding to a minor effect on D at a given time (Fig.3.6A), and suggests the presence of a factor secreted by the cells over time.

Second, we studied the effect of various conditioned media (Fig.3.6C). Highly conditioned medium (HCM) conditioned by growing cells in the exponential phase during 2 days strongly reduces D at 2μm^2/min as compared to cells at the same density ($C = 12000$ cells/cm^2) in fresh medium (Fig.3.6A). Notice that D is very stable over 200 min. After that period of time, the medium of the same sample dish was exchanged for a moderately conditioned medium (MCM conditioned by cells at the same sample density, $C = 12000$ cells/cm^2 during 4 hours). This exchange induced an increase of D up to 4μm^2/min with little change during 200 min. This value is equal to the one obtained after the same period for aging experiments (Fig.3.6B). Finally, the medium was once more exchanged to fresh HL5 and D suddenly jumped to 8μm^2/min and slowly decreased with time with the same dynamics than in aging experiments (Fig.3.6B). These experiments indicate that *(i)* the more conditioned the medium the slower the cell migration, *(ii)* migration rate saturates at very large conditioning and *(iii)* cells quickly reset their migrating properties as soon as buffer is modified (within the 50 min time interval necessary to record reliable *MSD* measurements).

Third, we perfused the sample dish with fresh medium with series of steps of increasing, albeit slow, flow rates (Fig.3.6D). The duration of each step was 50 min and its amplitude roughly exponentially increasing up to $30 mL/hours$ where flow was stopped while cell trajectories were still recorded. With a high initial density ($C = 12000 cells/cm^2$) and for very slow flow rates (3 first steps), D is first decreasing but afterwards it increases with increasing Q up to 18μm^2/min. Once the flow is stopped D immediately falls down. It is known that shear

stresses above 0.1 Pa trigger active actin cytoskeleton remodeling and shear-flow induced velocity along the flow direction (110). In our experiments, the higher applied wall shear stresses ($\sigma \simeq \eta Q/Wh^2$ where η, h and w are medium viscosity, dish height and width respectively) are much smaller, in the mPa range. We also checked that trajectories of perfused cell are isotropic (Fig.3.1B) excluding therefore any shear-flow induced effect.

All these experiments unambiguously demonstrate that cells are sensitive to an unknown quorum sensing factor (QSF) secreted by cells. This QSF accumulates in the medium (aging experiments), can be partially removed by an external flow (dilution) or can be concentrated up to level saturating cells (highly conditioned medium).

3.2.6 A simple kinetics model to describe the QSF concentration for each experimental situation

With simple assumptions, it is possible to model the ratio of the number N_f of secreted QSF over some synthesis rate α. The first assumption is that N_f quickly reaches an equilibrium in the full sample volume. It holds if diffusion and or convection due to the motorized stage motion or the external perfusion if any are quickly equilibrating the density with respect to the typical 50 min experimental time for a *MSD* run. The second assumption is the hypothesis of exponential growth for the number of cells $N : N = N_0 exp(t/\tau)$ with $\tau = T/ln2$. This assumption is well verified experimentally with $T \simeq 8$ hours even for cells in the experimental sample dish (3.7).
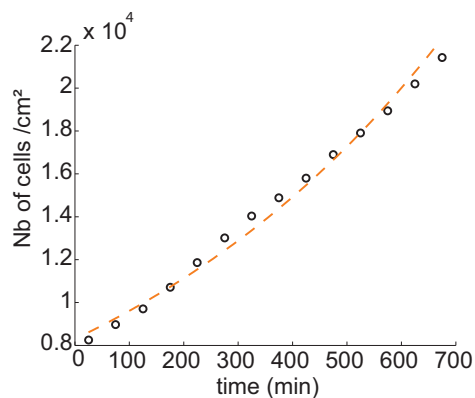
Figure 3.7: Cell growth. *Dictyostelium* cell proliferation is not affected by experimental condition. Cells migrating in HL5 on glass substrate are counted every 50 min (black circles). the number of cells is fitted by $N = N_0 exp(t \cdot ln(2)/T)$ (orange line) with a doubling time $T \sim 8$ hours.

If we assume that the number N_f of secreted QSF quickly reaches an equilibrium in the full sample volume, the variation of N_f over time t is described by the following differential equation:

$$\frac{dN_f}{dt} = \frac{dN_f}{dt}\bigg|_{synthesis} + \frac{dN_f}{dt}\bigg|_{dilution} \tag{3.2}$$

The right term represents a competition between the synthesis of QSF by cells and the dilution of QSF by the applied flow in the well. The synthesis term depends linearly on the number of cells $N_c(t)$:

$$\frac{dN_f}{dt}\bigg|_{synthesis} = \alpha N_c(t) \tag{3.3}$$

where α is the rate of emission of QSF by cells (supposed constant). The dilution term is simply related to the applied flow rate Q and the sample well volume V_0:

$$\frac{dN_f}{dt}\bigg|_{dilution} = -\frac{QN_f}{V_0} \tag{3.4}$$

We assume a classical exponential growth to describe the number of cells $N_c(t)$:

$$N_c(t) = N_c(0).\exp(\frac{t}{\tau}) \tag{3.5}$$

where $N_c(0)$ is the initial number of cells at $t = 0$ and $\tau = T.ln(2)$ with T the doubling period. In the case of *aging experiments* ($Q = 0$) we obtain:

$$\frac{N_f(t)}{\alpha} = \tau.N_c(0).(\exp(\frac{t}{\tau}) - 1) \tag{3.6}$$

where t is the time after cells were plated in fresh medium ($N_f(0) = 0$). In the case of *flow experiments* we have:

$$\frac{N_f(t)}{\alpha} = \left\{ \tau.N_c(0).\left[1 - \exp(\frac{-t_A}{\tau}) - \frac{V_0}{V_0 + Q\tau} \right] \right\} \exp(\frac{-Qt}{V_0})$$
$$+ \left\{ \frac{N_c(0)V_0\tau}{V_0 + Q\tau} \right\} \exp(\frac{t}{\tau}) \tag{3.7}$$

where t_A is the waiting time before flow application ($\sim 1hour$), t the starting time, when the flow Q was applied and $N_c(0)$ the number of cells at $t = 0$.

The solution N_f/α is a sum of two exponentials. These two exponentials explain why D is first decreasing at low Q (aging is dominant) and increasing at high Q (dilution is dominant, Fig.3.6D). With these equations it is possible to represent all *MSD* measurements as a function of the same common variable N_f/α which spans over more than 6 decades (Fig.3.8). The
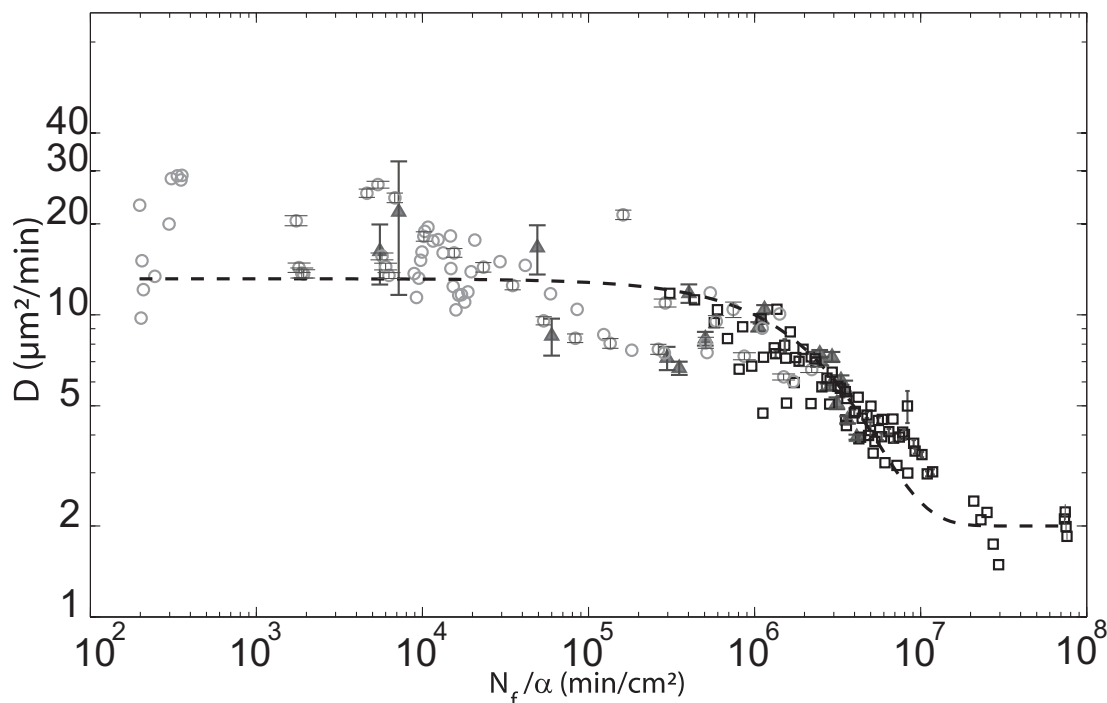
Figure 3.8: QSF density triggers cell motility: Merge of all experimental results. Diffusion Coefficient D is plotted as a function of calculated N_f / α (with α, the rate of QSF secretion) for all experimental points: 'aging' experiments (square), cell density experiments (triangle), flow experiments (circle). All data are well fitted by the following equation $D = D_0 exp(-N_f/(\alpha\lambda)) + D_{end}$; with $D_0 = 11.2\mu m^2/min$, $D_{end} = 2\mu m^2/min$, $\lambda = 3 \cdot 10^6$, $R^2 = 0.82$. For clarity we reported only error bars on 3 representative experiments.

agreement between very different types of experiments (variable initial cell density N_0, aging or experiment with a dilution rate) is very satisfactory. Interestingly the diffusion constant D shows two plateau values: a maximum value of about 12 $\mu m^2/min$ occurs at low QSF concentrations (very diluted cell density or dilution at high flows) while a minimum plateau value at 2 $\mu m^2/min$ occurs at large QSF concentrations (HCM or aging experiments at very long times).

3.2.7 Cells do not organize spatially at high density.

Even though experiments reported above indicate that cells regulate their motility according to a global QSF concentration, one may ask if cells detect their nearest neighbors and organize themselves accordingly.
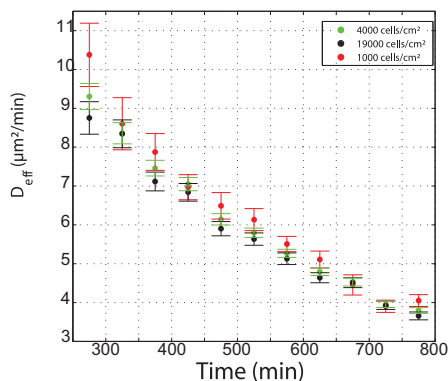
Figure 3.9: Effect of the local density. Local density has little effect if any on the effective diffusion constant defined from t=15 *min* as $D_{eff} = MSD(15')/(4 \times 15')$. Data originate from different regions of the same sample dish with different local cell densities. Red bullets correspond to the region of low local density (1000 cells/cm^2), black bullets to a high local density (19000 cells/cm^2) and green bullets correspond to a region with an intermediate density probably more representative of the mean density within the well (4000 cells/cm^2). Cells with a local low density move slightly faster than cells with a local higher density at least 2h after cells were transferred to fresh medium. The difference however is small as compared to the changes with time due to the aging effect.

To shed light on this question we first measured migration rates in sample dishes presenting an inhomogeneous cell density. Fig.3.9 shows that indeed cells with a low local density (red dots) move faster than cells with a high local density (black dots) at least 2*h* after cells were transferred to fresh medium. The difference however is small compared to the changes with time due to the aging effect (more than two-fold decrease of *D* during 500 min) and tends to vanish with time. This experiment indicates therefore that local QSF inhomogeneities quickly diffuse and cells mainly feel a global concentration of QSF. Finally, we checked that the diffusion constant value is independent of cell density in HCM. Very diluted cells (not shown) move with the same very low diffusion constant than cells at higher density (Fig. 3.6C) indicating that local cell-cell distances is not triggering the migrative properties of cells.

The second measurement is the pair correlation function $g(r)$ which quantifies the probability per unit length (normalized by the cell density) of finding another cell at a distance *r* from the reference cell. At short distances, $g(r)$ is zero due to the finite volume of cells. At long distances, a flat or an oscillating landscape may be encountered. A flat landscape at $g(r) = 1$
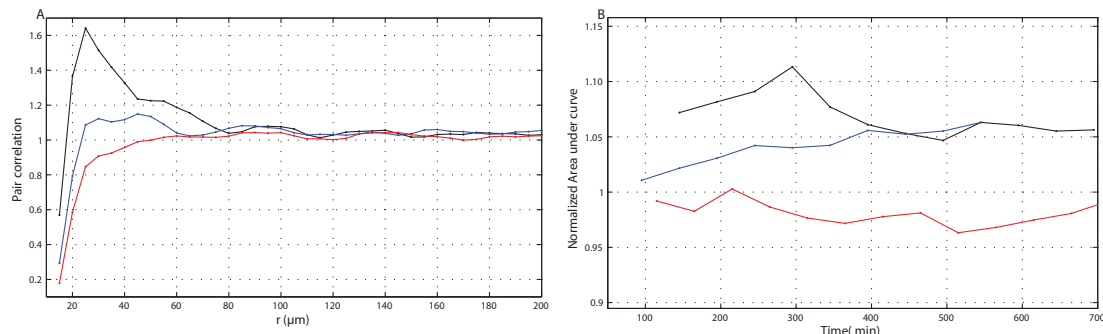
Figure 3.10: Pair correlation function analysis rules out any cell-cell structuration. Three typical experiments are presented: black line correspond to slow cells (conditioned medium experiment of Fig. 3C), blue line correspond to cells moving at intermediate speed (aging experiment) and red line to fast cells (flow experiment). The pair correlation function is defined as $g(r) = \langle \frac{n(r)}{\rho 4\pi r^2 \Delta r} \rangle_{cells}$ where $n(r)$ is the mean number of cells in a ring of width Δr at distance r, ρ is the mean cell density. **(A)** $g(r)$ at t=300 min for $\rho = 16000$cells/cm^2. Fast cells are randomly organized (flat landscape). Slow cells present a peak at $r = 25\mu$m which is significantly lower than the mean cell-cell distance obtained from the mean density ρ. This structuration is probably due to a lack of diffusion of cells after cell division (*i.e.*, clustering effect) not a real self-organization. **(B)** Normalized area under the curve defined as $\left(\int_{10}^{200} g(r) \, dr \right)/190$ as a function of time t. A value larger than one indicates an excess of cells with respect to the average density at short distance (*i.e.*, clustering effect). Clustering seems to progressively increase with age (see blue line, aging experiment). After $t = 300$ min for black line, HCM (highly conditioned medium from 2 days in culture) was exchanged to MCM (moderately conditioned medium for 4 hours) and cell clustering decreases toward the same level than a population that has been producing itself the same MCM medium (blue line). If the medium is continuously renewed (red line) the normalized area is close to one and does not change significantly with time.

indicates that cells are randomly distributed. An oscillating landscape indicates that they tend to occupy preferential positions because they feel each other. The first maximum in the curve corresponds to the mean nearest neighbor distance. Fast cells submitted to a constant flow do not show any structure indicating a completely random distribution (Red squares in Fig.3.10). Slow cells in HCM show a peak at about 25 μm. Cells moving at intermediate speed in HL5 show a less pronounced peak at about 40 μm. The location of these peaks is much smaller than the mean cell-cell distance calculated from the overall cell density (*i.e.*, 70 μm). The fact that the peak position increases with D indicates that it is related to a diffusion limited process: after a division, cells cannot separate significantly if they are too slow (*i.e.*, clustering effect). Clustering increases progressively with age and is very high in HCM (Fig. 3.10B). So far, these experiments do not support any self-organization of cells in territories.

3.3 Comparative motility study
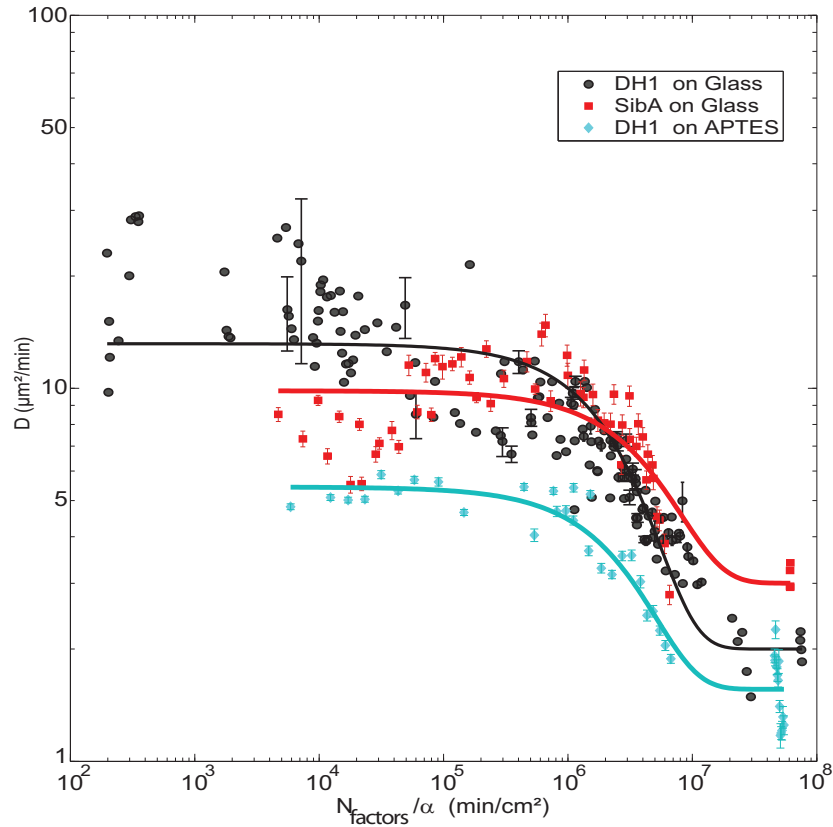
Figure 3.11: Quorum sensing factor triggers *Dictyostelium* migration. Diffusion Coefficient D is plotted as a function of calculated Nf/α. three different conditions are represented: wild type DH1 on glass substrate (black circles), SibA mutant (a subset of integrin like proteins is missing) on glass (red squares), Wild type DH1 on APTES-coated glass (cyan diamonds). All data are fitted (line) by the following equation $D = D_0 exp(-N_f/(\alpha\lambda)) + D_{end}$. Error bars represent SEM.

After having define a clear experimental frame and found that QS was involved in vegetative *Dictyostelium* motility we decided to test and quantify comparatively *Dictyostelium* on glass coated with APTES as well as *Dictyostelium* Ko-SibA mutant. We obtained the same correlation between the Diffusion coefficient and cell persistence as well as with cell shape. Fig. 3.11 show that the response to QSF (*i.e.* the sharp transition between fast and slow moving cells) is not altered for Ko-SibA mutant on glass nor wild type DH1 cells on APTES coated

glass. However, the plateau defining fast cells and slow cells (*i.e.* at very low or very high concentration of QSF, respectively) are different. The analysis of QS response appears thus as a robust parameter to compare quantitatively cell motility.

First, for low number of QS factors, *Dictyostelium* cells move faster on glass than on a surface bearing NH2 groups (APTES) (high motility at $D = 11.2$ vs. 3.9 μm^2/min for APTES and glass, respectively). The role of SibA protein in cell migration is also evidenced. For low number of QS factors, *Dictyostelium* cells are slow down if the SibA protein is not present ($D = 6.8$ μm^2/min vs. 11.2 μm^2/min for ko-SibA and wild type, respectively). For high number of QS factors, the differences vanishes, with a slightly higher motility for Ko-SibA cells compared to Wild-type cells as curves are crossing each other. It should be interesting to know if this difference arises from a difference in cell adhesion. *Dictyostelium* adhesion has been quantified during this thesis using a microfluidic system described in detail in chapter 5. Gathering information on chapter 3 and 5, preliminary scheme on the adhesion-migration interplay for amoeboid cells will be then discussed in the general conclusion.

3.4 Discussion

3.4.1 Presence and detection of Quorum Sensing Factors QSF

We have shown in this study that a number of QSF directly governs cell migration. Thanks to a simple model based on rate of secretion and dilution (due to flow), all data could be reasonably fitted by a single master curve (Fig.3.8). We mention again that data were obtained from a large set of independent experimental conditions (aging, constant and variable flow, stagnation, and conditioned media). Even with a very large variability in the individuals migrating properties, it is remarkable to see that the average migration rate is clearly governed by this QSF. The role played by such a factor in cell motility in the vegetative stage has never been reported to our knowledge. Even though we are unable to determine the absolute concentration of QSF in our experimental conditions, we can get information on cell sensitivity by analyzing the master curve. It is accurately fitted with an exponential decay with constant. For low QSF concentration, cells move with a constant high rate ($D = 11.2\mu$m^2/min) up to $N_f/\alpha = 3 \times 10^5$ min/cm^2. At this point, there is a sharp transition towards a lower rate of motion ($D = 2\mu$m^2/min), when $N_f/\alpha = 10^7$ min/cm^2. Using Eq. (3.6), we can estimate the corresponding cell density range for cells plated 2 hours before in fresh medium: from 2.5×10^3 cells/cm^2 to 2.5×10^4 cells/cm^2 corresponding to a mean cell-cell distance of 186 μm and 53 μm respectively. It is interesting

to compare the lower critical cell density (2.5×10^3 cells/cm^2) to the number of cells required for aggregation. It has been reported that a critical cell-cell distance of less than 100μm (*i.e.*, 10^4 cells/cm^2) is necessary for cells to relay signals during chemotaxis and form aggregation streams. Increasing the distance between cells hinders their capacity to sense each other and relay cAMP signals (111). Cells appear to have at least similar if not higher sensitivity to QSF than to cAMP. When cells are reaching the upper critical cell density (2.5×10^4 cells/cm^2), there is no further modification on cell motion, that stays low. This could be related to a saturation of receptors occupancy (equivalent to the one found during chemotaxis, where cell motility is depressed above a concentration in cAMP of 10 μM, corresponding approximately to 10^5 cells (55)).
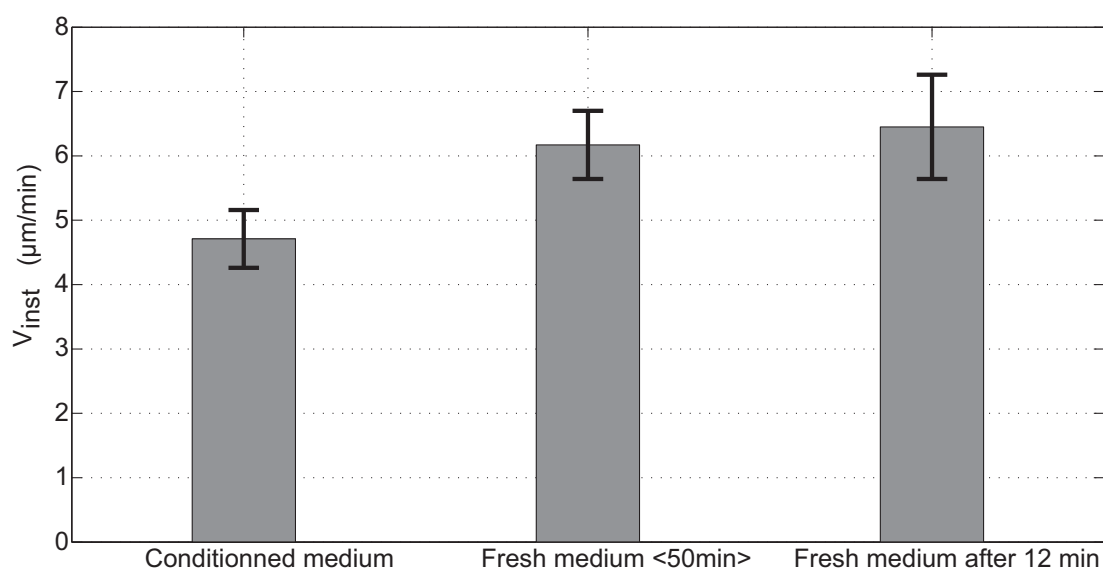
Figure 3.12: Fast response of cell speed to medium rapid exchange. Instantaneous cell speed is calculated as $v_{inst} = \sqrt{MSD(30\ sec)/30\ sec}$. Speed was first averaged during 50 min in highly conditioned medium (HCM, 1st bar) and in fresh medium (2nd bar). The third bar corresponds to a speed calculated between 10 and 12 min after HCM medium was exchanged to fresh medium while the second bar corresponds to an average value between 10 and 60 min after HCM was exchanged. The speed after changing HCM is largely increased especially when it is calculated immediately after the medium exchange (3rd bar).

It has to be pointed out that local cell density has a small influence on cell migration speed compared to the global concentration of QSF factor (Fig.3.9) and that we could not detect any self-organization of cells in territories (Fig.3.10). This is similar to chemotaxis, where sig-

nals relayed during aggregation (and hence locally modified with cell density) do not regulate individual cell speed (111). We do not know at this stage the exact nature of this QSF. It is admitted that gene regulation for synthesis of proteins usually takes about 30 min whereas protein phosporylation takes about 2 min [1]. A preliminary experiment suggests that it is not a protein synthesis. When changing the medium of experimental chamber from conditioned medium to fresh medium within 12 minutes the instantaneous velocity is significantly increased (Fig. 3.12). Several tests are now necessary to determine the size of this QS factor (to know whether it is a protein or a molecule, thanks to dialysis or ultracentrifugation technique), and its electrostatic and hydrophobic affinity (thanks to exchange resins). Also, it should be interesting in future studies to analyze if this effect is related to the quorum-sensing mechanisms regulating adhesion found by Cornillon *et al.* (66). Indeed, adhesion and migration are closely related in mammalian cells (112), and presumably also in *Dictyostelium* (61). First results analyzing the effect of QSF on adhesion are shown in chapter 5.

3.4.2 Consensual and novel aspects of *Dictyostelium* dynamics.

It is difficult to compare quantitatively the numerous studies on *Dictyostelium* cell motion as experimental conditions (substrate, cell density, strain, buffer composition) were different. A general trend however is that amoeboid cells exhibit a correlated random walk: the direction of a cell's current movement is correlated with that of its movement in the past, and cells therefore move with persistence (106, 113, 114). Van Haastert and Bosgraaf have extensively studied the ordered extension of pseudopods and found that they are of two types (115): *(i)* splitting pseudopods extended at small angles and preferentially alternating to the right and left, causing the cell to take a persistent zigzag trajectory; *(ii)* de novo pseudopods extended in a random direction. The ratio of splitting pseudopods to de novo pseudopods determines the persistence of cell movement. Starved cells are faster than vegetative cells not by extending more pseudopods and/or increasing their speed but by moving longer in the same direction (116). At small times, cells exhibit a complex dynamics with no simple exponential decay of the velocity autocorrelation and non Gaussian velocity distribution (103, 104, 105, 114). At large times, in the case of aggregation competent cells, cells might be attracted by some nascent aggregation centers eventually not visible outside the recorded field of view. In the absence of

---

[1]C.Anjard, personal communication

external signals, *MSDs* become satisfactorily fitted by the simple Fürth's formula (Eq.(3.1)) at times much larger than the persistent time (104). If the experiments do not last long enough to self-average properly and to detect the long term features of highly persistent cells, it is difficult to distinguish true superdiffusion from correlated random walk (114, 117).

Due to the low magnification choice, it was not possible to observer accurately pseudopod dynamics, however we confirm for true vegetative cells in growth medium (HL5) the former conclusions on cell centroid motion: cells exhibit a correlated random walk with a persistence time of a few minutes. To fully observe this long term behavior, it is necessary to fit *MSD* up to about 15 min and to track cells during at least three-fold this period (Fig.3.2). 'Fast' cells (with large *D*) are more persistent than 'slow' cells. However, at short times we have found an interesting non-monotonous behavior in the velocity autocorrelation, with a negative peak at 2 min. This peak which has never been reported in the literature seems related to a tendency for many vegetative cells to retract initially extended pseudopods. Notice that it could be related to the oscillatory component of the velocity detected in Li *et al.* (114) although this oscillatory component was superimposed to a larger amplitude time average component of the velocity.

3.5 Conclusion

This chapter clearly emphasizes that vegetative *Dictyostelium* cells display a classical persistent random motion at long times (*i.e.*, cells are persistent until a cross-over where they recover random diffusion). Extreme care has to be taken to analyze *MSD* curves. Both the total recording time and the number of analyzed cells have to be large enough in order to obtain reliable statistics and reliable estimates of diffusion constant and persistent time. In agreement with numerous studies of *Dictyostelium* cells in a buffer, the diffusion constant appears strongly (positively) correlated with the persistent time indicating that cells modulate their migrated distance possibly by the proportion of persistent runs and not by their intrinsic speed. We demonstrate for the first time in the vegetative state that these quantities are regulated by a quorum sensing factor (QSF) secreted by cells. The molecular structure and the physiological role of this QSF remain to be elucidated but the existence of such a unique relation between cell motility and a QSF concentration and the reported methodology to obtain it (automated multisite cell tracking) offer opportunities to compare quantitatively various mutants and various environmental conditions (surface adhesion, stiffness of the substrate, medium composition).

3. VEGETATIVE CELL MIGRATION

Chapter 4

Cell in the course of development

The social amoeba *Dictyostelium* provides an experimentally accessible and simple model system to investigate chemotaxis and development. When they are starved, cells enter their developmental cycle. They start to signal each other by several quorum sensing factors and cAMP, they aggregate and form a multicellular structure. The evolution of cell motion and shape is analyzed here during the first steps of development (up to 8h of starvation, *i.e.*, streaming and aggregation stages). Cells were collected at different times of starvation t_S from the same high density starved plate $(20 \times 10^6$ cells/mL in DB), plated at different densities and in different buffers under the microscope and analyzed using the same tools than in the previous chapter (automatized timelapse to acquire large data sets, statistical analysis of trajectories). Cell motile properties strongly depend on cell density and starvation time. At early stages $(t_S \leq 2$ h), cells are surprisingly slow and rounded. At late stages $(t_S \geq 3$ h), cells are more elongated and move faster than vegetative cells especially when they are plated at high cell densities. They display anomalous diffusion and seem sometimes attracted towards nascent aggregation centers. However, if cell density under the microscope is reduced or if cell medium is exchanged with fresh buffer, cells become slower and rounded again even at late stages suggesting a dedifferentiation process. The results are discussed in relation with the literature data.

4.1   Introduction

At developmental stages, cell dynamic is mainly governed by cAMP sensed and relayed by the cells. Once starved, cells are becoming aggregative competent: they are more elongated and move faster than vegetative cells, attracted towards aggregation centers emitting waves of cAMP. Only few studies focused on a quantitative and comparative analysis of cell migration in the course of development. These studies often used different strains, substrates and buffers, different starvation conditions. The purpose of this chapter is two-folds. First, assuming that cell-substrate adhesion is regulated in the course of development, a detailed study of cell motility at different developmental stages of *Dictyostelium* is useful to investigate the initial question of this thesis (*i.e.*, how migration is affected by adhesion ?). Second, as exemplified in the previous chapter, cell density may affect cell motility. To our best knowledge, this parameter was never investigated in migration studies in the course of development. However, Gregor and Sawai showed that it greatly affect cAMP production (109). In this introduction, I will present key elements of cAMP signaling and relay, and the state of the art on experimental results on cell shape, speed, traction forces and cAMP production in the course of development.

4.1.1   cAMP signaling and relay

4.1.1.1   cAMP expression, function and regulation

Growth and development are two distinct life cycles for *Dictyostelium* cells. The processes of growth and differentiation therefore need to be coordinately regulated in the early stages of *Dictyostelium* development in the growth-to-differentiation transition (GDT) (84). During exponential growth, *Dictyostelium* cells start synthesizing prestarvation factors (PSFs). PSFs function as quorum-sensing molecules (118). They induce the prestarvation response, which includes expression of genes related to cAMP signaling and developmental aggregation, to prepare cells for early development events before the onset of starvation. When nutrients are depleted, secretion of PSFs is discontinued. At this time, if the cell density is high enough, cells start secreting a diffusible 80 kD glycoprotein called conditioned medium factor (CMF), which induces the expression of early developmental genes and cell-type-specific prespore and prestalk genes (89, 119). As more and more cells secrete CMF, above a threshold, cells start aggregation with relayed pulses of cyclic adenosine monophosphate cAMP.

Most part of *Dictyostelium* development is regulated by cAMP, especially the aggregation stage (Fig. 4.1). In common with other highly motile, chemotactic cells, such as neutrophils,

Dictyostelium sense the chemical gradient through G-protein coupled receptors, in this case the cAMP receptors (or cARs). cAR proteins are evenly dispersed around the cell (120), and GFP FRET (fluorescence resonance energy transfer) analysis demonstrates that G-protein activation occurs with no significant difference from the external cAMP concentration (121).
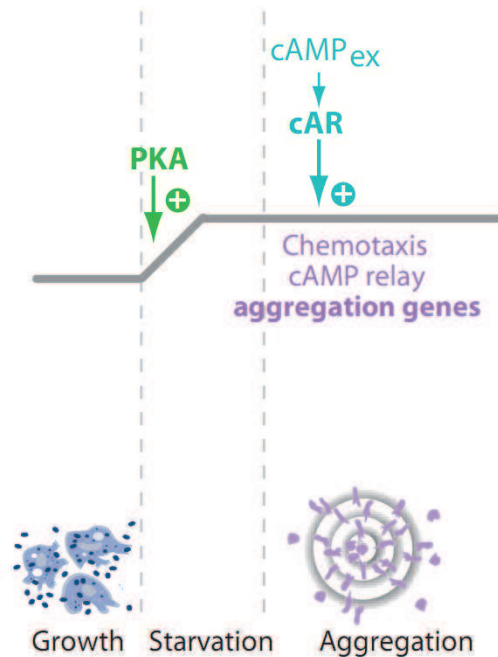
Figure 4.1: **Roles of intracellular and secreted cyclic adenosine monophosphate (cAMP) during *Dictyostelium* development.** The transition from growth to aggregation requires release of protein kinase (PKA) from translational repression. At this stage, PKA triggers a basal level of expression of genes required for aggregation, such as cAR1, PdsA and ACA, which enable the cells to synthesize and secrete cAMP pulses. In addition to inducing chemotaxis and cell aggregation, the cAMP pulses further upregulate the expression of aggregation genes. from (122)

As a secreted signal, cAMP controls cell movement and differentiation throughout the developmental program, but in its more common role as intracellular messenger, it mediates the effect of many other developmental signals. The main intracellular target for cAMP is cAMP-dependent protein kinase or PKA, wich consist of a single regulatory (PKA-R) and a single catalytic subunit (PKA-C). During canonical PKA activation, cAMP binds to PKA-R, which causes PKA-R to dissociate from PKA-C, leaving PKA-C in its active form. However, because PKA-C is active on its own, the ratio of inhibitory PKA-R to active PKA-C molecules is also an important determinant for PKA-C activity (Fig. 4.1). PKA activity is not required for growth, but it is essential for the transition from growth to aggregation (123).

4. CELL IN THE COURSE OF DEVELOPMENT

Once synthesized, PKA-C activates full expression of early genes such as discoidin I, and a basal level of expression of genes that are required for aggregation, such as the cAMP receptor cAR1, the extracellular cAMP phosphodiesterase PdsA, and the adenylate cyclase ACA (86). cAR1, PdsA, ACA and several other proteins, among which PKA and the intracellular cAMP phosphodiesterase RegA, form a biochemical network that can generate cAMP in an oscillatory manner (93). The cAMP pulses are initially secreted stochastically by a few starving cells and elicit three responses: (*i*) cAMP-induced cAMP secretion, also called cAMP relay, which results in propagation of the cAMP pulse throughout the cell population; (*ii*) chemotactic movement of cells towards the cAMP source, resulting in cell aggregation; and (*iii*) upregulation of aggregation genes, causing all cells to become rapidly competent for aggregation.

4.1.1.2 Influence of cell density on cAMP production

Recently Gregor, Sawai and co-workers made a major advance to elucidate the onset of the cAMP oscillations triggering cell aggregation (109). Using fluorescence resonance energy transfer (FRET) based sensor, they were able to directly monitor cytosolic cAMP in live *Dictyostelium* cells. In small cell islands (100-200 cells in a circular spot of $\simeq 400\mu$m in diameter, *i.e.*, $0.5 \sim 1 \times 10^5$ cells/cm^2), cells began to emits cAMP pulses synchronously 5 hours after nutrient deprivation with pulses occurring first sporadically every 15 to 30 min and two hours later periodically every 8 to 6 min. The entire population is participating in the firing from the first pulse (109).

To probe in more details the extracellular conditions necessary to initiate periodic pulses, after 4 to 6 hours starvation in shaken suspensions 2×10^7 cells/mL, cells were plated at different densities in a perfusion chamber and perfused with buffer (no added cAMP) to ensure a uniform and controlled environment. At sufficiently high densities ($\geq 10^5$ cells/cm^2) and under moderate flow speed ($\simeq 1$ mL/min), cells periodically fire approximately once every 6 min on average, which was typically observed in the intact population. With decreasing cell density ($\leq 5 \times 10^4$ cells/cm^2), the synchronized pulses become sporadic and finally cease (109).

These findings indicates that the onset of synchronized pulses occurs by a switch like response of individual cells to an external threshold concentration. The initiation is highly dynamic and collective, and cannot be attributed to a few leaders among the population. As random cells continue to emit pulses sporadically, extracellular cAMP accumulates so that, cells become transiently oscillatory, some local aggregation centers appear and the pulses emitted from such a location become self-sustainable and are periodically emitted.

4.1.2 *Dictyostelium* in the course of Development: Changes in cell velocity, shape and traction forces

4.1.2.1 Cell velocity and cell shapes

The velocity of single *Dictyostelium* (AX3 strain) in the absence of a chemotactic signal has been first analyzed in details during growth, development, and dedifferentiation by Varnum *et al.* (124). These authors demonstrated that the velocity remains low and even significantly decreases for a 6 hours period preceding the onset of aggregation in axenically grown cells ($V = 4.5, 4, 3.8, 3.9\mu$m/min at 0, 2, 4, and 6 hours after starvation respectively). The velocity presents a two-fold increase at 7 hours ($V = 8.4\mu$m/min) corresponding to the onset of aggregation where cells are very elongated and quickly moving in streams during natural aggregation. It then decreases from the formation of loose aggregates (from 8 hours) to very low levels ($V = 3\mu$m/min) at early culminate stage (Fig. 4.2). These authors also demonstrated that if the buffer around cells at 7 hours is exchanged for buffered dextrose solution, the velocity quickly decreases because cells dedifferentiate.

Recent studies using automated tracking protocols characterized not only the speed, but also the full mean squared displacements (MSD) as a function of time (103) and shape changes (pseudopod activity) (116) at several developmental periods. Qualitatively, results differed significantly from the ones of Varnum *et al.* (124) indicating that different starvation conditions might impact the results. Takagi *et al.* measured the MSD of AX2 cells replated on glass at 8×10^3cells/cm^2 after a 0, 1, 2.5, 4 and 5.5 hours starvation period in shaken conditions and with 100 nM pulsed cAMP. MSD displayed always anomalous diffusion. Except at 1 hour where cells exhibited the lowest migrated distance during 15 min, they found that motility and persistence were gradually increasing with starvation time (103). Van Haastert and Bosgraaf *et al.* directly starved AX3 cells in 6-wells at 2×10^4 cells/cm^2 (116). They also observed a gradual increase in migrated distance at 15-min with starvation time. They did not search for anomalous diffusion behavior but their important contribution was to develop a computer algorithm that identifies the size, timing and direction of extending pseudopodia. In particular, they found that cells either extend front splitting pseudopodia at a small angle and preferentially alternating to the right and left (zig-zag step), or at random directions (turn). On average, vegetative cells extend 1.8 zig-zag steps and 1.6 turns per minute, giving a total pseudopod frequency of 3.4/min. Cells starved for 5 hours do not extend many more pseudopodia (3.9/min), but extend much more zig-zag steps (3.4/min) relative to turns (0.5/min). The increase of

the step/turn ratio in starved cells strongly influences the length of the nearly straight runs (*i.e.*, persistence). Finally, the size of extended pseudopods ($\simeq 5\mu$m) does not change between vegetative and starved cells arguing that cAMP controls cell polarization rather than direct induction of actin polymerization (125).
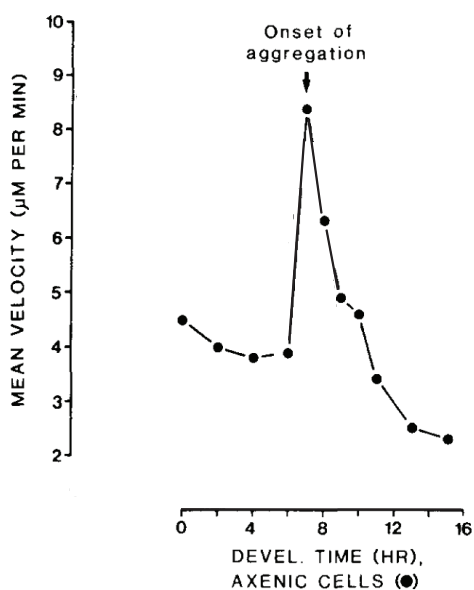
Figure 4.2: Mean velocities during development. Exponentially multiplying cells were washed free of axenic medium and dispersed on parallel development filters. At the noted times, cells were disaggregated and tested for motility. Each data point represents the mean velocity for at least 15 independently monitored amoeba. The ripple (R), loose aggregate (LA), tight aggregate (TA), finger (F), and early culminate (ECl) stages occurred at 7, 8, 11, 13 and 14 hr, respectively, for axenically grown cells. from (51)

4.1.2.2 Traction forces

The distribution of forces exerted by migrating *Dictyostelium* amoebae at different developmental stages was measured by Delanoë-Ayari *et al.* (28) using traction force microscopy. They have found remarkable differences in cell shape, speed, as well as in traction force magnitude and force distribution in three different phases of the unicellular stage of AX2 *Dictyostelium* cells.

In the vegetative state (HL5 medium), cells present cyclic changes in term of speed and shape between an elongated form and a more rounded one (Fig. 4.3). The forces are larger in
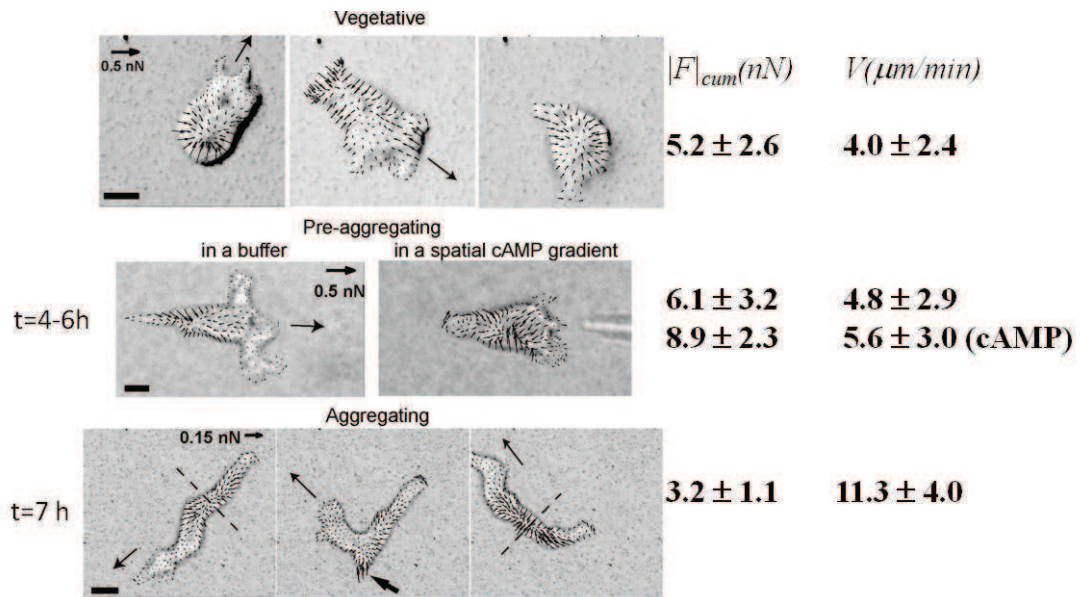
Figure 4.3: Force exerted by AX2 cells in the course of Development. Traction forces have been evaluated for vegetative, pre-aggregating and aggregating *Dictyostelium* cells in DB on very soft polyacrylamide elastomer substrates ($E \sim 400$ Pa).Bars, 5μm. From reference (28).

this first state, especially when they are symmetrically distributed at the front and rear edge of the cell (see also Fig. 1.11). Elongated vegetative cells can also present a front-rear asymmetric force distribution with the largest forces in the crescent-shaped rear of the cell (uropod). Pre-aggregating cells (DB buffer), once polarized, only present this last kind of asymmetric distribution with the largest forces in the uropod. Neither the force distribution of pre-aggregating cells ($t = [4 - 6]$h) nor their overall magnitude are modified during chemotaxis, the later being similar to the one of vegetative cells ($F_0 \sim 6$nN). On the contrary, both the force distribution and overall magnitude is modified for the fast moving aggregating cells ($t = 7$h).

An inverse relationship between average speed and average force is found. The aggregating cells are twice faster but exert almost twice less force than the pre-aggregating or vegetative cells (28).

4.2   Results

The protocol and statistical methods used to study cell migration in the course of development are described in Chapter 2.

4.2.1 Cell migration during development

We have analyzed the migration of starved *Dictyostelium* cells at different stages of their development. Cells were collected at different starvation times at 20×10^6 cells/mL in development buffer (DB). They were plated under the microscope at constant effective cell density of 1500 cells/cm^2 in DB, recorded and tracked during 50 min in a stagnant buffer where cAMP concentration is likely to increase in the course of development. Surprisingly, freshly starved cells in DB are very slow.
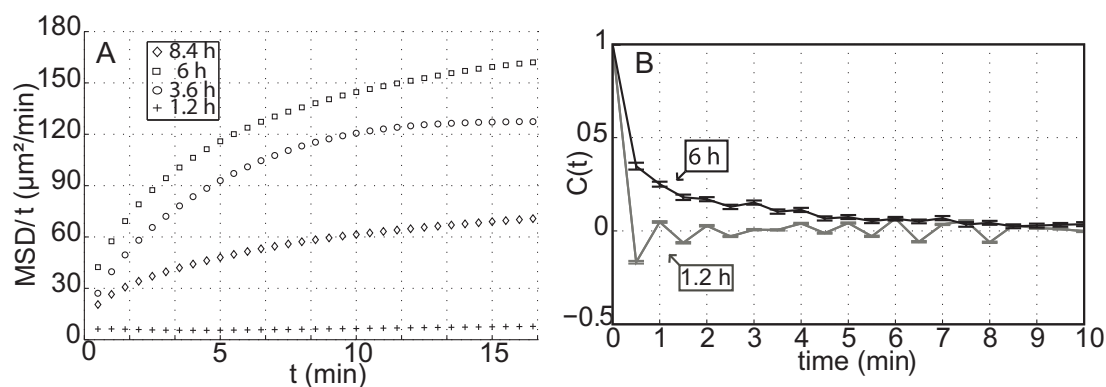
Figure 4.4: **(A)** MSD/t as a function of time lag t in the course of development at 1500 cells/cm^2 in stagnant buffer. MSD is calculated from 50 min trajectories every 2.4 hours. The slope at long time does not always reach 0 due to chemotaxis. An apparent diffusion constant D^* is evaluated from the MSD at 15 min. The highest D^* is reached after 6 hours of starvation. **(B)** Velocity autocorrelation $C(t)$ as a function of time lag for the same cell conditions as **(A)** after 1.2 hours of starvation and 6 hours of starvation, respectively. Error bars represent SEM.

Their migration recovers normal diffusion after a time lag of about 1 minute with a mean diffusion constant much slower than the one found in fresh nutrient medium ($D = 1.5 \mu$m^2/min *Vs.* $D = 11,2 \mu$m^2/min for DB and fresh nutrient medium, respectively). This slow behavior is also found in the velocity autocorrelation curve (Fig. 4.4B) which exhibits a negative peak more important that in nutrient medium. These freshly starved cells appear to frequently retract newly extended pseudopods and as a result are little migrating. As starvation time increases, cells gradually increase their speed (migrated distance at a given time) and become more persistent. The cells are faster at 6 hours which corresponds probably to the onset of aggregation (124). At this time, anomalous diffusion is found (*i.e.*, $MSDs$ scale as t^β with an exponent $\beta = 1.2$ even after hours) (Fig. 4.4A). Meantime, the velocity autocorrelation (Fig. 4.4B) shows a very slow decay time ($t_d \geq 5$ min by fitting this part of the curve with an

exponential function). In that case, we believe that anomalous diffusion is due to chemotaxis as we could detect the initiation of some aggregation centers. For larger times (*i.e.*, 8.4 hours), cell speed decreases dramatically as previously found (124).
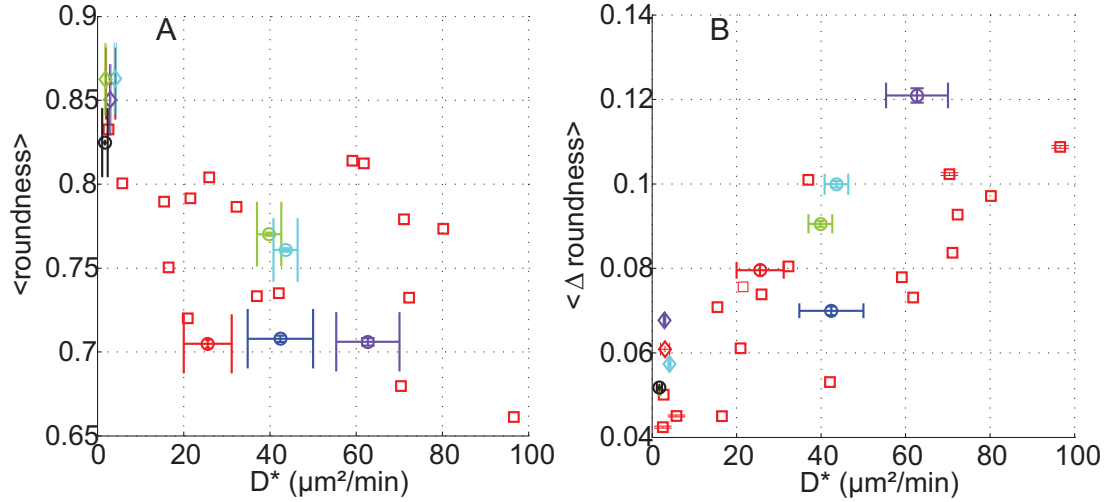
Figure 4.5: Cell shape is correlated with apparent diffusion constant D^* (**A**) Mean cell roundness is negatively correlated with the diffusion constant.Roundness is defined as $2(\sqrt{A/\pi})/M$ where A is the cell area and M the cell major axis length (both are determined with Matlab). The more elongated the cells are (Roundness< 1) the faster they move. (**B**) mean roundness variation (absolute value) between 2 successive steps is positively correlated with D^*. All variables are plotted as a function of D^* which is obtained by *MSD* at 15 min interval. Circles represents the data from Fig. 4.7A and Fig. 4.11B after $5 \sim 6$ hours of starvation. Diamonds represents the data from Fig. 4.7A after 1 hour of starvation. For both, color code represents cell density (red: 400, green: 1500, blue: 2000, cyan: 4000, violet: 6000 cells/cm^2 and black: 2000 cells/cm^2 with buffer renewal). Error bars represents SEM.

We use the roundness parameter to quantify cell polarization. Cell roundness (quantifying cell polarity) is inversely correlated with D^*, while roundness variation (quantifying cell deformation activity) is correlated with D^* (Fig. 4.5): the more the cells is elongated and the more it actively deforms, the larger is the diffusion constant.

As in the vegetative phase, we observe a correlation between apparent diffusion constant and cell persistence parameters calculated with the bimodal analysis (Fig. 4.6): the faster the cells are, the longer is the time spent in persistence mode (t_P) and the longer are the persistence lengths (L_P). The faster the cells are, the less they change their direction of movement between two successive steps.
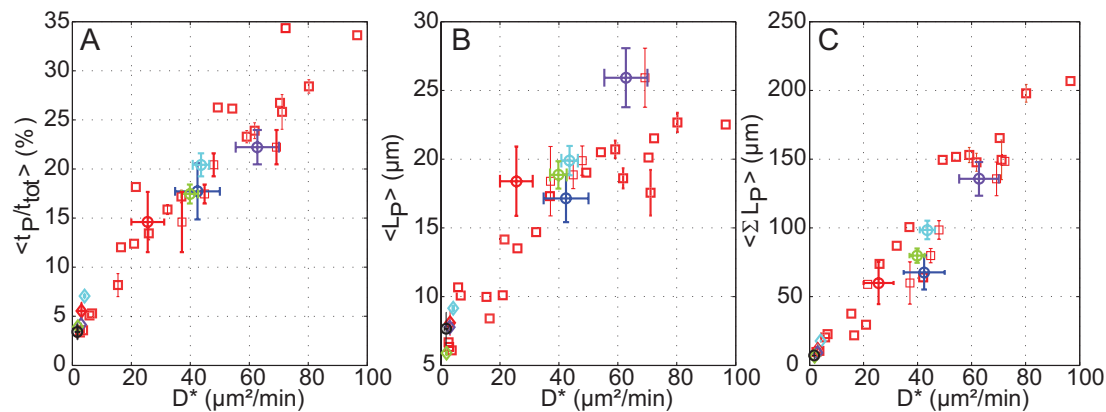
Figure 4.6: Cell persistence is correlated with apparent diffusion constant D^*. Average parameters obtained from a bimodal analysis for the whole experiments with starved cells: **(A)** Ratio of time spent in persistent mode over total tracking time. **(B)** Length of persistence L_P (distance end-to-end of each individual persistent portion of cell trajectory). **(C)** $\sum L_P$ is the cumulated distance in the persistent mode. $\langle \rangle$ denotes averaging over all tracked cells in a given condition in a single experiment. All variables are plotted as a function of apparent D^* which is obtained by *MSD* at 15 min interval. Circles represents the data from Fig. 4.7A and Fig. 4.11B after $5 \sim 6$ hours of starvation. Diamonds represents the data from Fig. 4.7A after 1 hour of starvation. For both, color code represents cell density (red: 400, green: 1500, blue: 2000, cyan: 4000, violet: 6000 cells/cm^2 and black: 2000 cells/cm^2 with buffer renewal). Error bars represents SEM.

4.2.2 Effect of cell density during development

Using the device described in 2.1.3 we can study the effect of effective cell density on cell migration during starvation. We quantified this effect in the course of development by repeating the previous experiment (MSD at different starvation times) for effective cell densities ranging from 400 to 6000 cells/cm^2 (corresponding to cell-cell distances of 500 to 130 μm, respectively).

The apparent diffusion constant (D^*, migrated distance after 15 min divided by 4×15 min) as already described, depends greatly on the starvation time but also on the effective density (Fig. 4.7A). For each effective cell-density investigated, maximal apparent diffusion constant (onset of aggregation) always occurred 6 hour after starvation. However, strong differences in the amplitude of apparent diffusion constant are found: the denser the cells are, the faster they move (from 25 μm^2/min to 62 μm^2/min at 400 cells/cm^2 and 6000 cells/cm^2 respectively).

Cells after 1 and 6 hours of starvation described in Fig. 4.7A are represented in Fig. 4.5 and 4.6 by diamonds and circles, respectively using the same color code to identify cell den-
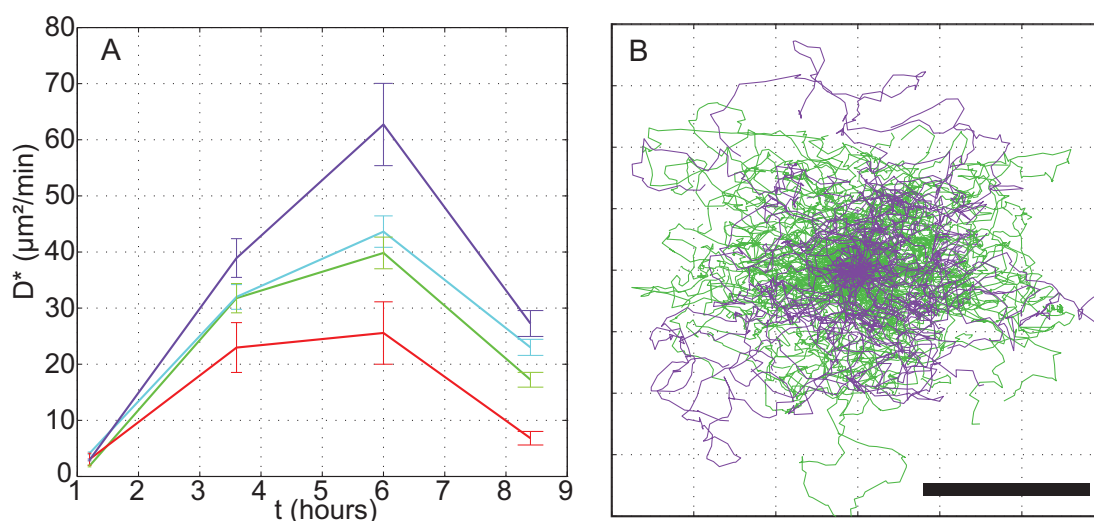
Figure 4.7: **Apparent cell diffusion constant as a function of starvation time and effective cell density during development in stagnant buffer.** (**A**) Each line represent a different cell density: (red line) 400 cells/cm^2, (green line) 1500 cells/cm^2, (cyan line) 4000 cells/cm^2, (violet line) 6000 cells/cm^2. D^* is dependent of cell density. (**A-B**) Cells are tracked in DB over 50 minutes every 2.4 hours. Error bars represent SEM. (**B**) Cell trajectories in DB after 6 hours of starvation at two different densities: (green line) 1500 cells/cm^2, (violet line) 6000 cells/cm^2. The more developed (larger) trajectories appear similar but the experiment at the lowest density present more cells with little migrated distances. 50 cells tracks in DB during 50 minutes. Scale bar: 100 μm.

sity. There is a clear increase in all persistence parameters and in the absolute roundness and roundness variation, due to the cell density. At the onset of aggregation ($\sim$ 6 hours of starvation), cells are more polarized, more active and more persistent than during the first hour of starvation. These features correspond to the typical phenotype of aggregation competent cells.

Cell trajectories after 6 hours of starvation for cells at 1500 cells/cm^2 and 6000 cells/cm^2 are represented in Fig. 4.7B. Despite a 1.5 fold difference in the average apparent diffusion constant D^*, the area covered by the more developed cell trajectories are identical. Some cells are able to move as fast even if the condition are not optimal (*i.e.* low density). Therefore, this difference observed on D^* cannot be explained by a global increase in motility but rather by a ratio of slow/fast moving cells which decreases when density increases.

4.2.3 Evidence of heterogeneous cell population

Figure 4.8 shows a zoomed view of two migrating cells in the same experimental dish, at x4 magnification in DB after 5 hours of starvation at 200.10^6 cells/mL. Despite the low magni-
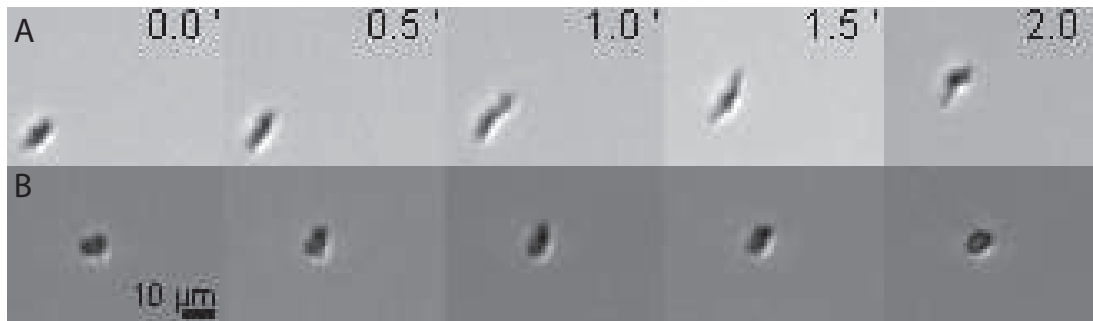
Figure 4.8: Zoomed view of an aggregation competent cell (**A**) and a non-aggregation competent cell (**B**). One can easily notice two different phenotypes. Both cells have been observed in the same experimental dish.

fication we can easily distinguished two phenotypes based on the *Dictyostelium* shape: the elongated cell is an aggregation competent cell and the round one is probably not.

After 6 hours of starvation distribution of cell deformation as a function of density (Fig. 4.9) confirms the idea that under starvation there are two subpopulation of cells: the one actively changing their shape and the other less.

This is also confirmed by the analysis of the distribution of percentage of time spent in persistence mode of individual cells (Fig. 4.10). Three very different experimental conditions leading to different apparent diffusion constants are examined: high, intermediate and very low apparent diffusion constant (corresponding respectively to an experiment at high cell density (6000 cells/cm^2) in stagnant buffer, at a low cell density (400 cells/cm^2) in stagnant buffer, and at an intermediate cell density (2000 cells/cm^2 with buffer renewal impairing cAMP signaling). Most of the very slow cells (black bars) spend less than 10% of their time in the persistent. They are random. On the other hand, the whole very fast cells (violet bars) are persistent more than 10% of their time. In case of cells with intermediate apparent diffusion constant, the time spent in persistence mode is widely distributed: some cells are very random, some cells are very persistent. This is a supplementary evidence that the decrease in average motility for the cell population is rather a shift in the proportion of slow/fast subpopulation of cells. Considering that most cells were differentiated when we take few mL from the mother petri dish, it is tempting to conclude that we observe dedifferentiation if we reduce cAMP production by decreasing cell density.

In order to directly check this hypothesis, we measured in parallel the migration of cells in stagnant buffer and after buffer renewal at constant cell density. Fig. 4.11 shows a stricking effect of medium renewal on cell motility. Cells clearly explore less their environment when
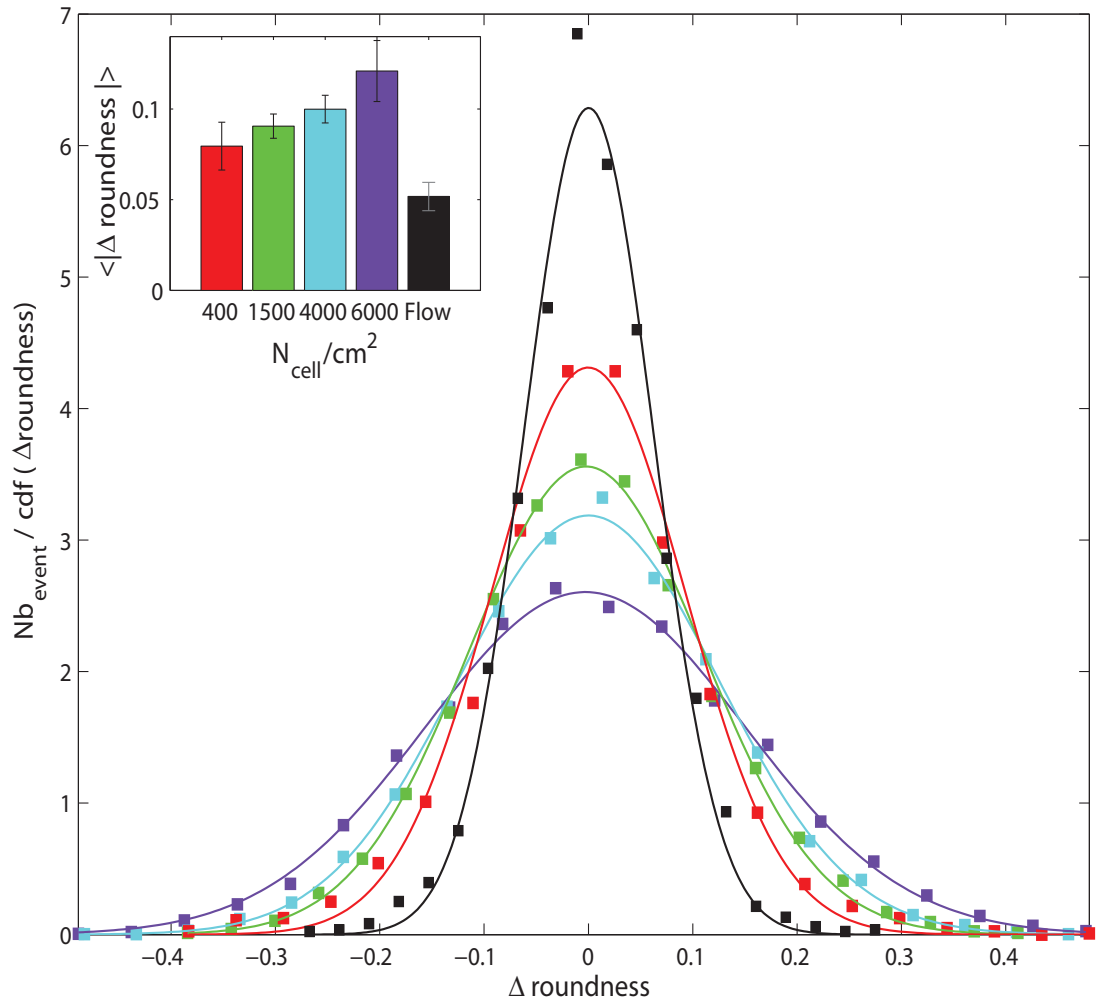
Figure 4.9: Cell deformation distribution. Normalized distribution of roundness variation $< \Delta roundness >$ for cells after 6 hours of starvation as a function of cell density (squares). As the density increases the ratio of highly deformable cells ($|\langle \Delta\ roundness \rangle| \geq 0.2$) increases. In accordance, the ratio of less active cells ($\langle \Delta\ roundness \rangle \sim 0$) decreases. Line are centered normalized Gaussian fit. Colors represents different density (given in the inset, black: 2000 cells/cm^2 with buffer renewal). The area under curve is normalized to 1. Inset: mean value of cell deformation increases with cell density.

cAMP is washed away at 5 hours starvation (Fig. 4.11A) and are far less motile for all starvation times (Fig. 4.11B). As it takes a 50-min period to measure the apparent diffusion constant and as we waited a little that cells recover from the change of medium, we can conclude that dedifferentiation takes less than 1 hour.
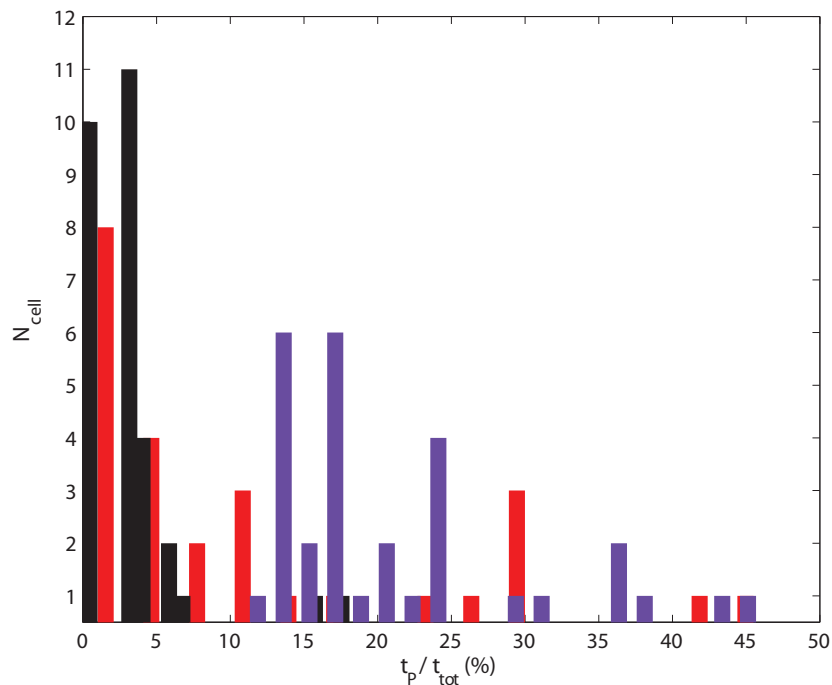
Figure 4.10: Histogram of cell persistence. Percentage of time spent in persistent mode after 6 hours of starvation deduce from a bimodal analysis of more than 30 cells for each conditions. (red bars) 400 cells/cm^2 in a stagnant buffer; (violet bars) 6000 cells/cm^2 in a stagnant buffer; (black bars) cell under buffer renewal at 2000 cells/cm^2. The proportion of highly persistent cells increase with the density.

4.3 Discussion

The results about the motile properties of starved cells found in this chapter are in many ways complementary than the ones found in the literature.

In the literature, all *Dictyostelium* migration experiments were performed with starved cells in a phosphate (PB) or development buffer (DB). In our case freshly starved cells present a surprisingly low diffusion constant of 1.5 μ^2/min, and a negative peak in the autocorrelation function. Varnum *et al.* found very low speed during the first hours of starvation (124). Takagi *et al.* obtained also smaller MSDs for 1h-starved cells than vegetative cells. But the results of these different studies are difficult to compare quantitatively because of different experimental conditions. The population is also probably very heterogeneous with a majority of very slow cells yet undifferentiated and a few very active early differentiated cells. Some cells may indeed quickly enter in a development stage (presumably the ones that are close to the
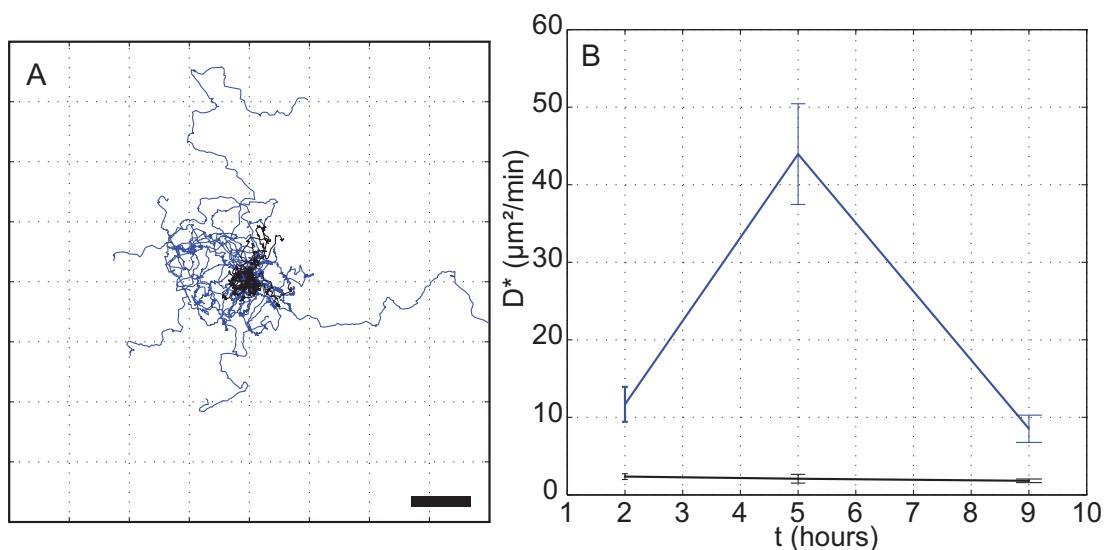
Figure 4.11: Effect of cAMP removal on cell migration. (**A**) Typical cell trajectories when cells were transferred under the microscope after 5 hours starvation in DB (5 hours at 20×10^6 cells/mL in DB). (**B**) apparent diffusion constant D^* as a function of starvation time. Blue line corresponds to migration in stagnant buffer (where cAMP is produced and degraded by cells), black line corresponds to buffer renewal (cAMP is removed). All experiments presented here were conducted at 2000 cells/cm² under the microscope. Less developed trajectories and lower apparent diffusion constant under buffer renewal indicate that cells quickly dedifferentiated and lost their aggregation competence in the absence of cAMP. Scale bar: 100 μm.

growth/differentiation checkpoint (GDT point) in their life cycle (84)).

For longer starvation time, cells acquire progressively aggregation competence by exchanging signals, becoming very polarized and very motile (95). Anomalous super-diffusion process reported in that stage ($< \rho^2 \simeq t^\beta$ with *beta* > 1) seems to be related to development, with increase of both persistence time and velocity (103, 105). However, as explained in the previous chapter, to be sure to reach the normal diffusion regime (*i.e.* plateau of the *MST*/t curves), it is necessary to track trajectories during 8-10 times the expected persistence time. In this work, we believe we investigated long enough times to conclude that in average diffusion is anomalous. However, this average behavior may be greatly influenced by a few very ballistic cells attracted by nascent aggregation centers while most of the cells are still random at long times especially the slow ones not fully differentiated or dedifferentiated. This point will be interesting to be clarified in the next future.

Complementary studies analyzing cell migration at the onset of aggregation (5h starved

cells at a density of 2×10^7 cells/mL, with exogenous pulses of 75 nM cAMP every 6 minutes) and tracked at high cell density (cell-cell distance of $40 \sim 100 \ \mu$m) have also confirmed the anomalous behavior, with an exponent β stabilized around 1.5 in the presence of cAMP gradients (generated by other streaming cells, or delivered via a micropipette (111)). This group analyzed independently the role of signal relay and developmental stage in the speed and directional persistence of aggregation-competent cells using *aca-* mutant cells (*aca-* cells are able to sense and respond to the presence of exogeneous cAMP, but cannot secrete it). *aca-* cells in uniform cAMP concentration exhibit anomalous superdiffusion in the first 3 minutes ($\beta \simeq 1.5$, corresponding to the formation of pseudopods in the vicinity of former ones), but normal diffusion is recovered after 10 minutes ($\beta \simeq 1$), indicating that direction of pseudopods formation is lost. They found no differences in this behavior when comparing cells at different developmental stage (5h and 6.5 h). This study confirms that the direction of pseudopod formation is regulated by signal relay rather than developmental stage. The timescale is similar to the one found in this thesis, with a decrease of the exponent β after 10-12 minutes. Gregor and Sawai showed by FRET that decreasing cell-cell distance below $50 \ \mu m$, the synchronized cAMP pulses emitted by starved cells (4-6 hours) become sporadic and finally cease (109). By analyzing cell migration and shape at larger cell-cell distance (ranging from 130 to 500 μm), our study complement this analysis and revealed that even if cells are unable to form streams at this cell density (a minimum cell-cell distance of 100 μm is required for stream formation (111)), cell shape and motility strongly depend on cell-cell distance, and hence on cell-cell signaling. We do not know at this stage if this signaling is due to cAMP signal relay, or if the effect is a quorum sensing phenomena (that could be regulated by CMF).

The importance of signaling is also confirmed by the perfusion experiments. Upon perfusion (impairing any signaling between cells), cells reset their differentiation state within less than 1 hour. This is in agreement with the measured drop in velocity of Varnum *et al.* after changing the medium of 7-hours developing cells (124). For cells replated at intermediate densities (1500 to 4000 cells/cm^2 in Fig. 4.7), distribution of time spent in persistence mode, together with distribution of cell shape variation evidenced the existence of at least two subpopulations of cells: (*i*) fast cells, moving very often in persistent mode and changing their shape very dynamically, (*ii*) slow cells, moving more often in random mode and with moderate change in their shape. Note that the transition between this two extreme cases is not sharp and there is rather a continuum of cells evolving toward the fast mode. This could be due to the low sensibility of our current experiments (spatio-temporal resolution could be greatly improved by

dedicated experiments) or could have again a biological origin (existence of a large variability in cell properties). It is indeed well known that the more they were differentiated, the longer it takes for cells to dedifferentiate (84). In any cases, the fast/slow cell mode denomination is a way to easily and clearly described the existence of different subpopulations of cells, one fully differentiated and aggregation competent, one dedifferentiated.

_____

4. CELL IN THE COURSE OF DEVELOPMENT

Chapter 5

Cell under hydrodynamic shear stress

We have developed a method for studying cellular adhesion by using a custom-designed microfluidic device with parallel non-connected tapered channels. The design enables investigation of cellular responses to a large range of shear stress (ratio of 25) with a single input flow-rate. For each shear stress, a large number of cells is analyzed (500-1500 cells), providing statistically relevant data within a single experiment. Besides adhesion strength measurements, the microsystem presented in this paper enables in-depth analysis of cell detachment kinetics by real-time videomicroscopy. It offers the possibility to analyze adhesion-associated processes, like migration or cell shape change, within the same experiment. We examined quantitatively cell adhesion by analyzing kinetics, adhesive strength and migration behavior or cell shape modifications. We find that the threshold stresses, which are necessary to detach the cells, follow lognormal distributions, and that the detachment process follows first order kinetics. In the vegetative state, for glass substrate, cells are found to exhibit similar half-adhesion threshold stresses ($\sigma_{1/2}$, stress necessary to detach half of the cell) in fresh HL5 and Conditionned Medium (CM defined in chapter 3), but very different detachment kinetics (cells detach faster in CM than in HL5), revealing the importance of dynamics analysis to fully describe cell adhesion. Cell adhesion is found to decrease in the course of development, with a half-adhesion threshold stress two fold lower for 6-h starved cells compared to vegetative cells.

5. CELL UNDER HYDRODYNAMIC SHEAR STRESS

5.1 Introduction

Cell adhesion is a key process in many physiological and pathological situations. It is essential for many important cellular processes, such as tissue organization and differentiation, embryonic development and, as we have seen in the previous chapter, cell migration. Cell adhesion is known to trigger cell growth (126) and cell migration (127). During tumor progression, cancer cells are able to tune their adhesion in order to escape from primary tumor site and colonize other organs (128). Many cells are also sensitive to external forces, in a process generally called mechanotransduction (129). In blood circulation, shear stress is the most common mechanical stimulation sensed and transduced by the cells. Shear stress has been shown to influence adhesion of immune system cells (*e.g.* leukocytes (130) and neutrophils (131)), and gene expression in endothelial cell (132, 133), which alters adhesion on vessel walls of metastasizing cancer cells (134). Cell adhesion has been thoroughly investigated for mammalian cells, and many proteins and signaling pathways are known (135). On the other hand, mechanical aspects of cell adhesion are still under intensive theoretical and experimental considerations (136). Cell adhesion strength is usually estimated using controllable external forces that enable gradual cell detachment (137). This can be performed using centrifugal forces (18, 138, 139), or other macroscale set-ups such as radial flow-chambers (140), spinning disks (141) and rectangular parallel-plate flow chambers (142, 143). More recently, microfluidic-based adhesion chambers have been developed with tunable ranges of applied hydrodynamic forces, enabling real-time analysis of cell detachment kinetics (144, 145, 146), including cancer cell experiments (147, 148). Microfluidic dimensions require only small amounts of cells and reagents, and allow laminar flow, high throughput and the possibility of parallelization. Most of these devices, however, have a rather biological approach and therefore are satisfied with yielding the same results that could be achieved similarly by macroscopic approaches, that is counting the fraction of cells that detaches when exposed to a specific shear stress (137). Little effort has been made so far to resolve the time dependence of this fraction, *i.e* the detachment kinetics, which have been the object of mathematical and numerical modeling in several biophysical papers (149, 150, 151, 152).

We aim at filling that gap with a simple microfluidic device consisting of four independent channels enabling investigation of cell detachment in a large shear stress range (more than 1 order of magnitude), with a single input flow rate. Microfluidic set-ups enable time-lapse investigation not only on detachment kinetics, but also on cell motion under shear stress. We

show how this can be used to enhance the understanding of cell adhesion. Both kinetics of cell detachment and cell motion are investigated using *Dictyostelium* . Thanks to the versatility of the microfluidic-device presented in this work, it is possible to get results on adhesion strength for different cell types (MDA-MB-231 breast cancer cells were also tested with the device) with only minor experimental modifications. First results regarding cell adhesion for *Dictyostelium* in the vegetative state are presented and compared with cell adhesion in the course of development.

5.1.1   State of the art: cell adhesion experiments
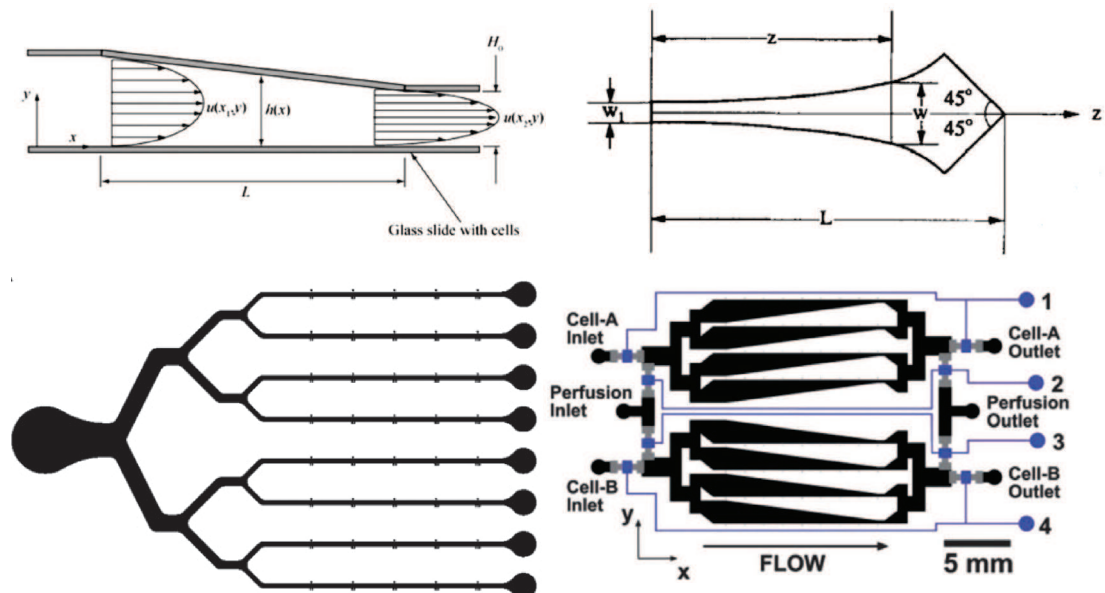
Figure 5.1:   Macrofluidic and microfluidic devices. (A) Variable-height flow chamber (21). (B) Variable-width linear shear stress flow chamber ((153)) (C) Eight-channel parallel microfluidic network for Endothelial cells adhesion assays. (D) Parallel microfluidic networks with variable shear flow chambers (146). From (137).

Classical cell culture flow systems designed to study adhesion often easily allow cell counting under different shear stresses and at different timepoints, but may require substantial modifications to allow proper visualization via microscopy to permit accurate predictions of individual cell-to-surface bond strengths. Parallel plate flow chambers are also the most commonly used apparatus for endothelial cells shear stress response studies. In adhesion assays, cells are loaded into the flow chamber, allowed to adhere, and then applied shear stress is incrementally

increased to produce a ramped shearing protocol. Because flow chamber geometry is uniform throughout the device and samples of adhered cells are treated with the same conditions for a given experiment, these chambers are limited to studying a single experimental condition at once. Parallel plate flow chambers have been modified to allow the same flow rate to simultaneously generate different shears at different locations. Variable-height flow chambers rely on a sloped top plate such that shear stress varies as a function of height, h(x), along the x-direction of the bottom plate (Fig. 5.1A). The variable-width flow chamber designed by Usami *et al.* (153) employs a tapered channel where side walls follow an inverse function, thus producing a linear shear stress gradient from inlet to outlet (Fig. 5.1B). Both systems permit simultaneous application of a range of shear stresses, but the tapered channel is easier to fabricate because of the uniform height, and thus lends itself well to microfabrication techniques.

Alternatively, one can take advantage of radial and circumferential flows to create ranges of shear stress from the non-uniform velocity fields. Radial flow can be generated by either divergence from a single point source, or convergence to a sink. If flow is confined by parallel plates, velocity and shear stress are both dependent on radial position alone. Circumferential flows may also be developed to generate similar shear stress gradients in the radial position. These fluid flow principles have been implemented for cell adhesion studies in a myriad of designs, including radial flow chambers (140), and spinning disc apparatuses. Although variable shear stress devices can produce a range of shear rates using a single volumetric flow rate, all these systems suffer from the major drawback that only one combination of cell type and specific surface can be tested at one time. Many bioengineering studies involve investigating multiple cell types on different surface functionalizations to screen for appropriate biomaterials and surface coatings that provide optimal adhesion of a given cell type. Yet none of these macroscale devices can determine adhesion strength metrics (*e.g.*, critical wall shear stress) for multiple cell and surface conditions at once. Recent developments in microfluidics have demonstrated that such capabilities are indeed possible. Examples of microfluidic devices for adhesion studies are plentiful. Kantak *et al.* (154) were one of the first to take advantage of parallelization in microfluidics and the convenience of soft lithography by investigating platelet adhesion to different fibrinogen-coated substrates on four individual straight microchannels on the same chip. By applying different surface coatings in each, Kantak and co-workers demonstrated one of the most basic advantages of microfluidics, *i.e.*, increased efficiency of experimentation by parallelizing multiple conditions. Keeping the microchannels separate ensured no cross-contamination between samples. Young *et al.* (144) adopted a similar configuration with eight

parallel interconnected microchannels, and used it to reveal differences in adhesion properties of vascular and valvular Endothelial cells (Fig. 5.1C). Flow analyses in these types of networks relied on principles of hydraulic resistance. While these designs reduced the number of connections, they introduced the possibility of cross contamination between connecting branches of the network. Despite these designs have benefited from parallelization, shear stress must be manually adjusted by changing flow rate in the system. By varying the length over width ratio in interconnected channels with similar pressure drop, it is nevertheless possible to submit cells simultaneously to different shear stress, with a single input flow rate (145). Alternatively Gutierrez and Groisman designed a microfluidic device (Fig. 5.1D that incorporated variable shear stress flow chambers in a parallel configuration, combining the efficiency of multiple shear rates within one chamber with the flexibility of multiple experimental conditions across separate chambers of the same device (146). We tested such approaches, but a general problem with complex interconnected channel systems is, that a defect in one of the channels changes all hydrodynamical resistances and impairs the local flow rate estimates. Parallel channel systems bring along also other disadvantages, such as difficulties to dispose of air bubbles or problems with seeding the cells uniformly in the parallel branches. All these drawbacks could be avoided or downsized by our device which uses simple tapered channels without interconnections, corners and acute angles, as shown in Fig. 2.7. Based on this design,we have developed a microfluidic device to quantify cell adhesion as well as cell detachment kinetics that answer the drawbacks of macroscale device and allow parallelization of four different condition. (155).

5.2 Results and discussion

5.2.1 Device design and rationale

Tapered shapes of the channels enable the exploration of a wide range of shear stresses along the channel direction x. Our tapered device which is shown in Fig. 2.7 is characterized by a linearly decreasing width w given as $w(x) = w_{min} + \frac{x}{L}(w_{max} - w_{min})$ ($w_{max} = 5$ mm and $w_{min} = 200\mu$m, channel length $L = 36$ mm). As the tapering slope is small ($dw/dx \approx 0.13$), the classic wall shear stress expression (137) (at the bottom of the channel where the cells adhere) for a rectangular tube of width $w \gg h$ (h is the channel height) can be locally applied:

$$\sigma(w(x)) = \eta \frac{dv}{dz}\bigg|_{z=0} = \frac{6\eta Q}{h^2 w(x)} \tag{5.1}$$

where η is the viscosity and Q the flow rate. In our case, $w \gg h$ is not fulfilled for all channel positions, and a 3D analysis of the velocity field is necessary (the calculus is given in appendix C. Master thesis of Peter Rupprecht.)

In a single experiment, the maximal range of shear stress is given by the ratio $\sigma_{max}/\sigma_{min} = w_{min}/w_{max} = 25$. This is large compared to microfluidic devices of similar design, for instance $\sigma_{max}/\sigma_{min} = 8$ in (146).

With h varying between 50, 100 and 150 μm, and Q up to 50 mL/h, wall shear stresses up to 100 Pa can be realized; however, the device is designed to work best at $0.1 - 5$ Pa, which covers the physiological range (137). To increase the shear stress range for one experiment, different flows can be applied for parallel channels by using syringes with different inner diameter.

The large dimensions lead us to revisit microfluidic assumptions, notably laminarity. The Reynolds number can be calculated using the average flow velocity $U = Q/(wh)$ and the hydraulic equivalent diameter for rectangular channels $D_h = 2hw/(w+h)$:

$$Re = \rho U D_h / \eta = \rho 2Q/(\eta(w+h)) \tag{5.2}$$

Laminar flow can be assumed for $Re < 2000$ (156). For this work, we have $Re < 5$, thus indicating laminar flow. The use of large glass slides (52x76 mm) enables to have 4 independent tapered channels in parallel. This offers the possibility of exploring different cell types and/or environmental conditions (coating, medium) in a single experiment. This can be pivotal for cell biology experiments where results from different conditions should be compared as much as possible from the same experimental day.

After cell injection and scanning path selection of the motorized stage (Fig. 2.7B), the experiment starts when both the syringe pump infusing at a constant flow rate Q and timelapse videomicroscopy are switched on ($t = 0$). The image treatment described in the protocol chapter (chapter 2) results in the typical cell detachment curves displayed in Fig. 5.2. Each curve represents the proportion of detached cells as a function of time for a given position along the channel. The initial cell number decreases exponentially, before reaching an asymptotic regime where almost no cell detachment is detectable. Due to limited recording time, the asymptotic regime is not fully reached for *Dictyostelium* in fresh medium (Fig. 5.2A) at low stress ranges, but can be observed in highly conditioned medium (HCM) (Fig. 5.2A, green open circles). The meaning of these asymptotic states will be discussed later on in the framework of a threshold stress model. For each experiment, channel height and/or flow rate are adjusted in order to
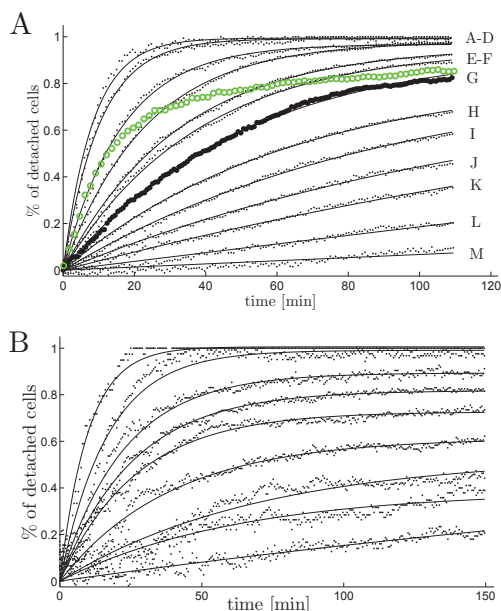
Figure 5.2: Detachment curves with first order kinetic fits. **A.** Cell detachment curves for *D. Discoideum* DH1 in fresh medium, fitted with first order kinetics. The letters on the right show the channel position (cf. Fig. 2.7) which is used for the corresponding detachment curve. Higher shear stresses correspond to greater detachment. The detachment curve for 0.50 Pa (letter G) is highlighted by larger dots, the detachment curve for DH1 in highly conditioned medium (HCM) at the same shear stress is drawn in green open circles. This shows that the final detachment is very similar for both conditions, whereas the kinetics are much faster for HCM. **B.** Detachment curves for MDA-MB-231 human breast cancer cells. The more significant fluctuations are due to a lower cell concentration and image treatment.

cover the whole range of detachment from complete detachment up to almost zero detachment (100 μm and 5 mL/h for *Dictyostelium* cells.

5.2.2 Mathematical description of adhesion and detachment

For describing the adhesive behavior of these two cell lines, we mostly follow (140); similar ideas were also used by (148). Three major assumptions are made: (1) There is a threshold shear stress σ_t for each cell, which, if exceeded, leads sooner or later to the detachment of the respective cell. (2) This threshold stress is lognormally distributed over a given population. (3) The detachment dynamics follow first order kinetics.

The lognormal threshold stress distribution $f(\sigma_t)$ is specified by its median $\sigma_{1/2}$ (the stress at which half the cell population detaches) and the dimensionless distribution width $\widetilde{\sigma}$:

$$f(\sigma_t) = \frac{1}{\sqrt{2\pi}\widetilde{\sigma}\sigma_t} \exp\left(-\frac{\ln^2(\sigma_t/\sigma_{1/2})}{2\widetilde{\sigma}^2}\right) \tag{5.3}$$

The cumulative distribution (*i.e.* the integral of $f(\sigma_t)$) gives the proportion of cells which will be detached by a given stress σ; we call this proportion the detachment efficiency $e(\sigma)$,

$$
\begin{aligned}
e(\sigma) &= \int_0^\sigma f(\sigma_t)d\sigma_t = \\
&= \frac{1}{2}\left[1 + \mathrm{Erf}\left(\frac{\ln\left(\sigma/\sigma_{1/2}\right)}{\sqrt{2}\widetilde{\sigma}}\right)\right].
\end{aligned}
\tag{5.4}
$$

The first order kinetics presuming threshold stresses - $dn/dt = -kn$ for cells with $\sigma_t < \sigma$ and $dn/dt = 0$ for $\sigma_t > \sigma$ - lead to a time-dependent expression for the percentage of detached cells (140):

$$n(t) = e(\sigma)\left(1 - \exp\left(-k(\sigma)t\right)\right). \tag{5.5}$$

The detachment efficiency, which stands for for the percentage of detached cells for $t = \infty$, links the kinetics with the threshold stress distribution eq. 5.4.

5.2.3 Adhesion threshold for amoeboid cells follow lognormal distribution

	DH1$_{glass}$ (FM) 1	DH1$_{glass}$ (FM) 2	DH1$_{glass}$ (FM) 3	DH1$_{glass}$ (FM)	DH1$_{glass}$ (HCM).	DH1$_{APTES}$ (FM)
$\sigma_{1/2}$ [Pa]	0.30 $\pm$ 0.02	0.31 $\pm$ 0.02	0.30 $\pm$ 0.02	0.32 $\pm$ 0.02	0.32 $\pm$ 0.02	0.65 $\pm$ 0.03
$\widetilde{\sigma}$	0.47 $\pm$ 0.08	0.54 $\pm$ 0.08	0.54 $\pm$ 0.08	0.48 $\pm$ 0.07	0.48 $\pm$ 0.08	0.52 $\pm$ 0.07

Table 5.1: Left: Reproducibility among channels. Adhesion strength distribution parameters for three parallel channels with same conditions (*Dictyostelium* DH1 cells in fresh medium on glass substrate). **Right:** Results for adhesion on glass in fresh medium (FM), on glass in highly conditioned medium (HCM), and in FM on an APTES-coated surface.

The experimentally obtained detachment curves shown in Fig. 5.2 are very well fitted with first order kinetics for each cell line, leading to a stress dependent detachment rate k (Fig. 5.3B).

The detachment efficiency which corresponds to the asymptotic state value in Fig. 5.2 is plotted as a function of σ in Fig. 5.3A. The experimental values for each cell line are fitted by the lognormal cumulative distribution function.

The occurrence of lognormal distributions for biological quantities is well-known and also successfully applied for adhesive strength distributions (140, 148), but not well-understood. There is not only a single standard generative model which produces lognormal populations, but several possible mechanisms which can lead to lognormality. Yet, key idea is the accumulation of multiplicative (and not additive, which leads to normal distributions) random effects. For cellular objects, these multiplicative random effects may occur by asymmetrical cell division or external random effects whose impact depend on the actual state of the cell. We refer to (157) for a biology-oriented introduction to generative models for lognormal distributions. Our data (Fig. 5.3A) fit very well to the lognormal cumulative distribution function and therefore give support to the idea of lognormal distributed threshold stresses for single cells, independently of the cell type.

5.2.4 Quantitative comparison of detachment parameters

For a quantitative discussion of adhesion parameters and to assess the precision and the robustness of our device, we investigate two main possible error sources:

1. Statistical and counting errors δ_N; a limited number of cells creates a statistical error when data are described by a given distribution law as given in eq. 5.3.

2. Physical incertitudes and device approximations of the wall shear stress δ_σ: flow velocity field and thus shear stress values may be modified by PDMS deformation due to internal pressure; temperature-dependency of viscosity can affect the shear stress as well; also channel width and thus shear stress are not constant over a given field of view.

A detailed discussion of these main error sources and their estimate (Master thesis of Peter Rupprecht) is given in appendix B. As far as the second error source is concerned, δ_σ mostly depends on the channel height error ($\delta_{h(x)} \simeq 2\ \mu$m and is almost independent of x). However, a proper measurement of $h(x)$ by confocal microscopy was performed for high shear stress conditions; in a first approximation, deformation increases linearly with channel width (cf. supplementary information, where we refer in detail to (158) for a theoretical framework). To estimate the error of the fit parameters $\sigma_{1/2}$ and $\widetilde{\sigma}$ in eq. 5.4 due to the limited experimental
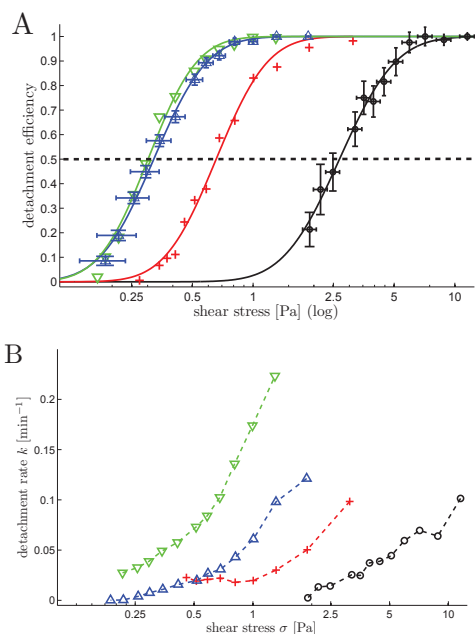
Figure 5.3: Detachment efficiency and detachment rate for different experiments. **A.** The cumulative lognormal threshold-stress distribution function (cdf), fitted with eq. 5.4 for four datasets, listed from left to right: *Dictyostelium* on glass substrate in highly conditioned medium (green, downward pointing triangles) and in fresh medium (blue, upward pointing triangles), in fresh medium on APTES-coated substrate (red, crosses), and MDA-MB-231 on collagen-coated substrate (black, circles). Every datapoint for the *Dictyostelium* data in fresh medium corresponds to one position in Fig. 2.7. Error bars are shown for one condition each for *Dictyostelium* and MDA-MB-231 to give an idea of magnitude. $\sigma_{1/2}$ can be read off at the point where the dashed line intersects the fits. **B.** Detachment rates k, obtained by first order kinetics fits. The color/symbol code is the same as in subfigure A. Stress errors are the same as for subfigure A, fit errors for k are of the size of the symbols. Data points without significant detachment (APTES for $\sigma < 0.5$ Pa) could not be fitted properly and were left out. Data points are connected as a guide for the eye.

sample, *i.e.* the finite cell number, we used a numerical resampling method. Combining the primary error sources as root of the squares, we are able to give a total error estimation. For best conditions for *Dictyostelium*, it is about 6% of the value for $\sigma_{1/2}$ and 13% of the value for $\widetilde{\sigma}$.

Reproducibility among different parallel channels was verified with good accordance of adhesion strength from one channel to another, see Tab. 5.1, left hand side.

It is therefore possible to fully use the independent channels of our device in parallel to compare simultaneously the cells from the same culture in different environments. In Fig. 5.3, three different conditions for *Dictyostelium* are shown. *Dictyostelium* in fresh HL5 medium on glass substrate yields $\sigma_{1/2} = 0.32$ Pa. Coating the glass substrate with APTES increases adhesion strength significantly to $\sigma_{1/2} = 0.65$ Pa; this increase has already been reported by (140).

Another possibility besides surface treatment to modify detachment of cells, is modifying the medium. Highly conditioned medium (HCM) is obtained from *Dictyostelium* cell cultures; the medium therefore is enriched with various biomolecules that are naturally produced by *Dictyostelium* in cell culture. Some of these molecules can dock to extracellular receptors, which impedes non-attached receptors to interact with the substrate. We discussed this in the context of cell migration (see chapter 3), where we observed lower motility and more rounded cells for *Dictyostelium* in HCM (27). For adhesion, we found no difference for $\sigma_{1/2}$ for fresh medium and HCM, see Fig. 5.3A. By contrast, detachment kinetics were much faster in HCM (Fig. 5.3B and Fig. 5.2A, highlighted curves). These findings suggest that attachment and re-attachment of receptors, which is reduced by HCM as described above, plays an important role in the detachment process, but does not significantly determine the threshold stress value for our experiments with *Dictyostelium* , *i.e.* the decision if a cell is detached at a given stress or not. This example illustrates the need for having access to detachment kinetics. It enabled to highlight differences in cell detachment which are not revealed by $\sigma_{1/2}$ values.

In (140), experiments with *Dictyostelium* were carried out in buffer (whereas we used HL5 medium); buffer media are of simple constitution, the number of parameters which may influence an experiment is reduced. On the other hand, a buffer is not a natural environment, leading to complications like osmotic shocks and starvation. We found that adhesion is weaker for *Dictyostelium* in HL5 compared to values given by (140) for experiments using buffer. The difference is about one order of magnitude. This indicates that adhesive contacts are strengthened in buffer medium. Due to lower applied shear stresses, detachment in HL5 is much slower (Fig. 5.2A,5.3B) than in buffer. In buffer, (140) found typical detachment times of ≈ 5 min, whereas we got characteristic times of 1 hour (Fig. 5.2A). As shown in Fig. 5.3B, kinetics are generally faster with increasing shear stresses.

Also, we did preliminary experiments to study cell adhesion in the course of Development. We performed a comparative study of adhesion in DB after 1h and 8 hours of starvation (see

Annexe F.). We found that cell adhesion significantly decreases with starvation time with a $\sigma_{1/2} = 0.54 \pm 0.04$Pa and 0.33 ± 0.03Pa after 1 hour and 8 hours of starvation, respectively.

Finally we performed preliminary experiments with two *Dictyostelium* mutants: ko-SibA which lacks subset of integrin like proteins and MaM4, a mutant currently studied in Pierre Cosson laboratory (Geneva, Switzerland) with unknown function. Measured $\sigma_{1/2}$ are 0.16 ± 0.03 Pa and 0.29 ± 0.02 Pa, respectively for those two mutants.

5.2.5 Cell tracking, migration, detachment mode

In addition to kinetics resolution and the possibility of parallel experiments, our device is also adapted to measurements of adhesion and cell tracking simultaneously. This allows to enhance the comprehension of detachment kinetics by analyzing cell shape modifications and migrative behavior. *Dictyostelium* , as stated above, are detached on a typical timescale of up to 1 hour for an applied hydrodynamic stress close to $\sigma_{1/2}$ in fresh medium. The detachment for *Dictyostelium* is described by (149) as a peeling process which begins with the onset of the experiment. In this model, the microscopic peeling velocity v_p, which is a function of some microscopic parameters, is connected with the detachment rate k and the peeling time τ using the cell dimension l_c: $k \propto 1/\tau = v_p/l_c$. Our tracking analysis however shows that cells are able to migrate normally during up to 1 hour before detachment. The trajectories show diffusive behavior for low shear stresses and only partially directed flow-driven movement for high stresses (Fig. 5.4B-D).

The motility of *Dictyostelium* is therefore not disabled by shear stresses, and the peeling process does not start with flow onset, but at a stochastically determined moment. This is clearly visible on the cell of Fig. 5.4A submitted to a very high applied shear stress (2.6 Pa $\approx$ $4\sigma_{1/2}$). It first moves by extending several forward but also lateral pseudopods (see arrows in Fig. 5.4A) but finally stops migration, rounds up and is detached. It is therefore not possible to link microscopic and macroscopic kinetics within the framework of (149) for *Dictyostelium* in natural-like environment (HL5 medium). This conclusion would not have been possible without the possibility to track the motion of cells.

5.3 Conclusion

We have designed and tested a simple 4-channel tapered microfluidic device for cell adhesion strength measurements based on the analysis of cellular response to varying hydrodynamic
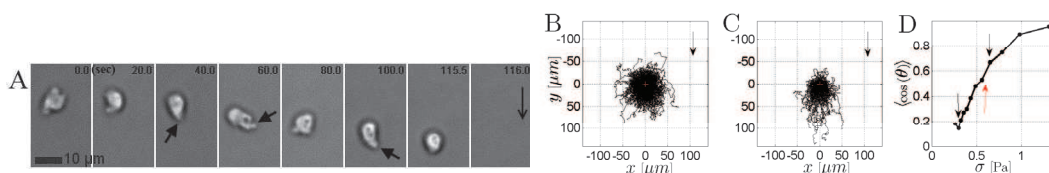
Figure 5.4: *Dictyostelium* cells motility during a detachment experiment on APTES coated substrate. **A.** Detachment of a single *Dictyostelium* cell at 20x magnitude, at 2.6 Pa: despite the very high stress, the cell extends also lateral pseudopods (arrows) and migrates. Finally the cell rounds and detaches. The arrow in the last frame indicates the flow direction. **B.,C.** Centered trajectories of at least 150 cells submitted to a shear stress of 0.25 Pa (B) and 0.70 Pa (C) respectively over 52 min. Cell migration is almost random at low shear stresses, whereas it is strongly biaised in flow direction for higher shear stresses. Flow direction is given by arrows. **D.** Mean directionality of cell movement as a function of applied shear stress, indicating to which extent migration is aligned with flow direction. Directionality is defined as the angle between the flow direction and the cell movement direction over a 52 min interval. Therefore, $\cos(\theta) = 1$ indicates fully biased cell movement in flow direction, $\cos(\theta) = 0$ indicates random direction of migration. The chosen positions B. and C. are represented by black arrows, $\sigma_{1/2} = 0.65$ Pa by the red arrow.

shear stresses. Compared to other recent microfluidic shear stress designs, our device offers a larger shear stress range and a better and very precise detachment kinetics measurement. The device was also tested on a breast cancer cell line (MDA-MB231) (155). This allowed us to confirm that first order kinetics and lognormal distributions for the proportion of detached cells are very general laws describing well either amoeboid *Dictyostelium* and mesenchymal breast cancer cells.

We would like to stress here that kinetics (Fig. 5.2) could be obtained by a single experiment, observed at more than 200 time-steps. In contrast, (140) did one experiment for one experimental data point. We hold this for a major improvement of our device: evidently, it reduces the effort; secondly, it can be checked if an asymptotic state is attained in a single experiment. Generally, it is often preferable to acquire biological data for one issue at the same time for reasons of comparability. This allows to distinguish variations due to biological heterogeneity of a sample and those due to other changes of experimental parameters.

Another advantage of our device is the possibility to track cells (single cells or few hundreds as well) and therefore to better understand adhesion through migration analysis. In addition, visualization during experiments gives feedback over possible problems and allows to show *e.g.* the mode of detachment, which can bring forward cell detachment modeling. Because each channel is fully independent of the others, the effect of several environmental parameters

(substrate coating, buffers, drugs . . .) on adhesion and migration can be tested simultaneously. Besides, influence of shear stress on other parameters of interest can be easily measured without device alterations. For instance, influence of shear stress on cell division for *Dictyostelium* was an issue that occurred while testing our device. It is a versatile tool that could be used to analyze not only detachment strength and kinetics for different cell types in varying environmental conditions, but also putative shear stress dependent cell behavior such as cell motion.

Chapter 6

Conclusion & Perspectives

Throughout this work I have shown that individual *Dictyostelium* cell migration is dependent of various parameters. I will state here the major results of our work. Thanks to the methods we develop to characterize cell migration as well as cell adhesion, some novel aspects of migration have been highlighted: (*i*) if no taxis is involved, cell move purely diffusively, (*ii*) cell migration is strongly influenced by cell density, (*iii*) major migration changes during development are due to an increase of persistence and an increase in cell activity, rather than a modification of the intrinsic velocity. As far as the migration-adhesion interplay is concerned, the picture stays unclear after this thesis. Nevertheless, the results suggest that adhesion has a minor effect on migration compare to other environmental cues.

6.1 Development of efficient tools for statistical analysis of cell migration and adhesion

During this work, we have developed tools to automate the recordings of video microscopy and image analysis. This improvement allows us to work with very large samples of cells and to quantify cell migration on a population level. A reliable and reproducible diffusion constant over months for each experimental conditions required at least 100 cells ($\sim$ 100000 positions) due to large distribution of cell behavior. To the light of our results, averaging 10 cells *MSD* as often done in the literature (103, 104, 105) seems inappropriate to quantify migration, even if very long recording time are used.

We were very precocious of cell culture condition and our method allowed us to get reproducible results. Parameters such as cell diffusion constant, cell persistence and cell roundness were gathered for different environmental conditions (the substrate, the medium, and the type of cells). In parallel, we developed a microfluidic tapered channel device to quantify cell detachment in hydrodynamic flow. This device combined with a motorized stage has allowed a statistical study of adhesion but also the dynamics of detachment. Using 4 channels in parallel allows us to study various parameters simultaneously and gather large data, necessary to have reproducible results. We could quantify cell adhesion as well as cell detachments kinetics. A major improvement is the possibility of live tracking cells to have better insight into cell detachment kinetics whereas it is not possible other systems (140).

6.2 New aspect of dicty cell dynamics

6.2.1 Random migration of *Dictyostelium* is purely diffusive

The true nature of cell motion is still largely controversial: many groups have found anomalous diffusion experimentally and made hypothetical explanation of this phenomenon (102, 103). In light of the work done during this thesis, it is likely that the experiments that found anomalous diffusion often did not last long enough to detect the long term features of highly persistent cells (102, 103, 105). Cell traces were typically only a few cell-diameters long. Under these conditions, it is difficult to distinguish true superdiffusion from correlated random walk (117). Our statistical analysis of cell migration answered this question. It is now clear if no taxis phenomena[1] are involved, that cells always reach random diffusion as long as the tracking time

---

[1]Here, taxis referred to all environmental cues that may bias cell trajectories such as chemotaxis or haptotaxis

is long enough compared to the persistence of cells.

6.2.2 Antagonist effect of cell density on cell migration for vegetative and starved cells

The analysis of the role played by cell-density in the course of development highlight crucial differences in cell-cell signaling between vegetative and starved state. While cells move faster at low cell density in nutritive conditions, the opposite behavior is found in development: cells move faster at high cell density. The experiences of migration in growth medium revealed the presence of a QSF secreted by the cells. This QSF appears as a major variable regulating their random migration. The diffusion coefficient, the persistence of the movement and morphology of cells vary depending on the concentration of this factor. Studying cell migration in the course of development confirmed that cell migration is strongly dependent on cell-cell signaling and that the highest rate of migration is reached after ~ 6 hours of starvation. It highlights the role of density on cell differentiation and migration capacity. At this stage, cell density triggers in concert QS sensing (via CMF) and cAMP signaling.

6.2.3 Individual cells do not change their mode of locomotion in the course of development

Our work revealed that cell migration is positively correlated with persistence (Fig. 6.1) and negatively correlated with the cell shape (Fig. 6.2). By plotting the mean persistence length as a function of the diffusion coefficient for the whole cell stages (vegetative in black and starved in red), all experimental points are gathering in a single straight line (Fig. 6.1A). This is the main results of bimodal analysis: cells increase their persistence instead of their speed to explore larger areas (*i.e.*, increasing their D) (Fig. 6.1). This statement is true whether the cell is in nutrient medium or in the course of development. It is consistent with results obtained by the pseudopod analysis of Van Haaster *et al.* (116): starved cells are faster than vegetative cells not by extending more pseudopods and/or increasing their speed but by moving longer in the same direction. Surprisingly, Fig. 6.1B shows that for an identical D cells spend less time in persistent mode in DB than in HL5. However, these group of data concerned either dedifferentiated cells, or early starvation times (0-2h), where the majority of cells are rounded (see Fig. 6.2), and slower than in nutritive medium. It nevertheless suggests that in these extreme cases, there would be a small intrinsic difference in cell speed. For longer starvation time, cells are more elongated (see Fig. 6.2) and move faster.
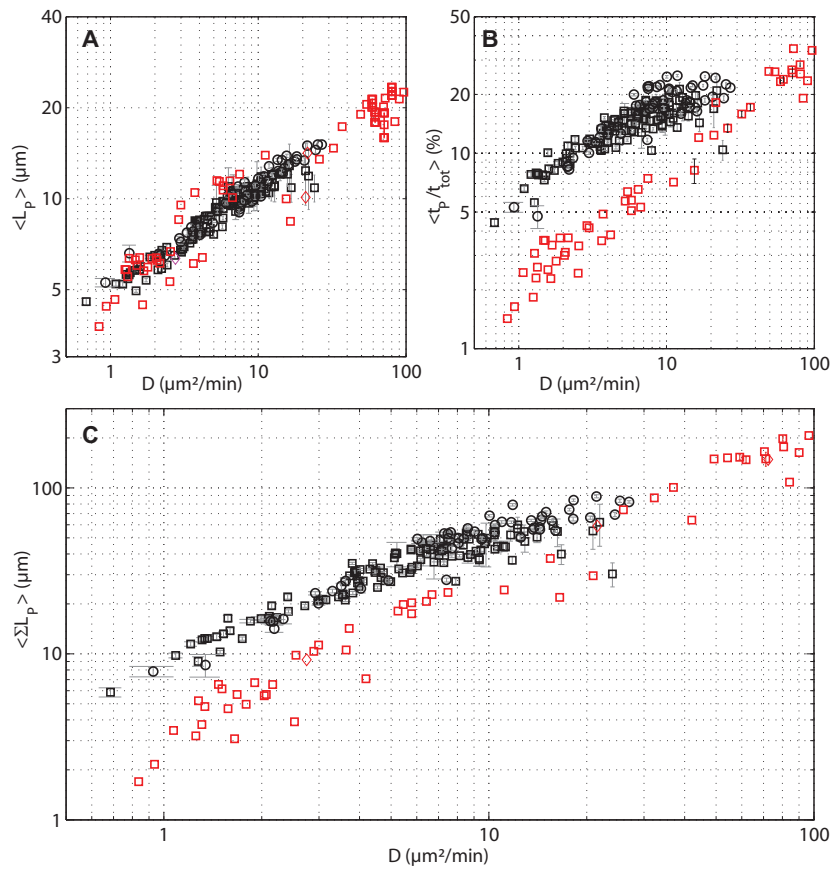
Figure 6.1: Persistence characterization. Bimodal analysis results for cells in HL5 (Black squares) and in DB (red squares). Error bars represents SEM. (**A**) Cells follow the same law for both conditions. (**B**) for identical D^* cell in Development have a lower ratio of persistence than cell in HL5. (**C**) As the cumulative persistence length is roughly the product of mean persistent length (**A**) times persistent ratio (**B**), the difference here is due to the difference in persistent ratio.
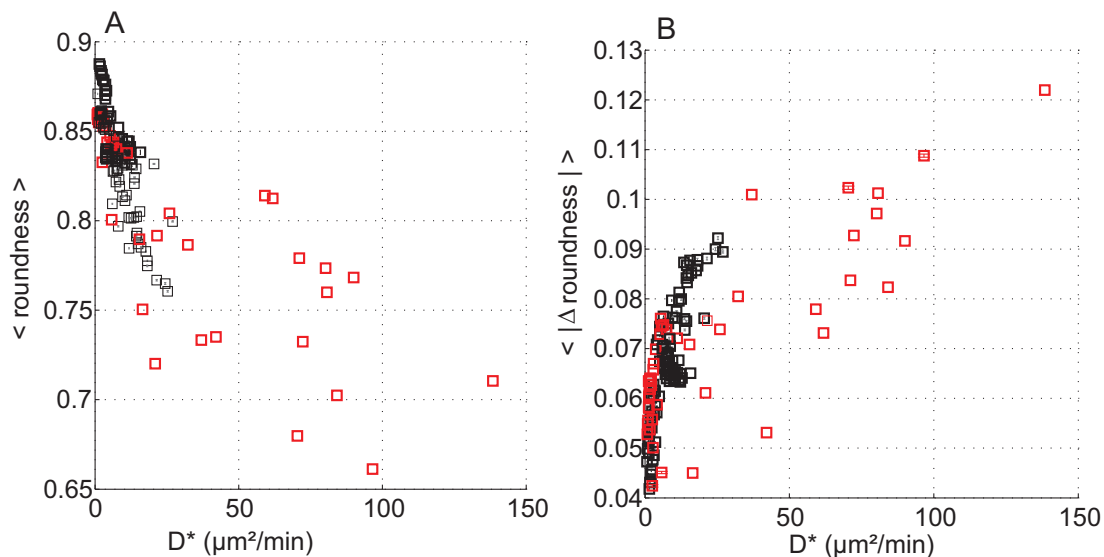
Figure 6.2: Shape analysis. Cells in HL5 (Black squares) and in DB (red squares) follow the same law for both roundness (**A**) and roundness variation (**B**). Error bars represents SEM.

Fig. 6.2 shows that correlation between cell diffusion and cell shape are identical in DB and HL5.

Both bimodal and cell shape analysis are highlighting the fact that *Dictyostelium* cells motion is amoeboid like in all experimental conditions we explored (*i.e.*, fast shape variation and rate of migration directly related to the length of persistence). For example a Keratocyte like type of motion would present a saturation of cell roundness variation with increasing *D* as there is no cell cycle of extension retraction unlike in amoeboid mode. Therefore it is also an interesting method to define migration mode.

6.2.4 Migration-Adhesion interplay

Throughout this work we have shown that individual *Dictyostelium* cell migration is dependent of various parameters and in particular, it is dependent on cell density and cell starvation time. The methods developed in this thesis to quantify cell migration allowed us to make a comparative study of migration by varying other parameters such as surface or the chemical composition of experimental medium. As far as starved cells are concerned, we showed that cell adhesion decreases with the time of starvation whereas the migration rate increases (appendix F.). This is consistent with the evolution of traction forces that also decrease in the course of development (28). Nevertheless, changes in cell adhesion are much smaller than

changes in cell migration (2 fold decreases in cell adhesion ($\sigma_{1/2}$) compare to 50 fold increases in apparent diffusion constant)). It seems therefore that cell adhesion as a minor effect on cell migration as compared to other environmental cues such as cAMP signaling.

For longer developmental time, similar cell speed and persistence were found for cells migrating outside or inside cell-streams (111). In that case biochemical and mechanical modifications induced by cell-substrate versus cell-cell adhesion does not influence cell migration. Cells in the same developmental stage move similarly, no matter the interaction with the substrate. It indicates that cell migration is once again mainly governed by soluble factors and molecules rather than regulating by cell-substrate or cell-cell adhesion.

In the following, we will try to outline in more detail the possible role played by adhesion in migration of *Dictyostelium* in nutrient medium. To that goal, we studied migration of ko-SibA mutant cells and migration on APTES coated substrate in both fresh medium and highly conditioned medium (see Fig. 3.11). Our set-up was also used to quantify cell migration and adhesion of a new mutant currently under investigation in the group of P. Cosson: Mam4. For every experimental conditions, cell adhesion has been quantified in parallel. As a first attempt to draw a picture of the adhesion-migration interplay in *Dictyostelium* , one can represents the average diffusion coefficient (that quantify cell migration) as a function of shear stress necessary to detach cells (representing cell adhesion, Fig. 6.3).

From this graph, it is rather difficult to give a clear answer concerning the interplay between cell migration and adhesion. We will therefore, discuss different possibilities. First, it has been shown that the stress necessary to detach half of the cell population is independent of the cytoskeleton dynamics (140). It is therefore rather a measurement of passive cell-substrate interactions that does not take into account the dynamic of adhesion-de-adhesion coupled to myosinII-actin activity. This is also confirmed in this thesis, as for every mutants and substrates used, despite a 3 to 10 fold decrease of D, QSF barely affects the shear stress necessary to detach half of the cell population but modify drastically the dynamics of detachment (Fig. 6.4A).

To get insight into this dynamic, it is thus tempting to compare the kinetics of cell detachment. However, no better correlations between the diffusion constant and the detachment rate are found (Fig. 6.4B). From this analysis, one logical explanation of the results could be that *Dictyostelium* is mainly moving via an independent-adhesion mechanism, mainly governed by factors and molecules secreted and sensed by the cells. This is consistent with a
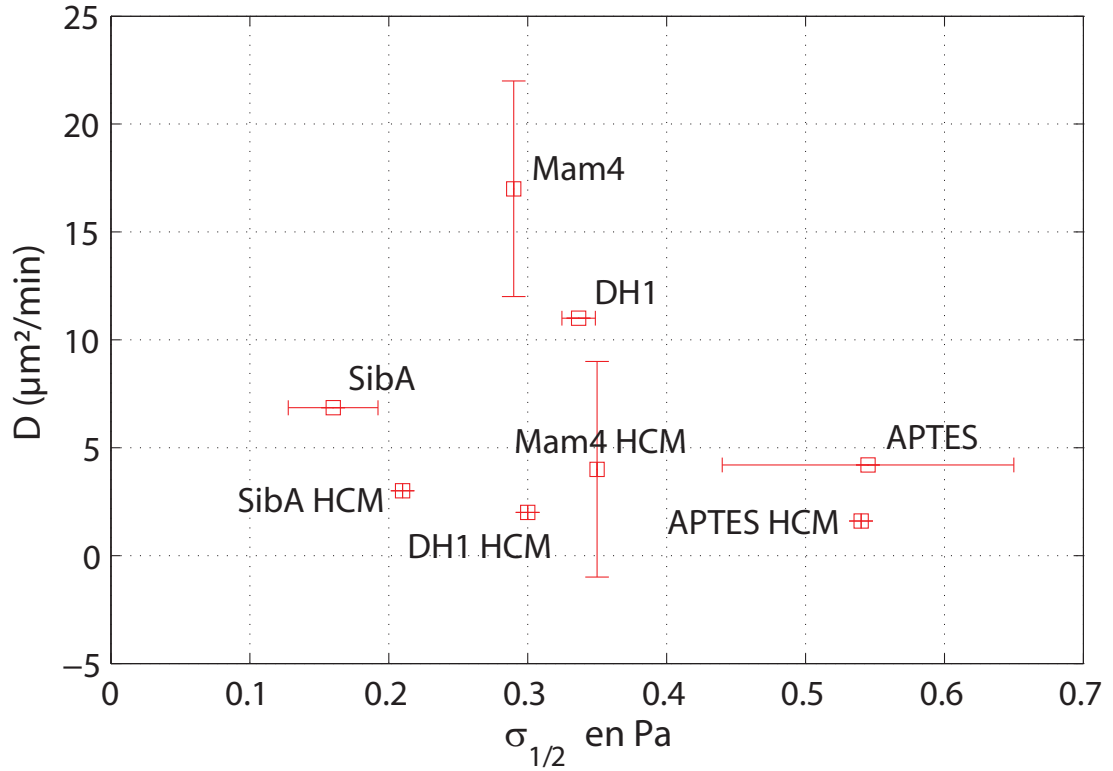
Figure 6.3: *Dictyostelium* **diffusion constant** *D* **Versus Adhesion.** Error bars represents SEM.
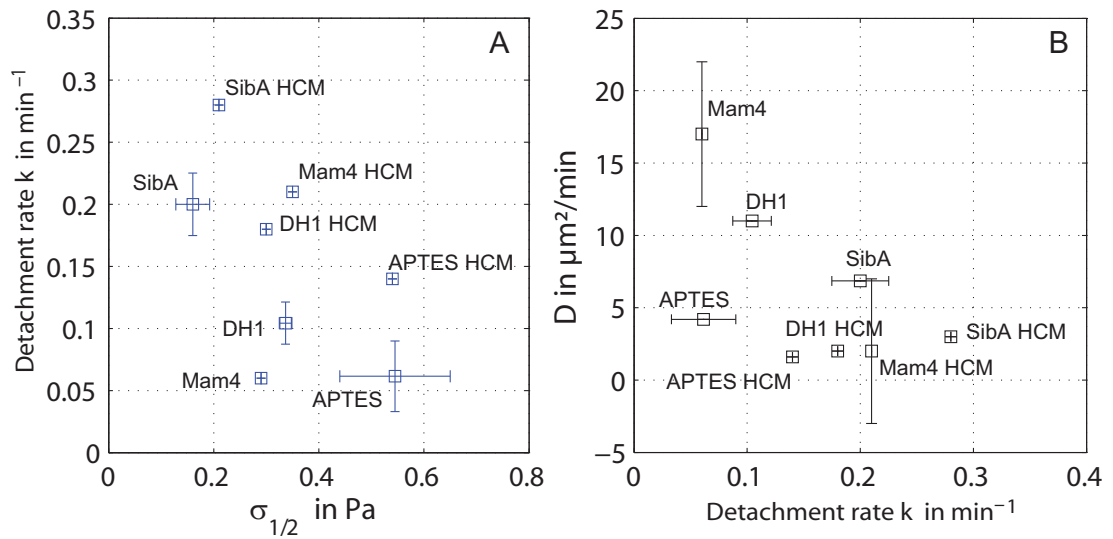
Figure 6.4: *Dictyostelium* **diffusion constant Versus Adhesion.** (**A**) Detachment rate *k* as a function of $\sigma_{1/2}$. (**B**) *D* as a function of *k*. Error Bars represent SEM.

recent model, where cell speed were found to be roughly constant for a large range of values of adhesive forces (159). In their model, cell motion can be described by a contraction-relaxation-protrusion cycle (as opposed to the classical extension (driven by actin)-retraction (driven by myosinII) cycle). The cell speed is determined by the ratio of the displacement per cycle and the period of this cycle. In that case, it would indicate that migration is mainly driven by actin polymerization at the front, rather than myosin-II contraction at the rear. In accordance to this model, even if a good colocalisation of traction forces and myosin-II was found for both vegetative and aggregation-competent cells (28), other studies have shown that in aggregation-competent cells, most rearward traction stresses emerged at spots where accumulation of F-actin took place and did not involve myosin II (59). In addition, entirely polymerization-driven protrusions were demonstrated in *Dictyostelium* (18, 41), as well as in other amoeboid cells such as T lymphocytes (160), leukocytes (161) and dendritic cells (40) upon blockade of myosin II. The shear force of polymerization was apparently sufficient to protrude the membrane. It is also similar to the polymerization-driven protrusion in nematode sperms (162), where polymeric filaments are used for locomotion. Remarkably, these cells were still able to migrate in low-adhesive 2D or confined environments.

To validate this hypothesis, rather than modifying the substrate, it would be interesting in future studies to take advantage of the statistical analysis developed in this thesis to rigorously compare cell migration and cell adhesion on mutant lacking some key components driving the cytoskeleton dynamic such as myosinII, TalinA or PaxB (*Dictyostelium* ortholog of paxilin).

References

[1] P Friedl, S Borgmann, and E B Bröcker. **Amoeboid leukocyte crawling through extracellular matrix: lessons from the Dictyostelium paradigm of cell movement.** *Journal of leukocyte biology*, **70**(4):491–509, October 2001. 2, 3, 13

[2] S P Palecek, J C Loftus, M H Ginsberg, D A Lauffenburger, and A F Horwitz. **Integrin-ligand binding properties govern cell migration speed through cell-substratum adhesiveness.** *Nature*, **385**(6616):537–40, March 1997. 3

[3] Isabelle Delon and Nicholas H Brown. **Integrins and the actin cytoskeleton.** *Current opinion in cell biology*, **19**(1):43–50, February 2007. 3

[4] Marc R Block, Cedric Badowski, Angelique Millon-Fremillon, Daniel Bouvard, Anne-Pascale Bouin, Eva Faurobert, Delphine Gerber-Scokaert, Emmanuelle Planus, and Corinne Albiges-Rizo. **Podosome-type adhesions and focal adhesions, so alike yet so different.** *European journal of cell biology*, **87**(8-9):491–506, September 2008. 3, 7

[5] Gary J Doherty and Harvey T McMahon. **Mediation, modulation, and consequences of membrane-cytoskeleton interactions.** *Annual review of biophysics*, **37**:65–95, January 2008. 4

[6] Paul A. Janmey Qi Wen. **Polymer physics of the cytoskeleton.** *Current Opinion in Solid State and Materials Science*, **15**(5):177–182, October 2011. 4

[7] Xavier Trepat, Guillaume Lenormand, and Jeffrey J. Fredberg. **Universality in cell mechanics.** *Soft Matter*, **4**(9):1750, July 2008. 4

[8] Carlos Jurado, John R Haserick, and Juliet Lee. **Slipping or gripping? Fluorescent speckle microscopy in fish keratocytes reveals two different mechanisms for generating a retrograde flow of actin.** *Molecular biology of the cell*, **16**(2):507–18, February 2005. 6

[9] T Mitchison and M Kirschner. **Cytoskeletal dynamics and nerve growth.** *Neuron*, **1**(9):761–72, November 1988. 6

[10] Alberts. **Molecular Biology of the Cell**, 2002. 6, 8, 9, 10

[11] Mario Gimona, Carsten Grashoff, and Petra Kopp. **Oktoberfest for adhesion structures.** *EMBO reports*, **6**(10):922–6, October 2005. 7

[12] Benjamin Geiger and Kenneth M Yamada. **Molecular architecture and function of matrix adhesions.** *Cold Spring Harbor perspectives in biology*, **3**(5), January 2011. 6

[13] Allison L Berrier and Kenneth M Yamada. **Cell-matrix adhesion.** *Journal of cellular physiology*, **213**(3):565–73, December 2007. 6

[14] Carlier C, LeClainche MF. **Regulation of actin assembly associated with protrusion and adhesion in cell migration.** *Physiological reviews*, **88**(2):489–513, April 2008. 7

[15] Fiona M Watt. **Role of integrins in regulating epidermal adhesion, growth and differentiation.** *The EMBO journal*, **21**(15):3919–26, August 2002. 7

[16] Martin A Schwartz. **Integrin signaling revisited.** *Trends in Cell Biology*, **11**(12):466–470, December 2001. 8

[17] M W Renshaw, D Toksoz, and M A Schwartz. **Involvement of the small GTPase rho in integrin-mediated activation of mitogen-activated protein kinase.** *The Journal of biological chemistry*, **271**(36):21691–4, September 1996. 9

[18] P Y Jay, P A Pham, S A Wong, and E L Elson. **A mechanical function of myosin II in cell motility.** *Journal of Cell Science*, **108 (Pt 1)**(1):387–393, 1995. 11, 21, 22, 86, 106

[19] S Munevar, Y Wang, and M Dembo. **Traction force microscopy of migrating normal and H-ras transformed 3T3 fibroblasts.** *Biophysical journal*, **80**(4):1744–57, April 2001. 11

[20] M F Ware, A Wells, and D A Lauffenburger. **Epidermal growth factor alters fibroblast migration speed and directional persistence reciprocally and in a matrix-dependent manner.** *Journal of cell science*, **111 (Pt 1**:2423–32, August 1998. 11

[21] Y Xiao and G A Truskey. **Effect of receptor-ligand affinity on the strength of endothelial cell adhesion.** *Biophysical journal*, **71**(5):2869–84, November 1996. 11, 87

[22] X Zhang, P Jones, and S Haswell. **Attachment and detachment of living cells on modified microchannel surfaces in a microfluidic-based lab-on-a-chip system.** *Chemical Engineering Journal*, **135**:S82–S88, January 2008. 11

[23] T Oliver, M Dembo, and K Jacobson. **Separation of propulsive and adhesive traction stresses in locomoting keratocytes.** *The Journal of cell biology*, **145**(3):589–604, May 1999. 11

[24] Andrew D Doyle and Juliet Lee. **Cyclic changes in keratocyte speed and traction stress arise from Ca2+-dependent regulation of cell adhesiveness.** *Journal of cell science*, **118**(Pt 2):369–79, January 2005. 11

[25] Lee A Smith, Helim Aranda-Espinoza, Jered B Haun, and Daniel A Hammer. **Interplay between shear stress and adhesion on neutrophil locomotion.** *Biophysical journal*, **92**(2):632–40, January 2007. 11

[26] Lee A Smith, Helim Aranda-Espinoza, Jered B Haun, Micah Dembo, and Daniel A Hammer. **Neutrophil traction stresses are concentrated in the uropod during migration.** *Biophysical journal*, **92**(7):L58–60, April 2007. 11

[27] Laurent Golé, Charlotte Rivière, Yoshinori Hayakawa, and Jean-Paul Rieu. **A quorum-sensing factor in vegetative Dictyostelium cells revealed by quantitative migration analysis.** *(Accepted in PLoS One)*, 2011. 11, 95

[28] H Delanoë-Ayari, S Iwaya, Y T Maeda, J Inose, C Rivière, M Sano, and J-P Rieu. **Changes in the magnitude and distribution of forces at different Dictyostelium developmental stages.** *Cell motility and the cytoskeleton*, **65**(4):314–31, April 2008. 11, 17, 18, 19, 21, 22, 53, 72, 73, 103, 106

[29] Alex Mogilner and Kinneret Keren. **The shape of motile cells.** *Current biology : CB*, **19**(17):R762–71, September 2009. 12

REFERENCES

[30] R J PELHAM AND Y L WANG. **High resolution detection of mechanical forces exerted by locomoting fibroblasts on the substrate.** *Molecular biology of the cell*, **10**(4):935–45, April 1999. 11

[31] SANDRINE ETIENNE-MANNEVILLE. **Actin and microtubules in cell motility: which one is in control?** *Traffic (Copenhagen, Denmark)*, **5**(7):470–7, July 2004. 11

[32] IRINA KAVERINA, OLGA KRYLYSHKINA, AND J VICTOR SMALL. **Regulation of substrate adhesion dynamics during cell motility.** *The international journal of biochemistry & cell biology*, **34**(7):746–61, July 2002. 11

[33] J LEE, A ISHIHARA, J A THERIOT, AND K JACOBSON. **Principles of locomotion for simple-shaped cells.** *Nature*, **362**(6416):167–71, March 1993. 12

[34] T M SVITKINA, A B VERKHOVSKY, K M MCQUADE, AND G G BORISY. **Analysis of the actin-myosin II system in fish epidermal keratocytes: mechanism of cell body translocation.** *The Journal of cell biology*, **139**(2):397–415, October 1997. 13

[35] J LEE, M LEONARD, T OLIVER, A ISHIHARA, AND K JACOBSON. **Traction forces generated by locomoting keratocytes.** *The Journal of cell biology*, **127**(6 Pt 2):1957–64, December 1994. 13

[36] URSULA EUTENEUER AND MANFRED SCHLIWA. **Persistent, directional motility of cells and cytoplasmic fragments in the absence of microtubules.** *Nature*, **310**(5972):58–61, July 1984. 13

[37] A B VERKHOVSKY, T M SVITKINA, AND G G BORISY. **Self-polarization and directional motility of cytoplasm.** *Current biology : CB*, **9**(1):11–20, January 1999. 13

[38] TIM LÄMMERMANN AND MICHAEL SIXT. **Mechanical modes of 'amoeboid' cell migration.** *Current opinion in cell biology*, **21**(5):636–44, October 2009. 13

[39] S YUMURA AND Y FUKUI. **Spatiotemporal dynamics of actin concentration during cytokinesis and locomotion in Dictyostelium.** *Journal of cell science*, **111 (Pt 1**:2097–108, August 1998. 13, 21

[40] R J HAWKINS, M PIEL, G FAURE-ANDRE, A M LENNON-DUMENIL, J F JOANNY, J PROST, AND R VOITURIEZ. **Pushing off the walls: a mechanism of cell motility in confinement.** *Physical review letters*, **102**(5):058103, February 2009. 13, 106

[41] KUNITO YOSHIDA AND THIERRY SOLDATI. **Dissection of amoeboid movement into two mechanically distinct modes.** *Journal of cell science*, **119**(Pt 18):3833–44, September 2006. 13, 106

[42] G T CHARRAS. **A short history of blebbing.** *Journal of microscopy*, **231**(3):466–78, September 2008. 13

[43] JÖRG RENKAWITZ, KATHRIN SCHUMANN, MICHELE WEBER, TIM LÄMMERMANN, HOLGER PFLICKE, MATTHIEU PIEL, JULIEN POLLEUX, JOACHIM P SPATZ, AND MICHAEL SIXT. **Adaptive force transmission in amoeboid cell migration.** *Nature cell biology*, **11**(12):1438–43, December 2009. 14

[44] P N DEVREOTES AND S H ZIGMOND. **Chemotaxis in eukaryotic cells: a focus on leukocytes and Dictyostelium.** *Annual review of cell biology*, **4**:649–86, January 1988. 14

[45] KB RAPER. **Dictyostelium discoideum, a new species of slime mold from decaying forest leaves.** *J Agr. Res.*, **50**:135–47, 1935. 14

[46] LOUISE FETS, ROB KAY, AND FRANCISCO VELAZQUEZ. **Dictyostelium.** *Current biology : CB*, **20**(23):R1008–10, December 2010. 15, 16

[47] KESSIN, R.H. *Dictyostelium: evolution, cell biology, and the development of multicellularity*. Cambridge University Press, Cambridge, UK, 2001. 14

[48] PIERRE COSSON AND THIERRY SOLDATI. **Eat, kill or die: when amoeba meets bacteria.** *Current opinion in microbiology*, **11**(3):271–6, June 2008. 16

[49] L EICHINGER, J A PACHEBAT, G GLÖCKNER, M-A RAJANDREAM, R SUCGANG, M BERRIMAN, J SONG, R OLSEN, K SZAFRANSKI, Q XU, AND ET AL. **The genome of the social amoeba Dictyostelium discoideum.** *Nature*, **435**(7038):43–57, 2005. 16

[50] PETER J M VAN HAASTERT AND PETER N DEVREOTES. **Chemotaxis: signalling the way forward.** *Nature reviews. Molecular cell biology*, **5**(8):626–34, August 2004. 17, 21

[51] D R SOLL. **Computer-assisted three-dimensional reconstruction and motion analysis of living, crawling cells.** *Computerized medical imaging and graphics : the official journal of the Computerized Medical Imaging Society*, **23**(1):3–14, January 1999. 17, 72

[52] D WESSELS, E VOSS, N VON BERGEN, R BURNS, J STITES, AND D R SOLL. **A computer-assisted system for reconstructing and interpreting the dynamic three-dimensional relationships of the outer surface, nucleus and pseudopods of crawling cells.** *Cell motility and the cytoskeleton*, **41**(3):225–46, January 1998. 17, 18, 20

[53] RUEDI MEILI, BALDOMERO ALONSO-LATORRE, JUAN C DEL ALAMO, RICHARD A FIRTEL, AND JUAN C LASHERAS. **Myosin II is essential for the spatiotemporal organization of traction forces during cell motility.** *Molecular biology of the cell*, **21**(3):405–17, February 2010. 17, 21

[54] ERIN L BARNHART, GREG M ALLEN, FRANK JÜLICHER, AND JULIE A THERIOT. **Bipedal locomotion in crawling cells.** *Biophysical journal*, **98**(6):933–42, March 2010. 17

[55] DAVID R SOLL, DEBORAH WESSELS, PAUL J HEID, AND HUI ZHANG. **A contextual framework for characterizing motility and chemotaxis mutants in Dictyostelium discoideum.** *Journal of muscle research and cell motility*, **23**(7-8):659–72, January 2002. 18, 63

[56] M UEDA, R GRÄF, H K MACWILLIAMS, M SCHLIWA, AND U EUTENEUER. **Centrosome positioning and directionality of cell movements.** *Proceedings of the National Academy of Sciences of the United States of America*, **94**(18):9674–8, September 1997. 19

[57] W DE PRIESTER, P RIEGMAN, AND A VONK. **Effects of microtubule-disrupting agents on chemotactic events in Dictyostelium discoideum.** *European Journal of Cell Biology*, **46**:94–97, 1988. 19

[58] S YUMURA, H MORI, AND Y FUKUI. **Localization of actin and myosin for the study of ameboid movement in Dictyostelium using improved immunofluorescence.** *The Journal of cell biology*, **99**(3):894–9, September 1984. 21

[59] YOSHIAKI IWADATE AND SHIGEHIKO YUMURA. **Actin-based propulsive forces and myosin-II-based contractile forces in migrating Dictyostelium cells.** *Journal of cell science*, **121**(Pt 8):1314–24, April 2008. 21, 106

[60] T BRETSCHNEIDER, S DIEZ, K ANDERSON, J HEUSER, M CLARKE, A MULLER-TAUBENBERGER, J KOHLER, AND G GERISCH. **Dynamic actin patterns and Arp2/3 assembly at the substrate-attached surface of motile cells.** *CURRENT BIOLOGY*, **14**(1):1–10, JAN 6 2004. 21, 22

[61] KAZUHIKO S K UCHIDA AND SHIGEHIKO YUMURA. **Dynamics of novel feet of Dictyostelium cells during migration.** *Journal of cell science*, **117**(Pt 8):1443–55, March 2004. 21, 22, 23, 64

[62] CHANG-HOON CHOI, HITESH PATEL, AND DIANE L BARBER. **Expression of actin-interacting protein 1 suppresses impaired chemotaxis of Dictyostelium cells lacking the Na+-H+ exchanger NHE1.** *Molecular biology of the cell*, **21**(18):3162–70, September 2010. 21

[63] MARIA L LOMBARDI, DAVID A KNECHT, MICAH DEMBO, AND JULIET LEE. **Traction force microscopy in Dictyostelium reveals distinct roles for myosin II motor and actin-crosslinking activity in polarized cell movement.** *Journal of cell science*, **120**(Pt 9):1624–34, May 2007. 21

[64] FRANZ BRUCKERT, EMMANUEL DÉCAVÉ, DANIEL GARRIVIER, PIERRE COSSON, YVES BRÉCHET, BERTRAND FOURCADE, AND MICHEL SATRE. **Dictyostelium discoideum adhesion and motility under shear flow: experimental and theoretical approaches.** *Journal of muscle research and cell motility*, **23**(7-8):651–658, 2002. 22, 23

[65] PIERRE COSSON, BERNHARD WEHRLE-HALLER, STEVE J CHARETTE, FRANZ BRU, AND LYON I. **An adhesion molecule in free-living Dictyostelium amoebae with integrin b features.** *Molecular Biology*, **7**(6), 2006. 24, 25

[66] SOPHIE CORNILLON, ROMAIN FROQUET, AND PIERRE COSSON. **Involvement of Sib proteins in the regulation of cellular adhesion in Dictyostelium discoideum.** *Eukaryotic cell*, **7**(9):1600–5, September 2008. 24, 25, 27, 44, 64

[67] J NIEWOHNER, I WEBER, M MANIAK, A MULLERTAUBENBERGER, AND G GERISCH. **Talin-null cells of Dictyostelium are strongly defective in adhesion to particle and substrate surfaces and slightly impaired in cytokinesis.** *JOURNAL OF CELL BIOLOGY*, **138**(2):349–361, JUL 28 1997. 24, 25

[68] MASATSUNE TSUJIOKA, KUNITO YOSHIDA, AKIRA NAGASAKI, SHIGENOBU YONEMURA, ANNETTE MUELLER-TAUBENBERGER, AND TARO Q. P. UYEDA. **Overlapping functions of the two talin homologues in Dictyostelium.** *EUKARYOTIC CELL*, **7**(5):906–916, MAY 2008. 24, 25

[69] M. BERENICE DURAN, ASIF RAHMAN, MAX COLTEN, AND DERRICK BRAZILL. **Dictyostelium discoideum Paxillin Regulates Actin-Based Processes.** *PROTIST*, **160**(2):221–232, MAY 2009. 24

[70] G GERISCH, R ALBRECHT, E DE HOSTOS, E WALLRAFF, C HEIZER, M KREITMEIER, AND A MÜLLER-TAUBENBERGER. **Actin-associated proteins in motility and chemotaxis of Dictyostelium cells.** *Symposia of the Society for Experimental Biology*, **47**:297–315, January 1993. 24

[71] HITESH PATEL, IREEN KONIG, MASATSUNE TSUJIOKA, MARGARET C. FRAME, KURT I. ANDERSON, AND VALERIE G. BRUNTON. **The multi-FERM-domain-containing protein FrmA is required for turnover of paxillin-adhesion sites during cell migration of Dictyostelium.** *JOURNAL OF CELL SCIENCE*, **121**(8):1159–1164, APR 15 2008. 24

[72] LEIGH GEBBIE, MOHAMMED BENGHEZAL, SOPHIE CORNILLON, ROMAIN FROQUET, NATHALIE CHERIX, MARILYNE MALBOUYRES, YAYA LEFKIR, CHRISTOPHE GRANGEASSE, FRANZ BRU, PIERRE COSSON, DE GENE, DE MORPHOLOGIE, CH GENE, INSTITUT DE BIOLOGIE, DE CHIMIE, NATIONAL DE, RECHERCHE SCIENTIFIQUE, LYON CEDEX, AND LABORATOIRE DE BIOCHIMIE. **Phg2 , a Kinase Involved in Adhesion and Focal Site Modeling in Dictyostelium re.** *Molecular Biology of the Cell*, **15**(August):3915–3925, 2004. 24, 25

[73] J MONIAKIS, S FUNAMOTO, M FUKUZAWA, J MEISENHELDER, T ARAKI, T ABE, R MEILI, T HUNTER, J WILLIAMS, AND RA FIRTEL. **An SH2-domain-containing kinase negatively regulates the phosphatidylinositol-3 kinase pathway.** *GENES & DEVELOPMENT*, **15**(6):687–698, MAR 15 2001. 24

[74] T BUKAHROVA, G WEIJER, L BOSGRAAF, D DORMANN, PJ VAN HAASTERT, AND CJ WEIJER. **Paxillin is required for cell-substrate adhesion, cell sorting and slug migration during Dictyostelium development.** *JOURNAL OF CELL SCIENCE*, **118**(18):4295–4310, SEP 15 2005. 24, 25

[75] S CORNILLON, E PECH, M BENGHEZAL, K RAVANEL, E GAYNOR, F LETOURNEUR, F BRUCKERT, AND P COSSON. **Phg1p is a nine-transmembrane protein superfamily member involved in Dictyostelium adhesion and phagocytosis.** *J. Biol. Chem.*, **275**:34287–34292, 2000. 24, 25

[76] P FEY, S STEPHENS, MA TITUS, AND RL CHISHOLM. **SadA, a novel adhesion receptor in Dictyostelium.** *JOURNAL OF CELL BIOLOGY*, **159**(6):1109–1119, DEC 23 2002. 25

[77] ANTHONY S KOWAL AND REX L CHISHOLM. **Uncovering a role for the tail of the Dictyostelium discoideum SadA protein in cell-substrate adhesion.** *Eukaryotic cell*, **10**(5):662–71, May 2011. 25

[78] STEVE ATKINSON AND PAUL WILLIAMS. **Quorum sensing and social networking in the microbial world.** *Journal of the Royal Society, Interface / the Royal Society*, **6**(40):959–78, November 2009. 25

[79] MICHAEL KRUPPA. **Quorum sensing and Candida albicans.** *Mycoses*, **52**(1):1–10, 2009. 25

[80] ALEXANDRA KOLBINGER, TONG GAO, DEBBIE BROCK, ROBIN AMMANN, AXEL KISTERS, JOSEPH KELLERMANN, DIANE HATTON, RICHARD H GOMER, AND BIRGIT WETTERAUER. **A cysteine-rich extracellular protein containing a PA14 domain mediates quorum sensing in Dictyostelium discoideum.** *Eukaryotic cell*, **4**(6):991–8, June 2005. 25, 26

[81] JONATHAN HICKSON, S DIANE YAMADA, JONATHAN BERGER, JOHN ALVERDY, JAMES O'KEEFE, BONNIE BASSLER, AND CARRIE RINKER-SCHAEFFER. **Societal interactions in ovarian cancer metastasis: a quorum-sensing hypothesis.** *Clinical & experimental metastasis*, **26**(1):67–76, January 2009. 25

[82] RICHARD H GOMER, WONHEE JANG, AND DERRICK BRAZILL. **Cell density sensing and size determination.** *Development, growth & differentiation*, **53**(4):482–94, May 2011. 26, 27

[83] JEREMY S. DUFFIELD AND MARK L. LUPHER, JR. **PRM-151 (RECOMBINANT HUMAN SERUM AMYLOID P/PENTRAXIN 2) FOR THE TREATMENT OF FIBROSIS.** *DRUG NEWS & PERSPECTIVES*, **23**(5):305–315, JUN 2010. 26

[84] YASUO MAEDA. **Regulation of growth and differentiation in Dictyostelium.** *International review of cytology*, **244**:287–332, January 2005. 26, 68, 81, 83

[85] M. CLARKE AND R. H. GOMER. **PSF and CMF, autocrine factors that regulate gene expression during growth and early development ofDictyostelium.** *Experientia*, **51**(12):1124–1134, December 1995. 26

[86] C SCHULKES AND P SCHAAP. **CAMP-DEPENDENT PROTEIN-KINASE ACTIVITY IS ESSENTIAL FOR PREAGGREGATIVE GENE-EXPRESSION IN DICTYOSTELIUM.** *FEBS LETTERS*, **368**(2):381–384, JUL 17 1995. 26, 70

[87] PAULINE SCHAAP. **Evolution of developmental cyclic adenosine monophosphate signaling in the Dictyostelia from an amoebozoan stress response.** *Development, growth & differentiation*, **53**(4):452–62, May 2011. 26

[88] GM SOUZA, AM DA SILVA, AND A KUSPA. **Starvation promotes Dictyostelium development by relieving PufA inhibition of PKA translation through the YakA kinase pathway.** *DEVELOPMENT*, **126**(14):3263–3274, JUL 1999. 26

REFERENCES

[89] R JAIN, IS YUEN, CR TAPHOUSE, AND RH GOMER. **A DENSITY-SENSING FACTOR CONTROLS DEVELOPMENT IN DICTYOSTELIUM**. *GENES & DEVELOPMENT*, **6**(3):390–400, MAR 1992. 26, 68

[90] L TANG, R AMMANN, T GAO, AND R H GOMER. **A cell number–counting factor regulates group size in Dictyostelium by differentially modulating cAMP-induced cAMP and cGMP pulse sizes.** *The Journal of biological chemistry*, **276**(29):27663–9, July 2001. 26

[91] C. A. PARENT. **A Cell's Sense of Direction**. *Science*, **284**(5415):765–770, April 1999. 26

[92] WJ DEERY AND RH GOMER. **A putative receptor mediating cell-density sensing in Dictyostelium**. *JOURNAL OF BIOLOGICAL CHEMISTRY*, **274**(48):34476–34482, NOV 26 1999. 26

[93] M T LAUB AND W F LOOMIS. **A molecular network that produces spontaneous oscillations in excitable cells of Dictyostelium.** *Molecular biology of the cell*, **9**(12):3521–32, December 1998. 26, 70

[94] F SIEGERT AND CJ WEIJER. **SPIRAL AND CONCENTRIC WAVES ORGANIZE MULTICELLULAR DICTYOSTELIUM MOUNDS**. *CURRENT BIOLOGY*, **5**(8):937–943, AUG 1 1995. 27

[95] LEI TANG, TONG GAO, CATHERINE MCCOLLUM, WONHEE JANG, MICHAEL G VICKER, ROBIN R AMMANN, AND RICHARD H GOMER. **A cell number-counting factor regulates the cytoskeleton and cell motility in Dictyostelium.** *Proceedings of the National Academy of Sciences of the United States of America*, **99**(3):1371–6, February 2002. 27, 44, 81

[96] RICHARD B. DICKINSON AND ROBERT T. TRANQUILLO. **Optimal estimation of cell movement indices from the statistical analysis of cell tracking data.** *AIChE Journal*, **39**(12):1995–2010, December 1993. 33, 46

[97] ALKA A POTDAR, JUNHWAN JEON, ALISSA M WEAVER, VITO QUARANTA, AND PETER T CUMMINGS. **Human mammary epithelial cells exhibit a bimodal correlated random walk pattern.** *PloS one*, **5**(3):e9636, January 2010. 34, 49

[98] XIAO-MEI ZHAO, YOUNAN XIA, AND GEORGE M WHITESIDES. **Soft lithographic methods for nano-fabrication**. *Journal of Materials Chemistry*, **7**(7):1069–1074, 1997. 36

[99] K STEPHAN, P PITTET, L RENAUD, P KLEIMANN, P MORIN, N OUAINI, AND R FERRIGNO. **Fast prototyping using a dry film photoresist: microfabrication of soft-lithography masters for microfluidic structures**. *Journal of Micromechanics and Microengineering*, **17**(10):N69–N74, 2007. 36

[100] G. UHLENBECK AND L. ORNSTEIN. **On the Theory of the Brownian Motion**. *Physical Review*, **36**(5):823–841, September 1930. 44, 47, 125

[101] G MAHESHWARI AND D A LAUFFENBURGER. **Deconstructing (and reconstructing) cell migration.** *Microscopy research and technique*, **43**(5):358–68, December 1998. 44

[102] PETER DIETERICH, RAINER KLAGES, ROLAND PREUSS, AND ALBRECHT SCHWAB. **Anomalous dynamics of cell migration.** *Proceedings of the National Academy of Sciences of the United States of America*, **105**(2):459–63, January 2008. 44, 100

[103] HIROAKI TAKAGI, MASAYUKI J SATO, TOSHIO YANAGIDA, AND MASAHIRO UEDA. **Functional analysis of spontaneous cell movement under different physiological conditions.** *PloS one*, **3**(7):e2648, January 2008. 44, 64, 71, 81, 100

[104] LIANG LI, SIMON F NØ RRELYKKE, AND EDWARD C COX. **Persistent cell motion in the absence of external signals: a search strategy for eukaryotic cells.** *PloS one*, **3**(5):e2093, January 2008. 44, 49, 64, 65, 100

[105] YUSUKE T MAEDA, JUNYA INOSE, MIKI Y MATSUO, SUGURU IWAYA, AND MASAKI SANO. **Ordered patterns of cell shape and orientational correlation during spontaneous cell migration.** *PloS one*, **3**(11):e3734, January 2008. 44, 64, 81, 100

[106] M J POTEL AND S A MACKAY. **Preaggregative cell motion in Dictyostelium.** *Journal of cell science*, **36**:281–309, April 1979. 45, 64

[107] H QIAN, M P SHEETZ, AND E L ELSON. **Single particle tracking. Analysis of diffusion and flow in two-dimensional systems.** *Biophysical journal*, **60**(4):910–21, October 1991. 45

[108] J SCOTT GRUVER, ALKA A POTDAR, JUNHWAN JEON, JIQING SAI, BRIDGET ANDERSON, DONNA WEBB, ANN RICHMOND, VITO QUARANTA, PETER T CUMMINGS, AND CHANG Y CHUNG. **Bimodal analysis reveals a general scaling law governing nondirected and chemotactic cell motility.** *Biophysical journal*, **99**(2):367–76, July 2010. 49

[109] THOMAS GREGOR, KOICHI FUJIMOTO, NORITAKA MASAKI, AND SATOSHI SAWAI. **The onset of collective behavior in social amoebae.** *Science (New York, N.Y.)*, **328**(5981):1021–5, May 2010. 53, 68, 70, 82

[110] SÉBASTIEN FACHE, JÉRÉMIE DALOUS, MADS ENGELUND, CHRISTIAN HANSEN, FRANÇOIS CHAMARAUX, BERTRAND FOURCADE, MICHEL SATRE, PETER DEVREOTES, AND FRANZ BRUCKERT. **Calcium mobilization stimulates Dictyostelium discoideum shear-flow-induced cell motility.** *Journal of cell science*, **118**(Pt 15):3445–57, August 2005. 56

[111] COLIN MCCANN, MEGHAN DRISCOLL, PAUL KRIEBEL, CAROLE PARENT, AND WOLFGANG LOSERT. **Cell speeds, persistence, and information transmission during signal relay and collective migration in Dictyostelium discoideum**. *Bulletin of the American Physical Society*, **Volume 55,**, March 2010. 63, 64, 82, 104

[112] P A DIMILLA, K BARBEE, AND D A LAUFFENBURGER. **Mathematical model for the effects of adhesion and mechanics on cell migration speed.** *Biophysical journal*, **60**(1):15–37, July 1991. 64

[113] M H GAIL AND C W BOONE. **The locomotion of mouse fibroblasts in tissue culture.** *Biophysical journal*, **10**(10):980–93, October 1970. 64

[114] LIANG LI, EDWARD C COX, AND HENRIK FLYVBJERG. **'Dicty dynamics': Dictyostelium motility as persistent random motion.** *Physical biology*, **8**(4):046006, May 2011. 64, 65

[115] LEONARD BOSGRAAF AND PETER J M VAN HAASTERT. **The ordered extension of pseudopodia by amoeboid cells in the absence of external cues.** *PloS one*, **4**(4):e5253, January 2009. 64

[116] PETER J M VAN HAASTERT AND LEONARD BOSGRAAF. **Food searching strategy of amoeboid cells by starvation induced run length extension.** *PloS one*, **4**(8):e6814, January 2009. 64, 71, 101

[117] G M VISWANATHAN, E P RAPOSO, F BARTUMEUS, JORDI CATALAN, AND M G E DA LUZ. **Necessary criterion for distinguishing true superdiffusion from correlated random walk processes.** *Physical review. E, Statistical, nonlinear, and soft matter physics*, **72**(1 Pt 1):011111, July 2005. 65, 100

[118] A RATHI AND M CLARKE. **Expression of early developmental genes in Dictyostelium discoideum is initiated during exponential growth by an autocrine-dependent mechanism.** *Mechanisms of development*, **36**(3):173–82, February 1992. 68

[119] N IIJIMA, T TAKAGI, AND Y MAEDA. **A proteinous factor mediating intercellular communication during the transition of Dictyostelium cells from growth to differentiation.** *Zoological science*, **12**(1):61–9, February 1995. 68

[120] Z Xiao, N Zhang, D B Murphy, and P N Devreotes. **Dynamic distribution of chemoattractant receptors in living cells during chemotaxis and persistent stimulation.** *The Journal of cell biology*, **139**(2):365–74, October 1997. 69

[121] C Janetopoulos, T Jin, and P Devreotes. **Receptor-mediated activation of heterotrimeric G-proteins in living cells.** *Science (New York, N.Y.)*, **291**(5512):2408–11, March 2001. 69

[122] Pauline Schaap. **Evolution of developmental cyclic adenosine monophosphate signaling in the Dictyostelia from an amoebozoan stress response.** *Development, growth & differentiation*, **53**(4):452–62, May 2011. 69

[123] M N Simon, D Driscoll, R Mutzel, D Part, J Williams, and M Véron. **Overproduction of the regulatory subunit of the cAMP-dependent protein kinase blocks the differentiation of Dictyostelium discoideum.** *The EMBO journal*, **8**(7):2039–43, July 1989. 69

[124] B Varnum, K B Edwards, and D R Soll. **The developmental regulation of single-cell motility in Dictyostelium discoideum.** *Developmental biology*, **113**(1):218–27, January 1986. 71, 74, 75, 80, 82

[125] Hazel P Williams and Adrian J Harwood. **Cell polarity and Dictyostelium development.** *Current opinion in microbiology*, **6**(6):621–7, December 2003. 72

[126] S Huang and Donald E Ingber. **The structural and mechanical complexity of cell-growth control.** *Nature Cell Biology*, **1**(5):E131–8, 1999. 86

[127] Miguel Vicente-Manzanares, Colin Kiwon Choi, and Alan Rick Horwitz. **Integrins in cell migration - the actin connection.** *Journal of Cell Science*, **122**(9):1473, 2009. 86

[128] Peter Friedl. **Prespecification and plasticity: shifting mechanisms of cell migration.** *Current Opinion in Cell Biology*, **16**(1):14–23, 2004. 86

[129] Benjamin Geiger, Joachim P Spatz, and Alexander D Bershadsky. **Environmental sensing through focal adhesions.** *Nature Reviews Molecular Cell Biology*, **10**(1):21–33, 2009. 86

[130] S Fukuda, T Yasu, D N Predescu, and G W Schmid-Schönbein. **Mechanisms for regulation of fluid shear stress response in circulating leukocytes.** *Circulation Research*, **86**(1):E13–E18, 2000. 86

[131] M B Lawrence, C W Smith, S G Eskin, and L V McIntire. **Effect of venous shear stress on CD18-mediated neutrophil adhesion to cultured endothelium.** *Blood*, **75**(1):227–237, 1990. 86

[132] Nitzan Resnick, Hava Yahav, Ayelet Shay-Salit, Moran Shushy, Shay Schubert, Limor Chen Michal Zilberman, and Efrat Wofovitz. **Fluid shear stress and the vascular endothelium: for better and for worse.** *Progress in Biophysics and Molecular Biology*, **81**(3):177–99, 2003. 86

[133] Peter F Davies, Jos A Spaan, and Robert Krams. **Shear stress biology of the endothelium.** *Annals of Biomedical Engineering*, **33**(12):1714–1718, 2005. 86

[134] Nolia Gomes, Chantal Legrand, and Franoise Fauvel-Lafve. **Shear stress induced release of von Willebrand factor and thrombospondin-1 in HUVEC extracellular matrix enhances breast tumour cell adhesion.** *Clinical experimental metastasis*, **22**(3):215–223, 2005. 86

[135] P A DiMilla, J A Stone, J A Quinn, S M Albelda, and D A Lauffenburger. **Maximal migration of human smooth muscle cells on fibronectin and type IV collagen occurs at an intermediate attachment strength.** *The Journal of Cell Biology*, **122**(3):729–737, 1993. 86

[136] C Zhu. **Kinetics and mechanics of cell adhesion.** *Journal of biomechanics*, **33**(1):23–33, 2000. 86

[137] Edmond W K Young and Craig A Simmons. **Macro- and microscale fluid flow systems for endothelial cell biology.** *Lab on a Chip*, **10**(2):143–160, 2010. 86, 87, 89, 90, 117

[138] Olivier Thoumine and Albrecht Ott. **Influence of adhesion and cytoskeletal integrity on fibroblast traction.** *Cytoskeleton*, **35**(3):269–280, 1996. 86

[139] Lily Y Koo, Darrell J Irvine, Anne M Mayes, Douglas A Lauffenburger, and Linda G Griffith. **Co-regulation of cell adhesion by nanoscale RGD organization and mechanical stimulus.** *Journal of Cell Science*, **115**(Pt 7):1423–1433, 2002. 86

[140] Emmanuel Décavé, Daniel Garrivier, Yves Bréchet, Bertrand Fourcade, and Franz Bruckert. **Shear flow-induced detachment kinetics of Dictyostelium discoideum cells from solid substrate.** *Biophysical Journal*, **82**(5):2383–2395, 2002. 86, 88, 91, 92, 93, 95, 97, 100, 104

[141] A J García, P Ducheyne, and D Boettiger. **Quantification of cell adhesion using a spinning disc device and application to surface-reactive materials.** *Biomaterials*, **18**(16):1091–1098, 1997. 86

[142] R Kapur and A S Rudolph. **Cellular and cytoskeleton morphology and strength of adhesion of cells on self-assembled monolayers of organosilanes.** *Experimental cell research*, **244**(1):275–85, 1998. 86

[143] Cdric Boura, Sylvaine Muller, Dominique Vautier, Dominique Dumas, Pierre Schaaf, Jean Claude Voegel, Jean Franois Stoltz, and Patrick Menu. **Endothelial cell–interactions with polyelectrolyte multilayer films.** *Biomaterials*, **26**(22):4568–75, 2005. 86

[144] Edmond W K Young, Aaron R Wheeler, and Craig A Simmons. **Matrix-dependent adhesion of vascular and valvular endothelial cells in microfluidic channels.** *Lab on a Chip*, **7**(12):1759–1766, 2007. 86, 88

[145] Hang Lu, Lily Y Koo, Wechung M Wang, Douglas A Lauffenburger, Linda G Griffith, and Klavs F Jensen. **Microfluidic shear devices for quantitative analysis of cell adhesion.** *Analytical Chemistry*, **76**(18):5257–5264, 2004. 86, 89, 126

[146] Edgar Gutierrez and Alex Groisman. **Quantitative measurements of the strength of adhesion of human neutrophils to a substratum in a microfluidic device.** *Analytical Chemistry*, **79**(6):2249–2258, 2007. 86, 87, 89, 90, 117

[147] Keon Woo Kwon, Sung Sik Choi, Sang Ho Lee, Byungkyu Kim, Se Na Lee, Min Cheol Park, Pilnam Kim, Se Yon Hwang, and Kahp Y Suh. **Label-free, microfluidic separation and enrichment of human breast cancer cells by adhesion difference.** *Lab on a Chip*, **7**(11):1461–1468, 2007. 86

[148] Luthur Siu Lun Cheung, Xiangjun Zheng, Ashley Stopa, James C Baygents, Roberto Guzman, Joyce A Schroeder, Ronald L Heimark, and Yitshak Zohar. **Detachment of captured cancer cells under flow acceleration in a bio-functionalized microchannel.** *Lab on a Chip*, **9**(12):1721–1731, 2009. 86, 91, 93

[149] D Garrivier, E Décavé, Y Bréchet, F Bruckert, and B Fourcade. **Peeling model for cell detachment.** *The European physical journal E Soft matter*, **8**(1):79–97, 2002. 86, 96

[150] C Cozens-Roberts, D A Lauffenburger, and J A Quinn. **Receptor-mediated cell attachment and detachment kinetics. I. Probabilistic model and analysis.** *Biophysical Journal*, **58**(4):841–856, 1990. 86

REFERENCES

[151] M D WARD, M DEMBO, AND D A HAMMER. **Kinetics of cell detachment: peeling of discrete receptor clusters.** *Biophysical Journal*, **67**(6):2522–2534, 1994. 86

[152] EVAN A EVANS AND DAVID A CALDERWOOD. **Forces and bond dynamics in cell adhesion.** *Science*, **316**(5828):1148–1153, 2007. 86

[153] S USAMI, H H CHEN, Y ZHAO, S CHIEN, AND R SKALAK. **Design and construction of a linear shear stress flow chamber.** *Annals of biomedical engineering*, **21**(1):77–83, January 1993. 87, 88

[154] AMEYA S. KANTAK, BRUCE K. GALE, YURI LVOV, AND STEVEN A. JONES. **Platelet Function Analyzer: Shear Activation of Platelets in Microchannels.** *Biomedical Microdevices*, **5**(3):207–215, September 2003. 88

[155] PETER RUPPRECHT, LAURENT GOLÉ, JEAN-PAUL RIEU, CYRILLE VÉZY, ROSARIA FERRIGNO, HICHEM C. MERTANI, CHARLOTTE RIVIÈRE, AND YOSHINORI HAYAKAWA. **A tapered channel microfluidic device for comprehensive cell adhesion analysis, using measurements of detachment kinetics and shear stress-dependent motion.** *(submitted for publication in Biomicrofluidics)*, 2011. 89, 97

[156] GEORGE KEITH BATCHELOR. *An Introduction to Fluid Dynamics*. Cambridge University Press, 2002. 90

[157] A L KOCH. **The logarithm in biology. 1. Mechanisms generating the log-normal distribution exactly.** *Journal of Theoretical Biology*, **12**(2):276–290, 1966. 93

[158] THOMAS GERVAIS, JAMIL EL-ALI, AXEL GÜNTHER, AND KLAVS F JENSEN. **Flow-induced deformation of shallow microfluidic channels.** *Lab on a Chip*, **6**(4):500–507, 2006. 93, 117, 119

[159] MATHIAS BUENEMANN, HERBERT LEVINE, WOUTER-JAN RAPPEL, AND LEONARD M SANDER. **The role of cell contraction and adhesion in dictyostelium motility.** *Biophysical journal*, **99**(1):50–8, July 2010. 106

[160] JORDAN JACOBELLI, F CHRIS BENNETT, PRIYA PANDURANGI, AARON J TOOLEY, AND MATTHEW F KRUMMEL. **Myosin-IIA and ICAM-1 regulate the interchange between two distinct modes of T cell migration.** *Journal of immunology (Baltimore, Md. : 1950)*, **182**(4):2041–50, February 2009. 106

[161] TIM LÄMMERMANN, BERNHARD L BADER, SUSAN J MONKLEY, TIM WORBS, ROLAND WEDLICH-SÖLDNER, KARIN HIRSCH, MARKUS KELLER, REINHOLD FÖRSTER, DAVID R CRITCHLEY, REINHARD FÄSSLER, AND MICHAEL SIXT. **Rapid leukocyte migration by integrin-independent flowing and squeezing.** *Nature*, **453**(7191):51–5, May 2008. 106

[162] DEAN BOTTINO, ALEXANDER MOGILNER, TOM ROBERTS, MURRAY STEWART, AND GEORGE OSTER. **How nematode sperm crawl.** *Journal of cell science*, **115**(Pt 2):367–84, January 2002. 106

[163] HENRIK BRUUS. *Theoretical Microfluidics (Oxford Master Series in Physics)*. Oxford University Press, USA, 2007. 118

[164] **NIST WebBook Chemie**, 2011. 120

[165] M SPIGA AND G L MORINI. **A symmetric solution for velocity profile in laminar flow through rectangular ducts**. *International Communications in Heat and Mass Transfer*, **21**(4):469–475, 1994. 121

Appendix

A. Migration Error Analysis

Noise on positions: Origin and effect on MSD and velocity autocorrelation function

In our experiments, there are two sources of error when recording cell centroid positions: (*i*) camera error σ_C and (*ii*) repositioning error of the stage σ_R. Camera error is due to the cumulated effect of finite pixel size and changes in illumination and contrast affecting the thresholding procedure. It can be reduced by using a larger lens magnification and a larger pixel array of the camera. Experimentally, one may evaluate this error by recording non moving dusts or fixed cells while not using the motorized stage: $\sigma_C \simeq 0.5$ and 0.1μm with a 4x or 20x objective lens respectively. This noise is uncorrelated with itself in time and can be treated as an independent white noise. The repositioning error of the stage depends on the stage speed and travel range and is independent of the magnification. It could be correlated with itself in time: the stage used in the experiments sometimes drifts slowly in a given direction. For the experiments presented here we measured a drift of about 0.5μm/min.

In principle it is possible to subtract this drift to the individual cell positions. At short times, each error source affects MSD and velocity autocorrelation function ($C(t)$ or $Z(t)$) but this effect remains minor and cannot explain the overshoot observed in the MSD nor the negative peak of $Z(t)$ near 2 minutes. This is demonstrated by Fig. 5. In (**A**), the MSD/t curves for dusts and cells at two different magnification (4x and 20x) are represented. At 2 min, the amplitude of noise is clearly smaller than the overshoot amplitude as measured by the difference between MSD/t and the best fit using the Fürth's formula (Eq.(3.1) in the main manuscript). Correcting cell positions with the stage drift has a minor effect on the MSD of cells as well (diamonds in Fig. 5A). The Velocity autocorrelation function of dusts shows a negative peak but with a slightly smaller amplitude than the negative peak of cells and it is shifted to lower times (*i.e.*,30 sec) (Fig. 5B). Cells are therefore truly presenting a tendency to move in opposite directions at two minutes intervals. In conclusion, one can consider that the noise on tracked positions due to camera and stage repositioning errors estimated from the mean-squared displacement of fixed dusts is $\sigma_T \leq 1.5\mu$m with the 4x objective lens and our fast moving motorized stage.
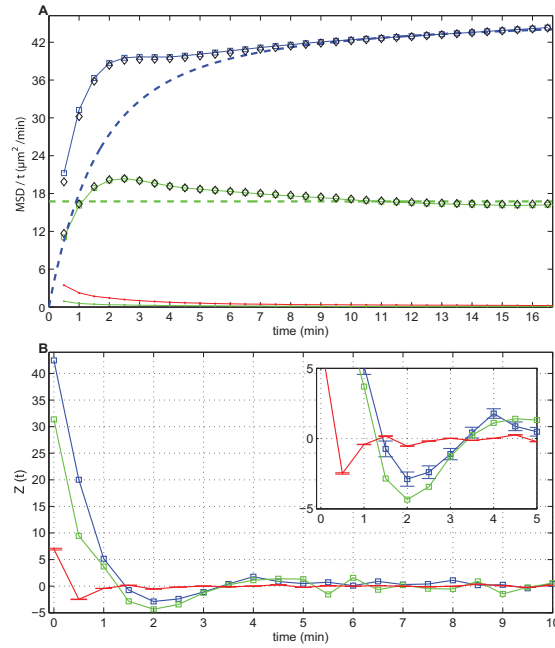
Figure 5: Noise on positions. (**A**) *MSD/t Vs. t* at 4x (blue squares) and 20x (green squares) magnification calculated for cells in the vegetative state (data of chapter 3). *MSD/t* of fixed dusts are represented by red and green dots for 4x and 20x respectively. Black diamonds represent *MSD/t* calculated from cells trajectories corrected with the drift of dust coordinates. Dotted lines are fits using the Fürth's formula (Eq. 3.1) of *MSD/t*. The fit is calculated from data points in the range 500-1000 sec but is represented in the full range 0-1000 sec to appreciate the overshoot height. (**B**) Velocity autocorrelation *Vs.* time for cells at 4x (blue squares) and 20x (green squares) magnification, and dust at 4x magnification (red line). The inset gives a larger view of the negative peaks. Concerning dusts, the negative peak due to camera and repositioning errors occurs around 30 seconds (the time interval used to record dusts movement). Cells speed autocorrelation shows a negative peak around 2 min which cannot be explained by position errors.

B.   Adhesion error analysis

Two main possible error sources affect the measured number of detached cells and the estimated wall shear stress.

1. Statistical and counting errors

2. Physical incertitudes and device approximations

Statistical and counting errors.

A limited number of cells creates a statistical error when data are described by a lognormal cumulative distribution function (cdf).

$$e(\sigma) = \frac{1}{2}\left[1 + \text{Erf}\left(\frac{\ln\left(\sigma/\sigma_{1/2}\right)}{\sqrt{2}\widetilde{\sigma}}\right)\right]. \tag{1}$$

To estimate the error of the fit parameters ($\sigma_{1/2}$ and $\widetilde{\sigma}$) in eq. 1 due to the limited experimental sample, *i.e.* the finite cell number, we used a numerical resampling method. Our resampling method for error estimation is the following: **(a)** Fit the data points to obtain $\sigma_{1/2}$ and $\widetilde{\sigma}$ of the distribution **(b)** Take for each stress position (cf. Fig.1 in the main paper, red rectangles) the number of cells at the start. **(c)** Create a random sample of this size according to the lognormal distribution with the parameters of step (a). **(d)** Fit the lognormal cdf to these sampled points. **(e)** Repeat (c) and (d) some 1000 times in order to get a distribution of sampled fit parameters. The variance of this sampled fit parameters leads to the error for $\sigma_{1/2}$ and $\widetilde{\sigma}$.

At good conditions (well-chosen stress range, high cell density), we got statistical fit errors ($2 \cdot$ standard dev) of 2% of the value for $\sigma_{1/2}$ and 7% of the value for $\widetilde{\sigma}$ for *Dictyostelium* . For MDA-MB-231 with lower densities, errors were at 5% of the value for $\sigma_{1/2}$ and 13% of the value for $\widetilde{\sigma}$.

As second statistical error, image treatment has to be considered. Cells are able to migrate under shear stress. Therefore, cell trajectories can be tangent among themselves, so that two or more cells are hardly perceptible as two single cells. However, by optimizing the parameters of the *Find Maxima* routine of ImageJ (cf. materials&methods), we reduced this error to less than 1% of the total cell number even for high cell densities up to $5 \cdot 10^4$cells/cm^2; furthermore, it is not a systematic error, a fluctuating one and is averaged out by fitting over data points. Thus,

compared with other uncertainties, this has little effect. Same applies for the error due to image edges: cells on the edges might leave the field of vision without having been detached. Yet the typical number of cells on the edges is rather low (about $5 - 20$ compared to a total cell number of $500 - 1500$ per image), and the fluctuations (*i.e.* migrating into/out of field of vision) of this number are even lower. A detachment fit which uses typically $150 - 300$ images/datapoints downsizes this fluctuations even more.

Physical incertitudes and device approximations.

We now list all possible errors and approximations that contribute to the wall shear stress error (δ_σ): absolute estimate of channel height or relative height changes due to PDMS deformation, temperature-dependency of viscosity, and non-constant channel width and thus non-constant shear stress for a given field of view.

Lack of stress homogeneity is considered to be a drawback for tapered channels(137). For 2.2x1.7 mm fields of view, the width-depending stress varies within this field with a standard deviation of the stress smaller than 5% of the stress value for 19 of 24 zones, guaranteeing stress-homogenity. Taking the same field of vision for the device of (146), the same condition would only be the case for 3 of 8 zones, what brings out the advantages of a larger design. For simple cell detachment experiments, however, absolute stress homogenity over one field of vision is not vital. Since threshold stresses are smoothly distributed (we use lognormal distributions), this distribution can be approximated as linear for the stress range of one field of vision. Hence, averaging out the variations is reasonable. It has to be kept in mind that channel positions with rather constant stress should be used for strongly varying distribution parts and vice versa. We checked that a reduction of the field of view from 2.2x1.7 mm to 2.2x0.85 mm (*i.e.*, a twice smaller window size along channel direction x) yielded indeed no differing results for detachment experiments.

As second possible error source, flow in microfluidic channels induces internal pressures that can alternate considerably channel dimensions. Because of the coupling of channel deformation and fluid flow, an analytical analysis is rather difficult. (158) introduces a dimensionless deformation number N_d related to maximal channel deformation $\Delta h_{max}/h$:

$$\frac{\Delta h_{max}}{h} = c_1 N_d = c_1 \frac{\Delta p w}{E h} \tag{2}$$

where Δp is the pressure difference between inside and outside, w and h are the channel width and height respectively, E is the Young's modulus of PDMS, and c_1 is a number of order of magnitude 1. To estimate N_d, one needs to estimate the hydrodynamic pressure difference between the point of interest and the outside pressure p_0: $\Delta p = QR_H$. The hydrodynamic resistance R_H consists of three parts: the resistance of the tapered channel R_{H_1}, the resistance of the transition piece R_{H_2} (see Fig. 6), and the resistance of the outlet tube R_{H_3}.

The resistance for a tapered channel is calculated in eq. 8 below, whereas the resistances for rectangular and circular tubes, R_{H_2} and R_{H_3}, can be found in standard hydrodynamic textbooks(163). This leads to a pressure drop $\Delta p(x)$:

$$\Delta p(x) = Q \cdot \left(\frac{8\eta L_c}{\pi r^4} + \frac{12\eta L_t}{h^3 w_t} + \frac{12\eta L(x)}{h^3} \frac{\ln\left(\frac{w_{out}}{w(x)}\right)}{w_{out} - w(x)} \right) \qquad (3)$$

where L_c is the length of the circular outlet tube, $2r$ its inner diameter; L_t is the length of the transition piece, w_t its width. $L(x)$ is the length of the part of the tapered channel which lies between the considered point and the outlet (and which therefore contributes to the local pressure), w_{out} is the width of the tapered channel next to the outlet (this can be 200 or 5000 μm, depending on the way we orient the channel).
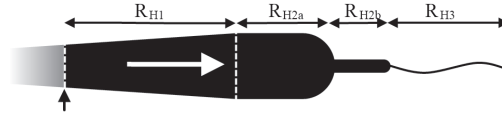
Figure 6: Contributions to the inner pressure by the hydrodynamic resistances at a given point x in the channel (vertical arrow). The white arrow indicates flow direction. Only channel parts/tubes downstream from the position x are relevant. The transition piece (R_{H_2}) consists of two parts, which are approximated as rectangular channel pieces both.

The deformation number N_d as estimation for $\Delta h_{max}/h$ calculated from the pressure drop calculation, together with experimentally measured $\Delta h_{max}/h$ are shown in Fig. 7. By taking $E = 1$ MPa for reticulated PDMS, the condition $N_d \ll 1$ is fulfilled for our experiments with *Dictyostelium* cells, but not or experimental conditions with MDA-MB-231 (Fig. 7, black dotted line, $Q = 17$ mL/h, $h = 50$ μm). The calculation predicts a non-negligible swelling of up to 15% of the channel height. We confirmed and quantified this swelling by confocal microscopy (Leica SP5) using a fluorescein solution flow. Experimental data $\Delta h_{max}/h$ are presented as upward looking black triangles in Fig. 7. We therefore corrected channel height h and the velocity
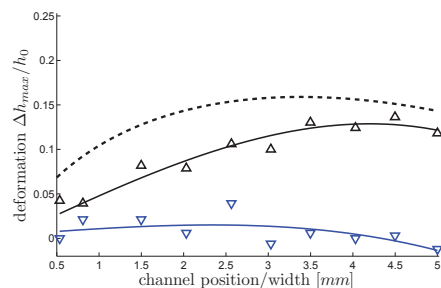
Figure 7: Channel deformation $\Delta h_{max}/h$, measured by confocal microscopy. Black upwards looking triangles for experimental conditions used for MDA-MB-231, blue downwards looking triangles for conditions used for *Dictyostelium*. The cubic fits (solid lines) are used for calibrating our experiments. The dashed line gives the deformation number N_d for MDA-MB-231 conditions and shows that N_d can be used as an upper estimate for deformation.

field in the spirit of (158) by fitting with an third order polynomial curve (black curve in Fig. 7) the measured heights. Note that the dotted line which represents N_d is no exact theoretical model for $\Delta h_{max}/h$ (since $\Delta h_{max}/h = c_1 N_d$, and c_1 depends on w in non-trivial manner(158)), but an order of magnitude estimation.

However, in principle, alternate PDMS type and curing conditions allow to attain $E \approx$ 4 MPa (158). Furthermore, the transition piece of our design is comfortable as it helps for bubble issues, but it is not vital. Its removal together with the higher Young's modulus leads to much smaller deformation numbers N_d, yielding errors for the channel height of less than 2%. In addition we interchanged in- and outlet position compared to Fig.1 to decrease the hydrodynamic pressure for the more sensitive channel part with larger widths. This can be reasonable means to control deformation if confocal microscopy is not available.

We also quantified the swelling for experimental conditions for *Dictyostelium* ($Q = 5$ mL/h, $h = 100\mu$m), blue downwards looking triangles in Fig. 7. The swelling $\Delta h_{max}/h$ is everywhere less than 2%. Since the channel height at the side-walls is significantly less modified than in the middle of the channel, the channel deformation can be estimated as $\langle \Delta h \rangle /h \approx 2/3 \Delta h_{max}/h$ (cf. the paper of (158)) and can be neglected with reasonable error ($[0.5 - 1.5]\mu$m).

Confocal microscopy offers a comfortable way to measure relative height variations, but can hardly give an absolute height value (due to refractive index mismatch). For that we used a surface profiler with a precision of about 1 μm. In combination with the deformation error for h, we can estimate the absolute channel height error $\delta_h \approx 2\ \mu$m, independently of position x along channel direction.

The shear stress can be influenced by several other parameters: flow rate, temperature, channel width. Channel width incertitude has less effect than height, since it appears only linearly in the stress expression and lateral dimensions are easily measurable by any microscopy. Our syringe pump delivers a very precise flow rate control. Temperature-dependent error is given by the temperature dependency of the viscosity of water. Temperature-dependent viscosity values are from the *NIST Chemistry WebBook*(164). For error calculus, we interpolated linearly between data points. We do the error propagation into the stress by propagation of uncertainty using the derivative of the stress with regard to the respective size and combine the independent errors as root of the squares.

Using typical uncertainties for our device ($\delta_h \approx 2\mu$m, $\delta_T \approx 1°$C), we get $\delta_{\sigma_h} \approx 4\%$ and $\delta_{\sigma_T} \approx 2.4\%$ of the stress value. The error of σ depending on the channel height h is clearly dominant.

To propagate the error δ_σ into the fit parameters, we use again a resampling method as described above for the statistical error. Concretely, we take samples with σ distributed as Gaussian[1] with standard deviation δ_σ as root of the squares of δ_{σ_h} and δ_{σ_T}.

The resulting errors are typically 5% of the value for $\sigma_{1/2}$ and 10% of the value for $\widetilde{\sigma}$.

Combining the primary error sources as root of the squares, we are able to give a total error estimation. For best conditions for *D. Discoideum*, the main error is due to physical uncertainties. It is about 6% of the value for $\sigma_{1/2}$ and 13% of the value for $\widetilde{\sigma}$. For MDA-MB-231, due to low cell densities, the statistical error prevails, but the order of magnitude of the total relative error remains the same.

---

[1]A Gaussian distribution of errors is not evident, but in our case surely a good enough approximation.

C. Shear stress calculus solving the 3D Navier-Stokes equation for a rectangular channel

The classic wall shear stress for rectangular channels with $w \gg h$ is given as

$$\sigma(w(x)) = \eta \frac{dv}{dz}_{z=0} = \frac{6\eta Q}{h^2 w(x)}. \tag{4}$$

If the condition $w \gg h$ is not fulfilled (for our design, $w_{min} = 200\mu$m, $h = 100\mu$m for *Dictyostelium* experiments), the Navier-Stokes (NS) equation has to be solved in 3D. This had already been done in the middle of the 20th century, and we will hold on to a paper by (165) which brings out the symmetry with respect to w and h in his solution.

The starting point is the x-component of the NS equations; inertial terms have been neglected, the pressure gradient can be supposed to be locally linear:

$$\nabla^2 v_x(y,z) = -\frac{\Delta p}{\eta L} \tag{5}$$

With a fourier series analysis for $v_x(y,z)$, we get the components of the fourier series development, and further using the boundary conditions $v(z = 0 \text{ or } z = h) = 0$ and $v(y = 0 \text{ or } y = w) = 0$, we get

$$u_x(x,y,z) = \frac{16}{\pi^4} \frac{\Delta p}{\eta L} \sum_{n,m \text{ odd}} k_{nm} \sin\left(n\pi \frac{y}{w(x)}\right) \sin\left(n\pi \frac{z}{h}\right), \tag{6}$$

with the factor

$$k_{nm} = \frac{1}{nm\left(\frac{n^2}{w(x)^2} + \frac{m^2}{h^2}\right)}$$

which we use here to cut short the formula within the article.

The shear stress is then given as $\sigma_{x\zeta} = \eta \frac{\partial v_x}{\partial \zeta}$. As the cells adhere at the bottom of the channel ($z = 0$), the derivative with respect to $\zeta = z$ is the only one to be considered, since $\sigma_{xy}(z = 0)$ is zero because of the term $\sin\left(n\pi \frac{z}{h}\right)$. The expression for the shear stress therefore is

$$\sigma_{xz}(x,y,z = 0) = \frac{16}{\pi^4} \frac{\Delta p}{L} \sum_{n,m \text{ odd}} k_{nm} \sin\left(n\pi \frac{y}{w(x)}\right) \frac{n\pi}{h}. \tag{7}$$

Hydrodynamic resistance of a tapered channel

The hydrodynamic resistance R_H is useful to know for 1) calculating the internal pressure in microchannels (see deformation analysis above) 2) calculating the flow rates via $Q = \Delta p/R_H$, when a given pressure drop is applied (*e.g.* flow creation by gravity), and not a given flow rate (what we did with syringe pumps).

For tapered channels, $\Delta p/L$ is not constant. For slow variations of $w(x) = w_0 + (w_1 - w_0) \cdot x/L$, a piecewise rectangular geometry can be approximated for tapered channels. $Q = wh^3\Delta p/(12\eta L)$ for rectangular channels transforms to $Q = w(x)h^3/(12\eta)\frac{dp}{dx}$. dp/dx can be integrated, and the relation $\Delta p = QR_H$ allows then to identify the hydrodynamic resistance

$$R_H = \frac{12\eta L}{h^3} \frac{ln\left(\frac{w_1}{w_0}\right)}{w_1 - w_0} \tag{8}$$

# D.   Soft lithography and production of a microsystem

To make microfluidic systems, we use mainly PDMS[1], a polymer of the family of siloxanes whose preparation in the laboratory is quick and easy. It is a viscoelastic solid, that is to say, it behaves like a viscous liquid at high temperatures while it has the same properties as elastic solid at low temperatures.

To fabricate microfluidic systems in PDMS (Fig. 8), one must first make a mold called master. To do this, we use a photosensitive dry resin. We first carefully wash the glass slide on which we want to do the master, and we deposit two layers of dry resin Etertec HQ-100 [21] of 50 microns thick each. Next, we overlay a mask previously created on a computer and printed with extreme accuracy representing the microsystem to be reproduced (see Fig. 2.7). We expose it under a UV lamp, then heat it thirty seconds on a hotplate at 75°C so that only the resin exposed to light crosslinks. After that, we develop with calcium carbonate ($CaCO_3$ 9 g/L), which removes the resin not exposed to UV without altering the master created. Finally, we treat the master by silanization: We place it in a vacuum bell with 25 μL of silane for three hours. The latter is absorbed by the surface of the master to facilitate the detachment of PDMS which comes later. Once the master is in our possession, it can be used to mold the PDMS. We prepare a solution containing silicone elastomer and 10% crosslinker agent, which is degassed with a vacuum pump and then is deposited on the previously created master. Although the crosslinking takes place naturally within 48 hours, you can speed it up by putting the system in the oven at 75°C for 1 hour. The microsystem is then removed from the mold. At the inputs (represented by circles), the PDMS is drilled from side to side to facilitate the future connection of the tubes to the microchannels. We then glue the microsystem on a glass slide by O_2 plasma.

---

[1] polydimethylsiloxane
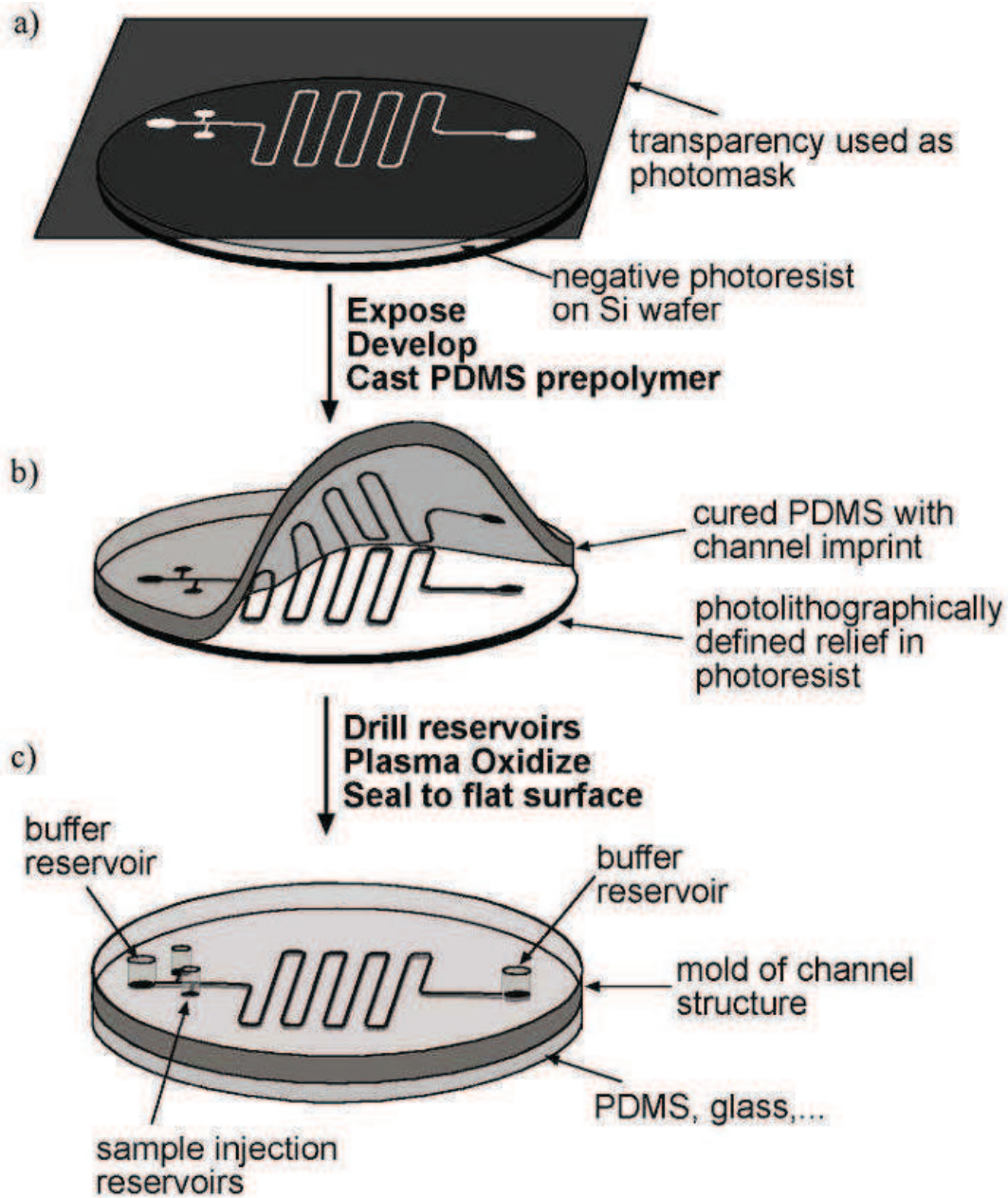
Figure 8: Schematic of the steps in the fabrication of a microsystem.

E.   Mean squared Displacement Equation

In order to understand the role of inertia in Brownian motion, Ornstein solved the Langevin equation (100):

$$m\ddot{x} = -\gamma_0 \dot{x}(t) + F_{thermal}(t) \tag{9}$$

where, m is the inertial mass of the Brownian particle. The force from the surrounding medium is the sum of two terms: Stokes friction $\gamma_0 \dot{x}$, and a random thermal force $(F_{thermal}(t) = 2k_B T \gamma_0)^{1/2} \eta(t)$ with Gaussian white-noise statistical properties,

$$\langle \eta(t) \rangle = \langle \eta(t)_j(t') \eta(t)_k(t'') \rangle = \delta_{j,k} \delta(t' - t'') \tag{10}$$

Equation 9 can be rewritten as

$$P \frac{\partial v}{\partial t} = -v + (2D)^{\frac{1}{2}} \eta \tag{11}$$

where D is the diffusion coefficient. $P \cong m/\gamma_0$, and is referred as the persistent time, which characterizes the time of the velocity auto-correlation function and may be understood as the time for which a given velocity is remembered by the system.

$$Z(t) = \langle v(0) \cdot v(t) \rangle = \frac{D}{P} \exp^{-\frac{|t|}{P}} \tag{12}$$

A new relationship between mean-square displacement and time was found by solving Equation 11:

$$MSD = \langle \rho^2(t) \rangle = 2nD(t - P(1 - \exp^{-\frac{t}{P}})) \tag{13}$$

where $n = 2$ in the case of 2D migration. Equation 11 is about the simplest possible kind in mathematical modeling. The persistent random motion it describes is termed the Ornstein-Uhlenbeck process (OU-process), and has served as the standard reference for cell motility since its discovery.

F.   Adhesion in the course of Developments: preliminary results

We studied cell adhesion in the course of development using device described by (145). Briefly, each channel is composed of two different rectangle of opposite width and length. By adjusting the length of Large channel and small channel we keep a constant hydrodynamic resistance and therefore get different shear stress for each part. in this case the shear stress applied is defined as:

$$\sigma = \frac{6Q\eta}{wh^2} \tag{14}$$

It was the first device we developed, and besides the advantages that shear stress was strictly constant in each part of the device, the interconnection between branches and low range of stress possibly applied with a single flow rate as well as cell density heterogeneity in each channels force us to develop a new and more versatile device. Despite all these drawbacks, we could perform a comparative study of cell migration in DB either after 1 hour of starvation either after 6 hours was performed. The idea was to have a first idea of adhesion/migration interplay by comparing results obtained in chapter 4 concerning migration with adhesion. We measure the number of detached cells every 30 seconds after flow was applied, and quantified cell adhesion using $\sigma_{1/2}$ after 70 min (Fig. 9). We found that cell adhesion significantly decreases with starvation time with a $\sigma_{1/2} = 0.54 \pm 0.04$ Pa and 0.33 ± 0.03 Pa after 1 hour and 8 hours of starvation, respectively.
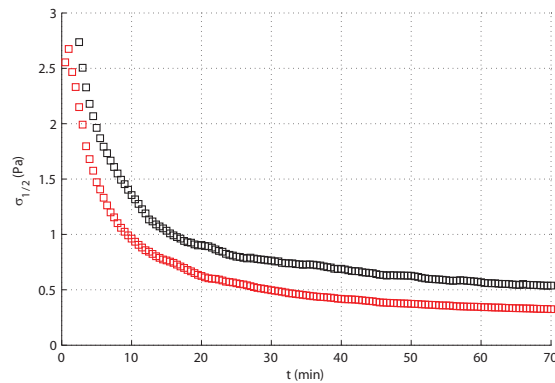
Figure 9: Adhesion in the course of development. mean shear stress necessary to detach 50% of cells as a function of time of applied flow. Cells after 8 hours of starvation (black squares) adhere less than cells after 1 hour of starvation (red squares).